THE UNIVERSITY OF OKLAHOMA

GRADUATE COLLEGE

BAROTROPIC INSTABILITY IN RELATION TO THE GENERATION OF SYNOPTIC-SCALE ATMOSPHERIC VORTICES

A DISSERTATION

SUBMITTED TO THE GRADUATE FACULTY

in partial fulfillment of the requirements for the

DOCTOR OF PHILOSOPHY

BY

CHUNG YI TSENG

Norman, Oklahoma

1975

BAROTROPIC INSTABILITY IN RELATION TO

THE GENERATION OF SYNOPTIC-SCALE ATMOSPHERIC VORTICES

APPROVED BY

Yoshi Sasaki

Rex L. Inman

Maurice Rasmussen

Claude E. Duchon

Martin C. Jischke

DISSERTATION COMMITTEE

ABSTRACT

It is generally known that barotropic instability cannot account for the development and intensification of a cyclone by means of conversions between available potential energy and kinetic energy. That is a baroclinic process. However, after the cyclone has initially developed due to baroclinic instability, the barotropic process may explain the subsequent development of synoptic-scale disturbances. This study will explore the relation between barotropic instability and the generation of synoptic-scale disturbances during the extreme tornadic outbreak of April 3-4, 1974.

The general features of barotropic instability are reviewed and the effect of smoothing of a wind profile on the stability characteristics is examined. It is found that smoothing eliminates the unstable waves due to truncation errors or errors inherent in the finite difference approximation, leaving, as a result, large-scale instability characteristics which have physical significance. The effect of extending the boundaries to infinity on the stability characteristics of a velocity profile is also studied. It is found that such an extension (which is more physically meaningful for the data studied) will increase the instability of the velocity profile.

The stability characteristics (unstable waves, growth rates, most preferred wavelength, momentum transport, etc.) of each wind profile at four mandatory levels during the April 3-4, 1974 tornado outbreak are computed and discussed. It is found that the atmosphere over

the area of maximum tornadic activity was barotropically most unstable on 0000Z April 4, i.e., shortly before the tornado outbreak. This result indicates the possibility that barotropic instability may be synoptically associated with the tornado outbreak.

ACKNOWLEDGMENTS

This study was supported by the National Science Foundation under Contract GA 30976, and also for several months by the National Aeronautics and Space Administration under Contract NAS 9-13360, and was conducted under the direction of Dr. Yoshi Kazu Sasaki, to whom I wish to express my hearty thanks for his guidance, assistance and encouragement. Support was also received from the Graduate College Research Development Fund, University of Oklahoma. The doctoral program was supported by the National Science Council, Taiwan, Republic of China.

I wish to express my gratitude to the other Doctoral Committee members: Dr. Rex L. Inman, Dr. Claude E. Duchon, Dr. Martin C. Jischke, Dr. E. F. Blick, and Dr. Maurice L. Rasmussen for their encouragement and assistance through all the phases of my doctoral program. I am particularly indebted to Dr. Jay S. Fein for his valuable discussions and suggestions on the manuscript of this research. A very special thanks is extended to Ms. Anita Cameron for typing the manuscript.

TABLE OF CONTENTS

LIST OF TABLES

LIST OF FIGURES

Figure		Page

Figure		Page

Figure		Page

Figure		Page

Figure | Page

LIST OF SYMBOLS

b	characteristic length, half the width of a channel
c	phase speed
c_r, c_i	real and imaginary part of phase speed c
d	gridlength
e	$=2.71828182 \ldots$
E	total kinetic energy
$\overline{E}, E'$	kinetic energy of mean flow and disturbances
f	Coriolis parameter
g	acceleration of gravity
i	$= \sqrt{-1}$
j	index
L	wavelength
$L_{\varkappa}, L_o$	lower and upper critical wavelength of an unstable wave
m, n	an integer
N	number of subdivisions
r	a measure of wavelength in y direction of U(y)
R	Reynolds number
S	smoothing element
S_1	first smoothing element
S_2	second smoothing element
t	time coordinate
u	x-component of velocity
$\overline{u}, u'$	x-component of velocity of mean flow and disturbances

U	$\equiv \overline{u}$
U'	$\equiv \frac{dU}{dy}$
U''	$\equiv \frac{d^2U}{dy^2}$
$\overline{U}$	smoothed value of U
U_e	a dimensional mean flow of an easterly current
U_{max}, U_{min}	maximum and minimum of $U(y)$
$U_\varkappa$	U at critical point $y_\varkappa$
v	y-component of velocity
v'	y-component of velocity of disturbances
x,y	space coordinates
$y_\varkappa$	y at critical points where $\beta - U'' = 0$
z	pressure height
Z	$\equiv \beta - U''$
$\overline{Z}$	smoothed value of Z
α	wavenumber
β	$= \frac{df}{dy}$ Rossby parameter
ζ	$= \frac{\partial v}{\partial x} - \frac{\partial u}{\partial y}$ relative vorticity
$\overline{\zeta}$	$= -\frac{dU}{dy}$ relative vorticity of mean flow
ζ'	relative vorticity of disturbances
θ	angle of tilt of troughs and ridges measured from positive y-direction
π	$= 3.141592653 \ldots$
τ	Reynolds' stress
φ	amplitude of stream functions
φ^*	complex conjugate of φ
φ_r,φ_i	real and imaginary part of φ

φ_r, φ_i	derivative of φ_r and φ_i with respect to y
$(\varphi_y)_{in}$	derivative of φ with respect to y in phase with φ
$(\varphi_y)_{out}$	derivative of φ with respect to y out of phase with φ
Φ	geopotential height
$\overline{\Phi}, \Phi'$	geopotential height of mean flow and disturbances
ψ'	disturbance stream functions
$\overline{(\ )}$	mean in x-direction or smoothed quantities
$(\ )^*$	dimensionless quantities or complex conjugate

BAROTROPIC INSTABILITY IN RELATION TO THE GENERATION OF SYNOPTIC-SCALE ATMOSPHERIC VORTICES

CHAPTER I

INTRODUCTION

The study of hydrodynamic instability of parallel flow U(y) has been a classical problem in hydrodynamics, but its application to geophysical problems is relatively modern. Rayleigh (1880, 1913) has shown that parallel flow of an inviscid nonrotating fluid is stable if the velocity profile U(y) has no inflection point, and for instability to occur, the absolute value of the vorticity of the basic current must have a maximum in the field of flow. Tollmien (1935) has shown that, for symmetric velocity profiles in a channel, and for the boundary-layer velocity profiles, the condition $\frac{d^2U}{dy^2} = 0$ at some point in the basic current is a sufficient condition for instability. The earlier works on hydrodynamic instability of parallel flow have been surveyed by Lin (1955) and Yih (1969). Recent developments have been treated by Drazin and Howard (1966). The viscous theory of parallel-flow instability has been summarized by Reid (1965).

Kuo (1949) and Foote and Lin (1950) extended the nonrotating instability theory of Rayleigh for geophysical applications to a rotating earth by the addition of the β term. They showed that the absolute vorticity must be a maximum or minimum at some point(s) in the basic current. It was also found that the β-effect, in general, reduces the instability of westerly jets and increases the instability of easterly jets (see also Kuo, 1973). Kuo (1951) considered the energetics of barotropic instability and showed that when amplified waves exist, kinetic energy is fed from the basic current into the disturbances, while the effect of damped disturbances is to feed the energy into the basic current. Lipps (1962) considered the barotropic instability of a nondivergent Bickley jet. Lipps (1963) examined the instability of a Bickley jet in a divergent, barotropic fluid and applied the theory to the Gulf Stream. Howard and Drazin (1964) investigated the stability characteristics of various basic velocity profiles. Lipps (1965) discussed the stability properties of hyperbolic-tangent shear flow. Jacobs and Wiin-Nielsen (1966) extended the instability theory of homogeneous fluids to a stratified atmosphere. Lorenz (1972) considered the barotropic instability of the Rossby wave motion and suggested that barotropic instability is largely responsible for the unpredictability of the real atmosphere.

In the tropics, where the baroclinicity is weak, barotropic instability has naturally drawn the attention of many authors who have attempted to correlate it to tropical phenomena. Indeed many studies have recently been published on barotropic instability in the tropics as an energy source of easterly flow. Nitta and Yanai (1969) studied the instability of an easterly current with a symmetric sine-curve profile. Lipps (1970) examined the stability characteristics of a hyperbolic tangent wind profile in the tropics. Yamasaki and Wada (1972a) extended Nitta and Yanai's research and showed that the stability properties of the easterly current are different from those of the westerly current in several respects. Yamasaki and Wade (1972b) investigated the vertical structure of the barotropic unstable waves in tropical easterlies. Despite many investigations of various authors, barotropic instability associated with the horizontal shear of the easterlies has not yet been fully explored.

Since the barotropic instability equation is a nonlinear one, the mathematical treatment is very difficult except for limited cases of special velocity profiles, such as sine-curve velocity profiles, the Bickley jet and the hyperbolic tangent shear layer. One must resort to numerical methods to determine the stability characteristics of basic currents with various profiles. Various authors (Wiin-Nielsen, 1961; Haltiner and Song, 1962) have investigated the instability problem by finite difference methods or finite Fourier series. Yanai and Nitta (1968) investigated the accuracy of the finite difference approximation in solving the stability problem of a nondivergent barotropic current. It was shown that for a sufficiently accurate description of the instability, a large number of subdivisions, at least 20, are required for a symmetric sine-curve basic current. Applications of the finite difference method proposed by them are found in Nitta and Yanai (1969) and Yamasaki and Wada (1972a,b). Dickinson and Clare (1973) used the shooting method and a fourth-order matrix approximation to solve the instability problem of a hyperbolic tangent barotropic shear flow. The barotropic stability equation can be formulated as a variational problem. This allows us to use the finite-element method to solve the instability problem numerically (see Appendix E for a description of this method).

In middle latitudes, barotropic instability has been investigated in conjunction with variations of the westerly jet. It is generally accepted that barotropic instability is not as important as baroclinic instability in middle latitudes where baroclinicity dominates. Barotropic models rarely predict occurrences of strong intensification of weather systems, and do not account for the formation of extratropical cyclones. However, after large-scale disturbances develop due to baroclinic instability, further development may be produced by barotropic instability. The purpose of the present work is to attempt to relate barotropic instability to the generation of synoptic-scale atmospheric vortices. The data for the present analysis are taken from the synoptic data of the tornado outbreak during April 3-4, 1974. This tornado outbreak was the greatest in recorded history in terms of number of tornadoes, track lengths, area affected and damage. One hundred and fifteen tornadoes occurred within the area generally encompassed by a line from Chicago southward to the Gulf of Mexico and eastward to the Atlantic coast. The hardest hit area consisted of Indiana, Ohio, Kentucky, Tennesse and Alabama. The barotropic instability analysis of the wind profiles over this area is performed for sixteen wind profiles, i.e., wind profiles for four mandatory levels: 850 MB, 700 MB, 500 MB and 300 MB and for four time steps: 0000Z April 3, 1200Z April 3, 0000Z April 4 and 1200Z April 4. The domain considered is chosen so that the atmospheric flow is quasi-parallel and the disturbances are small, as shown in Figures 46, 47, 48 and 49. The atmosphere over the central and east-central United States is very baroclinic during this period of intensification and, following the thermal wind constraint, the quasi-parallel jet stream is predominantly due to this baroclinicity. Shortly after 0000Z April 4 a tornado outbreak took place in this quasi-parallel flow area. It is easily conjectured that the tornado outbreak might be associated with the parallel-flow instability, although other instabilities of more complicated processes may also be possible. It would be interesting and rewarding to examine a simple physical mechanism such as barotropic instability in the synoptic environment which supported a severe tornado outbreak.

CHAPTER II

BASIC EQUATIONS

In this study the atmospheric motion is assumed to be horizontal, nondivergent and barotropic. The equations of motion, continuity equation, vorticity equation and energy equation take the form (e.g. see Haltiner, 1971)

$$\frac{\partial u}{\partial t} + u \frac{\partial u}{\partial x} + v \frac{\partial u}{\partial y} - fv = - \frac{\partial \Phi}{\partial x} \tag{1}$$

$$\frac{\partial v}{\partial t} + u \frac{\partial v}{\partial x} + v \frac{\partial v}{\partial y} + fu = - \frac{\partial \Phi}{\partial y} \tag{2}$$

$$\frac{\partial u}{\partial x} + \frac{\partial v}{\partial y} = 0 \tag{3}$$

$$\frac{\partial \zeta}{\partial t} + u \frac{\partial \zeta}{\partial x} + v \frac{\partial \zeta}{\partial y} + v \beta = 0 \tag{4}$$

$$\frac{\partial E}{\partial t} = \frac{\partial}{\partial t} \tfrac{1}{2} \iint (u^2 + v^2) \, dxdy = 0 \tag{5}$$

where u and v are the x- and y-component of velocity, f is the Coriolis parameter, $\Phi = gz$ the geopotential, g the acceleration of gravity, z the pressure height, ζ the relative vorticity, $\beta \equiv \frac{df}{dy}$ the Rossby parameter and E the kinetic energy. Eq. (4) expresses the conservation of absolute vorticity and Eq. (5) the conservation of kinetic energy. Since the effect of the variation of the density ρ is assumed to be small, ρ will be taken as constant and will not enter into the equations defining physical quantities.

We define

$$
\begin{aligned}
u &= \bar{u}\ (y,\ t) + u'\ (x,\ y,\ t) \\
v &= v'\ (x,\ y,\ t) \\
\zeta &= \bar{\zeta}\ (y,\ t) + \zeta'\ (x,\ y,\ t),\ \bar{\zeta} = -\frac{\partial \bar{u}}{\partial y} \\
\Phi &= \bar{\Phi}\ (y,\ t) + \Phi'\ (x,\ y,\ t)
\end{aligned}
\tag{6}
$$

Here the barred quantities denote average values in x-direction, which are zeroth order functions. The primed quantities denote the departures from the average values, which can also be taken as representing first order perturbations. The $\bar{u}$ (y, t) is assumed to be parallel to the x-axis and $\bar{v}$ is assumed to be zero. From Eq. (6) it is obvious that the average values of the departures are zero, i.e. $\overline{u'} = \overline{v'} = \overline{\zeta'} = \overline{\Phi'} = 0$. On substituting

$$\frac{\partial \bar{u}}{\partial t} + \overline{u' \frac{\partial u'}{\partial x}} + \overline{v' \frac{\partial u'}{\partial y}} = 0 \tag{7}$$

$$\overline{u' \frac{\partial v'}{\partial x}} + \overline{v' \frac{\partial v'}{\partial y}} + f\bar{u} = -\frac{\partial \bar{\Phi}}{\partial y} \tag{8}$$

$$\frac{\partial \bar{\zeta}}{\partial t} + \overline{u' \frac{\partial \zeta'}{\partial x}} + \overline{v' \frac{\partial \zeta'}{\partial y}} = 0\ . \tag{9}$$

The continuity equation is automatically satisfied.

If we define the mean-flow kinetic energy $\bar{E}$ as

$$\bar{E} = \tfrac{1}{2} \int \bar{u}^2\, dy$$

and the perturbation kinetic energy E' as

$$E' = \tfrac{1}{2} \int \overline{(u')^2 + (v')^2}\, dy$$

Then from Eq. (5) we obtain

$$\frac{\partial \bar{E}}{\partial t} = -\frac{\partial E'}{\partial t} \equiv -\frac{\partial}{\partial t} \tfrac{1}{2} \int \overline{(u')^2} + \overline{(v')^2}\, dy \tag{10}$$

Note that the dimension of $\bar{E}$ and E' is different from the dimension of E.

Substituting (6) into (1), (2), (3) and (4) and using the relations (7), (8) and (9) we get, to lowest order, the following equations for the perturbations:

$$\frac{\partial u'}{\partial t} + \bar{u}\frac{\partial u'}{\partial x} + v'\frac{\partial \bar{u}}{\partial y} - f v' = -\frac{\partial \Phi'}{\partial x} \tag{11}$$

$$\frac{\partial v'}{\partial t} + \bar{u}\frac{\partial v'}{\partial x} + f u' = -\frac{\partial \Phi'}{\partial y} \tag{12}$$

$$\frac{\partial u'}{\partial x} + \frac{\partial v'}{\partial y} = 0 \tag{13}$$

$$\frac{\partial \zeta'}{\partial t} + \bar{u}\frac{\partial \zeta'}{\partial x} + v'\frac{d\bar{\zeta}}{dy} + v'\beta = 0 \tag{14}$$

This kind of formulation is characteristic of the regular perturbation theory. When we want to formulate the prognostic equation for the perturbations, we ignore the time rate of change of the mean flow, since the latter is of second order, as can be seen from (7), (9) and (10). After the quantities of the perturbation have been calculated, we can find the time rate of change of the mean flow. However, these second order variations are essential in determining the stability of the mean flow.

From equations (11) and (12) one finds the time rate of change of the perturbation kinetic energy

$$\frac{\partial E'}{\partial t} = \frac{1}{2}\frac{\partial}{\partial t}\int \overline{(u')^2 + (v')^2}\, dy$$

$$= -\int \overline{u'v'}\frac{\partial u}{\partial y}\, dy = \int \tau \frac{\partial \bar{u}}{\partial y}\, dy \tag{15a}$$

$$= -\int \bar{u}\frac{\partial \tau}{\partial y}\, dy \tag{15b}$$

where $\overline{u'v'}$ is the y-direction momentum transport and $\tau = -\overline{u'v'}$ is the Reynolds' stress. For the inviscid theory, the momentum transport and the Reynolds' stress should vanish at solid boundaries. From Eq. (10)

the time rate of change of the mean-flow kinetic energy becomes (e.g. see Eliassen and Kleinschmidt, 1957)

$$\frac{\partial \bar{E}}{\partial t} = - \int \tau \frac{\partial \bar{u}}{\partial y} dy \tag{16a}$$

$$= \int \bar{u} \frac{\partial \tau}{\partial y} dy \tag{16b}$$

The integrand $\bar{u} \frac{\partial \tau}{\partial y}$ in (16b) represents the rate of work done by the Reynolds' stress and therefore the rate of increase in mean-flow kinetic energy. The integrand $\tau \frac{\partial \bar{u}}{\partial y}$ in (15a) correspondingly represents the rate at which the Reynolds' stress increases the kinetic energy of perturbations.

If the perturbations are assumed to be cyclic in x, from (7) and (9) we obtain the time rate of change of the momentum of the relative vorticity of the mean flow in the form (e.g. see Eliassen and Kleinschmidt, 1957)

$$\frac{\partial \bar{u}}{\partial t} = \frac{\partial \tau}{\partial y} = - \frac{\partial}{\partial y} \overline{u'v'} \tag{17}$$

$$\frac{\partial \bar{\zeta}}{\partial t} = - \frac{\partial}{\partial y} \overline{v'\zeta'} \tag{18}$$

where the term $\overline{v'\zeta'}$ is vorticity transport.

Normal Mode Solution of Perturbation Equations

The continuity equation for perturbation flow (13) allows us to define a stream function for the perturbation flow

$$u' = - \frac{\partial \psi'}{\partial y} \qquad v' = \frac{\partial \psi'}{\partial x} \tag{19}$$

and it follows that

$$\zeta' = \frac{\partial^2\psi'}{\partial x^2} + \frac{\partial^2\psi'}{\partial y^2} .$$

If we now set

$$\psi' = \varphi\ (y)\ e^{i\alpha(x-ct)} , \qquad (20)$$

i.e., proceed with the normal mode solution, the vorticity equation for a two-dimensional disturbance (14) becomes (Kuo, 1949)

$$(U - c)\ (\varphi'' - \alpha^2\varphi) + (\beta - U'')\ \varphi = 0$$

Here we use a prime to denote a differentiation with respect to y and use $U \equiv \bar{u}\ (y)$ for convenience in the following discussion. α is the real wavenumber in x-direction, c the complex phase velocity. We now define the dimensionless variables as follows

$$y^* = \frac{y}{b} , \quad U^* = \frac{U-U_{min}}{U_{max}-U_{min}} , \quad \varphi^* = \frac{\varphi}{b(U_{max}-U_{min})} ,$$

$$\alpha^* = \alpha b , \qquad \beta^* = \frac{\beta b^2}{U_{max}-U_{min}} ,$$

$$c^* = c_r^* + i c_i^* = \frac{c - U_{min}}{U_{max}-U_{min}} ,$$

$$c_r^* = \frac{c_r-U_{min}}{U_{max}-U_{min}} , \qquad c_i^* = \frac{c_i}{U_{max}-U_{min}}$$

where b is a characteristic length for a specified problem (here defined as half the width of the channel or the shear zone). U_{max} and U_{min} are the maximum and minimum value of the basic current U(y) in the field of flow. The nondimensional parameter β^* measures the ratio of planetary vorticity to the scale of the shear vorticity.

The nondimensionalized equation without the asterisks assumes the form

$$(U-c)\ (\varphi'' - \alpha^2\varphi) + (\beta - U'')\ \varphi = 0 \qquad (21)$$

Note than when $\beta = 0$ Eq. (21) becomes the Rayleigh stability equation, i.e., inviscid form of the Orr-Sommerfeld equation,

$$(U-c)\ (\varphi'' - \alpha^2\varphi) - U''\ \varphi = \frac{1}{i\alpha R}\ (\varphi^{iv} - 2\alpha^2\varphi'' + \alpha^4\varphi) \qquad (22)$$

where R is the Reynolds number.

For an easterly basic current U_e, if we set $U = -U_e$ and use the same dimensionless variables we obtain the same Eq. (21), except the dimensionless β becomes negative (Kuo, 1973). In fact the stability characteristics of an easterly current under the influence of β are exactly the same as those of the westerly current under the influence of $-\beta$. Hence we shall use a negative β to characterize the flow properties of an easterly current. Dimensional and dimensionless atmospheric profiles are schematically shown in Figure 1. It is easily seen that with proper nondimensionalization, all the equations from (1) to (20) are also valid in dimensionless form.

Boundary Conditions

At a rigid wall, such as shown in Figure 1, the normal velocity v' of the disturbances vanishes. This can be shown to imply that

$$\varphi = 0 \qquad \text{at} \qquad y = 0,\ 2 \qquad (23)$$

if we take the position of rigid walls at dimensional $y = 0,\ 2b$. If the flow extends to infinity, then, by physical requirements φ must be bounded there. Thus boundedness of φ at infinity in general implies that φ must tend to zero there, and we may use boundary condition (23) at an infinite as well as at a finite boundary (Drazin and Howard, 1966). Other boundary conditions have been discussed by Kuo (1949) and Yanai and Nitta (1969) (for the symmetric and antisymmetric velocity profiles extending to infinity, i.e., the profiles shown in Figure 15b,d), and by Drazin and Howard (1966) (for the profiles in which U or U' is discontinuous in the field of flow).

Eq. (21) is an eigenvalue problem under appropriate boundary conditions for a given profile U of the basic current. We can find c as an eigenvalue by solving (21) with the wavenumber α specified. The phase speed c may in general be complex. When its imaginary part c_i is equal to zero, the disturbance is neutral, and when $c_i \neq 0$, the disturbance is amplified or damped. The finite difference approximation to solve (21) and find c as an eigenvalue, as proposed by Yanai and Nitta (1968), will be discussed in the Appendix.

Momentum Transport

The physical mechanism of momentum and vorticity transport associated with the stability of mean flow has been discussed by Kuo (1951). Here we briefly review the momentum and vorticity transport equations. From equations (19), (20), and (21) we obtain the y-direction momentum transport equation (Foote and Lin, 1950),

$$\overline{u'v'} = - \tau = - \frac{\alpha}{2\pi} \int_0^{2\pi/\alpha} u'v' \, dx$$

$$= - \frac{1}{4} i\alpha \left(\varphi \frac{d\varphi^*}{dy} - \varphi^* \frac{d\varphi}{dy}\right) e^{2\alpha c_i t}$$

$$= -\frac{1}{2}\,\alpha\,\left(\varphi_r \frac{d\varphi_i}{dy} - \varphi_i \frac{d\varphi_r}{dy}\right) e^{2\alpha c_i t} \qquad \text{(24a)}$$

$$= \frac{\alpha c_i}{2} \int_o^y \frac{(\beta - U'')\,|\varphi|^2}{|U-c|^2}\, dy\; e^{2\alpha c_i t}, \quad 0 < y < 2 \qquad \text{(24b)}$$

or

$$\frac{\partial \tau}{\partial y} = -\frac{\alpha c_i}{2}\,\frac{(\beta - U'')\,|\varphi|^2}{|U-c|^2}\; e^{2\alpha c_i t} \qquad \text{(24c)}$$

It should be remembered that the physical quantities u', v', ψ', ζ', etc. are understood to be the real part of their representation. The term $|\varphi|^2$ in Eq. (24b) and (24c) is proportional to $(v')^2$. The momentum transport can also be expressed in terms of the tilting of the troughs and ridges, defined as the curves along which v' is zero. Thus, the location of trough and ridge curves is determined by (Kuo, 1951)

$$\tan \alpha\,(x - c_r t) = -\frac{\varphi_i}{\varphi_r}$$

and therefore the tangent of the angle of tilt θ, measured from positive y direction, is (Kuo, 1951)

$$\tan\theta = \frac{dx}{dy} = -\frac{1}{\alpha}\,\frac{\varphi_r\,\varphi_i' - \varphi_i\,\varphi_r'}{|\varphi|^2} \qquad \text{(25a)}$$

$$= \frac{2}{\alpha^2}\,\frac{\overline{u'v'}}{|\varphi|^2}\, e^{-2\alpha c_i t} \qquad \text{(25b)}$$

From the above equation we see that the momentum transport is proportional to the tilting of the troughs and ridges.

Vorticity Transport

The vorticity transport can either be obtained in the same way, or simply by differentiating (24) with respect to y. Thus, we have the vorticity transport equation (Kuo, 1951)

$$\overline{v'\zeta'} = \frac{\alpha}{2} (\varphi_r \varphi_i'' - \varphi_i \varphi_r'') e^{2\alpha c_i t}$$

$$= - \frac{\alpha c_i}{2} \frac{(\beta - U'') |\varphi|^2}{|U-c|} e^{2\alpha c_i t} \tag{26}$$

This equation shows that the vorticity transport produced by the amplifying disturbance is in the direction of decreasing absolute vorticity of mean flow.

Time Rate of Change of Momentum of Mean Flow

Substituting Eq. (24) into (17) we get the time rate of change of momentum of mean flow

$$\frac{\partial U}{\partial t} = \frac{1}{2} \alpha (\varphi_r \varphi_i'' - \varphi_i \varphi_r'') e^{2\alpha c_i t} \tag{27a}$$

$$= - \frac{\alpha c_i}{2} \frac{(\beta - U'') |\varphi|^2}{|U-c|^2} e^{2\alpha c_i t} \tag{27b}$$

$$= \overline{v'\zeta'} \tag{27c}$$

It follows that the effect of the damped disturbance ($c_i < 0$) is to produce an increase of U in the region where β-U" is positive and a decrease where β-U" is negative, thus their effect is to sharpen the mean velocity profile. The effect of the amplifying disturbances ($c_i > 0$) is in the oppositive direction, that is to flatten the mean velocity profile.

Time Rate of Change of Kinetic Energy of Mean Flow

Substituting the expression for $\frac{\partial \tau}{\partial y}$ (24c) into the energy equation of mean flow (16b), we obtain

$$\frac{\partial \bar{E}}{\partial t} = - \frac{\alpha c_i}{2} \int_o^2 \frac{U(\beta - U'') \ |\varphi|^2}{|U-c|} \ dy \tag{28}$$

$$= - \frac{\partial E'}{\partial t}$$

Since the only energy which the disturbances can withdraw for the growth is the mean-flow kinetic energy, the expression at the right-hand side should be negative. Thus, if the perturbation kinetic energy is to increase ($c_i > 0$), then, we must also have positive β-U" associated with higher values of U and negative β-U" with lower values of U. This result is essentially due to Fjortoft (1950).

CHAPTER III

GENERAL THEOREMS OF BAROTROPIC INSTABILITY

In this chapter we briefly review some known properties of the solution of Eq. (21) subject to the boundary conditions (23). When we set y = 2 in the Eq. (24b) and since the momentum transport or Reynolds' stress vanishes at the upper boundary, we obtain the following expression

$$c_i \int_0^2 \frac{(\beta - U'')\ |\varphi|^2}{|U-c|^2}\, dy = 0 \tag{29}$$

from which follows the Kuo's theorem (1949): A necessary condition for barotropic instability ($c_i > 0$) is that at some value of y, say y_κ

$$\beta - U'' = 0 \qquad \text{at } y_\kappa,\ 0 < y_\kappa < 2 \tag{30}$$

This is an extension of the well-known theorem originally derived by Rayleigh (1880, 1913). In other words, this condition states that the absolute vorticity must be a maximum or minimum at some point in the basic current. From Eq. (29) it might be supposed at first sight that we have proved that damped disturbances ($c_i < 0$) also require β-U" to vanish at some point in the field of flow. This is not the case, however, as was pointed out by Lin (1955), and the above result applies only to amplified disturbances. It should be noted that this is only a necessary condition. The profile $U(y) = \frac{1}{2}(1-\cos \frac{\pi y}{2})$,

$0 < y < 2$, which satisfies (30) but is stable, is a classical counter-example to the sufficiency of the Rayleigh-Kuo's necessary condition. Kuo (1949) showed that for the symmetric jet which he considered, (30) is both necessary and sufficient for the existence of amplified waves. There are several theorems for the neutral solutions of (21) which are relevant to the instability problem. Based on Sturm's oscillation theorem, Kuo shows that the phase velocity of neutral waves can never exceed the maximum wind speed, but may be less than the minimum wind speed: these are Rossby-Haurwitz waves. If the neutral waves whose phase velocity c lying between the maximum and the minimum of the basic-current velocity are to exist, there must be a critical point $y = y_\varkappa$ where β-U" changes sign. If there is just one point $y_\varkappa$ (in each half of the basic current), then there is just one neutral wave and its phase velocity is $U_\varkappa$ ($U_\varkappa = U(y_\varkappa)$). For amplified waves to exist, the absolute vorticity must have a maximum or a minimum within the field of flow and, if no such points exist, all waves with a phase velocity greater than the minimum wind speed will be damped. Waves with phase speeds between U_{min} and $U_\varkappa$, i.e., $U_{min} < c_r < U_\varkappa$, are amplified and their wavelength $L > L_\varkappa$. On the other hand, the faster moving waves, $c_r > U_\varkappa$, are damped and $L < L_\varkappa$. These characteristics are illustrated in Figure 2 in dimensionless quantities. The above statement is applicable for the symmetric westerly jet that Kuo considered. There are some controversies as to whether the amplified disturbances may travel with a phase velocity c_r less than U_{min} (in dimensionless form $c_r > 1$) for an easterly jet (dimensionless $\beta < 0$) (See Chapter IX).

In 1950 Fjortoft proved the stronger necessary condition for instability that $(\beta - U'')\ (U - U_\kappa) > 0$ somewhere in the field of flow. His extension of Rayleigh's theorem can be shown to be equivalent to the statement: for instability, the absolute value of the absolute vorticity of the basic current must have a maximum in the field of flow.

Stern (1961) and Lipps (1963) extended the Rayleigh-Kuo's necessary condition (30) to a divergent flow: A necessary condition for instability for a divergent barotropic fluid is that the potential vorticity must be a maximum or minimum at some point in the basic current.

Taylor (1915) gave a physical interpretation of Rayleigh's necessary condition of instability. Lin (1955) also has interpreted physically the mechanism of parallel-flow instability by consideration of the migration of vorticity. Brown (1972) re-examined the physical interpretation of Rayleigh's condition of instability.

Modification of the proof of the semi-circle theorem (Howard, 1961) for the Eq. (21) shows that instability ($c_i > 0$) implies that

$$(c_r - \tfrac{1}{2})^2 + c_i^{\,2} \leq (\tfrac{1}{2} + \tfrac{1}{2}\frac{|\beta|}{\alpha^2})^2 . \qquad (31)$$

This implies that c lies in the upper semicircle with center $(\tfrac{1}{2}, 0)$ and radius $\tfrac{1}{2}\ (1 + \frac{|\beta|}{\alpha^2})$ in the complex c plane. It can further be shown that $c_r < 1$ when $\beta > 0$ (westerlies) and that $c_r > 0$ when $\beta < 0$ (easterlies). These modifications of Howard's semi-circle theorem are essentially due to Pedlosky (1963). This theorem is as pretty a gem as ever has been polished in the hands of hydrodynamicists, as stated by Yih (1969). However, this theorem is too general to be used to detect "spurious" unstable waves. The inequality (31) may be used to obtain an upper bound on c_i. According to (31),

$$c_i^2 \leq \frac{1}{2} + \frac{1}{2} \frac{|\beta|}{\alpha^2} \tag{32}$$

The embarrassing feature of (31) and (32) is that the semi-circle in which c must lie and the upper bound on c_i increase as $|\beta| / \alpha^2$ increases. The upper bound on the growth rate is

$$\alpha c_i \leq \frac{1}{2} \left| \frac{dU}{dy} \right|_{max} , \tag{33}$$

which was due to Hoiland (1953) and Howard (1961). This states that the growth rate can never be larger than half the absolute value of the maximum shear of the basic current. Actually the semi-circle theorem (31), upper bound on c_i (32) and the growth rate (33) have limited practical applications.

CHAPTER IV

GENERAL STABILITY CHARACTERISTICS

In this chapter we shall discuss some features of the determination of critical wavelengths and phase speeds for barotropic instability.

Lower Critical Wavelength of an Unstable Wave

According to Kuo (1949), the lower critical wavelength $L_\varkappa$ can be found by solving (21) after setting $c = U_\varkappa$, i.e., by solving the eigenvalue problem

$$\varphi'' + \frac{\beta - U''}{U - U_\varkappa}\varphi - \alpha^2\varphi = 0, \quad \alpha = \frac{2\pi}{L_\varkappa} \tag{34}$$

$$\varphi = 0 \quad \text{at} \quad y = 0, 2$$

The finite difference scheme will be discussed in the Appendix. For a velocity profile expressible in mathematical functions, the $L_\varkappa$'s can be determined quite accurately by solving (34). However, for actual atmospheric wind profiles we had better solve (21) and determine c as an eigenvalue by specifying α and locate the wavelength $L_\varkappa$ at which the phase speed of an unstable wave first becomes complex.

Upper Critical Wavelength of an Unstable Wave

For a westerly basic current, the upper critical wavelength L_o of an unstable wave can be found by solving (21) after setting

$c = 0$, i.e., by solving the eigenvalue problem (Kuo, 1949)

$$\varphi'' + \frac{\beta - U''}{U}\varphi - \alpha^2\varphi = 0, \quad \alpha = \frac{2\pi}{L_o} \tag{35}$$

$$\varphi = 0 \quad \text{at} \quad y = 0, 2$$

The finite difference scheme will be discussed in the Appendix. In general L_o can be determined quite accurately. For an easterly current ($\beta < 0$) there arise some problems in determining L_o by solving (35) when we set $c = 1$. It is possible that an unstable wave may travel with a phase speed $c_r > 1$. We may solve (35) to determine a relation between c and L for real $c > 1$ and find the minimum value of L. Thus this L is the upper critical wavelength of the unstable wave (See Chapter IX).

(c_r, c_i)-L Diagrams

If we want to know the general feature of stability characteristics, the best method is to solve (21) and find c and φ as functions of α or L. Figure 4, called a (c_r, c_i)-L diagram in this study, shows an example of the relationship between phase velocity c and the wavelength L for the symmetric sine-curve profile $U(y) = \frac{1}{2}(1 - \cos \pi y)$, $0 < y < 2$ when the dimensionless β=0.375 and the number of subdivisions N = 20. We obtain nineteen series of phase velocities c, among which a pair become complex for intermediate wavelengths as denoted by the thick line in the figure. The other seventeen series correspond to "singular" solutions having phase speeds equal to the velocities of the basic current somewhere in the field of flow. For a more detailed description of this figure, see Yanai and Nitta (1968).

Figure 5 shows the (c_r, c_i)-L diagram for the atmospheric profile at 500 MB, 0000Z April 3, 1974. The number of subdivisions is 20. The values of the dimensional and dimensionless velocity profile, dimensionless absolute vorticity gradients, and the lower and upper critical wavelengths for the unstable waves found from (34) and (35) are shown in Table 1. For this wind profile, there are four critical points and five unstable waves. The real parts of the phase speeds of these unstable waves are denoted by thick lines and the imaginary part by dotted lines. It is difficult from Figure 5 to tell the "true" unstable waves from "spurious" unstable waves due to truncation errors or errors inherent in the finite difference approximation. A closer examination of the value of β-U'' at each point in Table 1 shows that the critical points at y = 1.64 and y = 1.79 are very close to each other. These two critical points can be easily smeared out by smoothing the basic current. Hence it is possible that four of the unstable waves are actually the same unstable wave, which will be contiguous to a Rossby-Haurwitz wave. The effect of smoothing of the wind profiles on the stability characteristics will be discussed in Chapter VI. It is also found that the $L_\varkappa$'s calculated from Eq. (34), shown in Table 1 are in general different from those shown in Figure 5. The $L_\varkappa$ for one of the unstable waves is especially difficult to find accurately since the real part of the phase speed c_r for this unstable wave changes little as L increases. A little inaccuracy in interpolating $y_\varkappa$ and $U_\varkappa$ will change $L_\varkappa$ significantly. On the other hand, the unstable wave associated with the Rossby-Haurwitz wave has its $\left|\frac{dc_r}{dL}\right|$ quite large and therefore it is easier to find its $L_\varkappa$ more accurately. This type of unstable wave in general contributes to larger growth rate. It is interesting to note that for all the atmospheric wind profiles considered in this study, the eigenfunctions φ for the singular waves which become this type of unstable wave at $L_{\varkappa}$ are of first mode. The unstable waves of this type are in general the "true" unstable waves for an atmospheric wind profile and are in general of practical importance, since they contribute larger growth rate.

There are other unstable waves which change into singular waves or exist even at infinite L. Their c_r's in general change little as L increases and thus it is more difficult to determine their $L_{\varkappa}$'s accurately. They contribute in general less growth rates as compared to the unstable waves contiguous to a Rossby-Haurwitz wave. An example of the unstable wave due to truncation errors will be shown in Chapter VI, and that due to errors in the finite difference approximation will be shown in Chapter V.

Since it is not economical or feasible to increase the number of subdivisions N for the actual atmospheric wind profiles, the best method to determine whether an unstable wave is spurious is to use the technique of smoothing. For a velocity profile expressible in mathematical functions, true unstable waves can be identified by their insensitivity to variations of number of subdivisions N.

Unstable Waves

In Figure 6 and Figure 7 the eigenfunctions for some unstable waves are shown in terms of their amplitude $|\varphi|$ and phase angle arg φ. Also plotted is $\frac{d\varphi}{dy}$ expressed in terms of the component in phase and the component out of phase with φ:

$$\frac{d\varphi}{dy} = \frac{d|\varphi|}{dy} e^{i \arg \varphi} + |\varphi| \frac{d}{dy} (\arg \varphi) e^{i(\pi + \arg \varphi)}$$

$$(\varphi_y)_{in} = \frac{d|\varphi|}{dy}$$

$$(\varphi_y)_{out} = |\varphi| \frac{d}{dy} (\arg \varphi)$$

For small c_i, it can be found that the in-phase and out-of-phase component of $\frac{d\varphi}{dy}$ has a distinct singular behavior at the points where c_r is equal to the velocity of the basic current. For c_i equal to zero, i.e., for a singular wave, this singularity is more profound and will be discussed later.

The disturbance stream function of an unstable wave can be calculated from (20), i.e.,

$$\psi' = [\varphi_r' \cos \alpha(x - c_r t) - \varphi_i \sin \alpha(x - c_r t)] e^{\alpha c_i t}$$

In Figure 19a is shown the disturbance stream function of the most unstable wave for 500 MB 0000Z April 3 wind profile, which has a wavelength of 2.6 (2476 km) and amplifies by a factor of e in 3.44 days. The maximum amplitude of the disturbance occurs at y = 1.0, just at the middle of the channel. The letter C and A represent the primary centers of cyclonic and anticyclonic vorticity. The dashed lines show the trough and ridge line, where v' vanishes. The location of trough and ridge line is determined by

$$\tan \alpha (x - c_r) = - \frac{\varphi_i}{\varphi_r}$$

and the tangent of the angle of tilt θ measured from positive y direction is given by (25a) and (25b), which is proportional to the momentum transport.

The momentum transport $\overline{u'v'}$ is given by Eq. (24a,b) and is represented by a curve in Figure 8b. It goes from zero to a minimum at the first critical point, then increases from here to a maximum positive value at the second critical point. From this critical point it decreases to zero at the upper boundary except at the two critical points close to each other, where it is negative. It is seen from Figure 8b that $\overline{u'v'}\,\frac{dU}{dy}$ is mainly negative so that the time rate of change of mean-flow kinetic energy, given by (16) and (28) is negative, i.e., the perturbation is withdrawing the kinetic energy from the basic current.

The time rate of change of the basic current is given by (27) at every point of y. From Figure 8a, in which are plotted the basic current U and its time rate of change $\frac{\partial U}{\partial t}$, it is readily seen that the momentum transfer reduces the maximum shear in the mean flow and hence intensifies the disturbances.

It is found that the $\frac{\partial U}{\partial t}$ calculated by (27a) and (27b) can be used as a measure of the accuracy of the finite difference approximations. The maximum root mean square difference between these two calculations for the wind profiles considered in this study is 0.7935×10^{-3}. The maximum percentage error is less than 0.01%. Therefore, the accuracy of the finite difference approximation of Eq. (21) is satisfactory.

The vorticity transport $\overline{v'\zeta'}$, which is numerically equal to the time rate of change of the basic current $\frac{\partial U}{\partial t}$ for a plane parallel flow, is given by (26). It is found from Figure 8c that the vorticity transport is in the direction of negative y at the center part of the channel and in the direction of positive y near the boundaries.

Rossby Waves

In Figure 4 and 5 it is seen that Rossby-Haurwitz waves appear at a certain wavelength L_o. They are Rossby-Haurwitz waves of the first mode. Rossby-Haurwitz waves appear in the order of the number of modes, as can be seen from the classical frequency relation of Rossby-Haurwitz waves. Let $U(y) = U_{max} = 1$, $U_{min} = 0$, then the frequency relation reads

$$\frac{n^2\pi^2}{4} + \frac{4\pi^2}{L^2} = \frac{\beta}{1-c}.$$

Keeping the right-hand side constant, we can see that the number of modes n increases if the wavelength L increases. That is, the Rossby-Haurwitz waves of higher modes will appear first at larger wavelengths. Figure 30a shows the (c_r, c_i)-L diagram for the 700 MB 0000Z April 3 wind profile and Figure 9 shows the eigenfunction φ of the three Rossby-Haurwitz waves for this profile.

Singular Waves

In addition to the regular solutions (unstable waves and Rossby-Haurwitz waves) mentioned above, there are "singular" or "continuum" solutions, which are denoted by thin solid lines in Figures 4 and 5. These solutions correspond to continuous eigenvalues of c which are equal to the basic current U somewhere in the field of flow. It is clear from Eq. (21) that these singular solutions possess discontinuous $\frac{d\varphi}{dy}$. The eigenvalues φ at L = 1.0 for 500 MB 0000Z April 3 wind profile are shown in Figure 10 in order of numerical values of the phase speed c. The singular waves possess real phase velocity which are equal to the velocities of the basic current shown by dots. These waves have discontinuous first derivatives of φ at the points, although a small discrepancy due to the coarse finite difference is observed.

The singular solutions are best illustrated by Drazin and Howard (1966). They showed how to attack the instability problem as an initial value problem by the use of Fourier-Laplace transforms. It is found that the solution contains a discrete spectrum (regular solutions), which is the same as the normal mode solution, and a continuum spectrum (singular solutions). Case (1960) and Dikii (1960) have indicated that the integral over the continuum spectrum decays like 1/t, so the discrete spectrum alone is associated with the instability. Thus, in seeking a criterion for instability, we may use the method of normal modes and ignore the continuum spectrum. The singular or continuum solutions correspond to continuous eigenvalues of c which are equal to U somewhere in the field of flow. Case (1960) has shown that these continuum modes are needed to form a complete set of solutions for arbitrary initial disturbances. But, as noted above, we can proceed with the normal mode solution and ignore the continuum mode. It should be remarked that the singular waves shown in Figures 4 and 5 would form a continuous spectrum of phase velocities when the number of subdivisions N is increased to infinity, i.e., only the unstable waves and Rossby-Haurwitz waves are distinguishable.

Finally, let us discuss some important features of (c_r, c_i)-L diagrams. It is found that

a. c_r-curves, i.e., the curves $c_r = c_r(L)$, for singular solutions rarely cross each other, however, they may cross the c_r-curves for unstable waves.

b. The singular waves of first mode in general travel more slowly than those of higher modes.

c. For the unstable waves contiguous to Rossby-Haurwitz waves, the gradient of c_r with respect to L, i.e., $\left|\frac{dc_r}{dL}\right|$ is larger.

d. The c_r-curves for the singular solutions tend to decrease as the wavelength L increases, if they do not cross each other or the c_r-curves for the unstable waves. However, when they cross the c_r-curves for unstable waves, their slope may increase as L increases. If they cross the unstable c_r-curves at large angles, then it is possible that there is a discontinuity in the slope of the $c_i(L)$ for the corresponding unstable waves.

e. Two singular c_r-curves may converge into one unstable c_r-curve at some wavelength $L_\varkappa$. Also, at $L_\varkappa$ the gradient of c_r for singular waves with respect to L is infinite whereas that for unstable waves is finite.

f. The gradient of c_i with respect to L in the vicinity of the lower critical wavelength $L_\varkappa$ and upper critical wavelength L_o becomes infinite, as proved by Yanai and Nitta (1968).

g. Only those singular waves that are associated with unstable waves, or that cross the unstable waves, have their real part of the phase speed c_r increasing as L increases.

CHAPTER V

STABILITY CHARACTERISTICS OF SINE-CURVE PROFILES

In a later chapter, we shall compare the instability characteristics of our atmospheric wind profiles with those of sine-curve profiles, so let us now discuss some stability characteristics of westerly currents ($\beta > 0$) with symmetric and antisymmetric sine-curve profiles.

Consider a sine-curve profile given by

$$U(y) = \frac{1}{2}(1 - \cos \pi r y), \quad 0 < y < 2 \qquad (36)$$

where r is a measure of wavelength of U(y) in the y-direction and needs not be an integer. The critical points are found by

$$y_{\varkappa} = \frac{2m}{r} \pm \frac{1}{\pi r} \cos^{-1} \left(\frac{2\beta}{\pi^2 r^2}\right) \qquad 0 < y_{\varkappa} < 2$$

and the U at critical points by

$$U_{\varkappa} = \frac{1}{2}\left(1 - \frac{2\beta}{\pi^2 r^2}\right)$$

where m is an integer and should be chosen such that $0 < y_{\varkappa} < 2$. In order that the gradient of absolute vorticity may vanish somewhere in the channel, the following relation should hold

$$0 < \frac{2\beta}{\pi^2 r^2} < 1$$

Following Kuo (1949), we determine the characteristic wavenumber of the neutral solution which is relevant to the stability problem. Substituting U and $U_\varkappa$ into Eq. (34), we get

$$\varphi'' = (\alpha^2 - \pi^2 r^2) \varphi . \qquad (37)$$

(37) admits the solution

$$\varphi = \sin p y$$

where

$$p^2 = \pi^2 r^2 - \alpha^2 . \qquad (38)$$

The boundary conditions $\varphi(0) = \varphi(2) = 0$ are satisfied by

$$p = \frac{n\pi}{2} \qquad (39)$$

where n is an integer. Hence from (38) and (39) the critical wavelength is

$$L_\varkappa = \frac{4}{\sqrt{4r^2 - n^2}}$$

For a real $L_\varkappa$, n should be chosen such that $n < 2r$. The acceptable largest value of the integer n is actually the number of unstable waves for the sine-curve profile. Since our atmospheric wind profiles correspond to the sine-curve profile (36) with r less than 2, only the case $r \leq 2$ is considered in this study.

For the case $r \leq 0.5$, there is no lower critical wavelength $L_\varkappa$ and therefore no unstable waves exist. For $0.5 < r \leq 1.0$ and $n = 1$; there is one lower critical wavelength and therefore only one unstable wave. For $1 < r \leq 1.5$ and $n = 1, 2$; there are two $L_\varkappa$'s and two unstable waves. For $1.5 < r \leq 2$ and $n = 1, 2, 3$; there are three $L_\varkappa$'s and three unstable waves. For $r=0.5$, the sine-curve velocity profile is a classical counter-example to the sufficiency of the condition for instability (30). The (c_r, c_i)-L diagrams for various values of r are shown in Figure 11. It should be noted that for non-symmetric sine-curve profiles, i.e., the profiles with r not equal to an integer, the amplitude function φ of the singular solutions is not symmetric or antisymmetric except at the lower critical wavelength $L_\varkappa$ where it is symmetric or antisymmetric. In addition to these critical values of r, i.e., those r equal to 0.5, 1.0, 1.5, 2.0, etc., it is easily seen from Figure 11 that there are other critical values of r which demarcate the number of Rossby-Haurwitz waves existing for the sine-curve profiles. In Figure 12 is shown the number of unstable waves and Rossby-Haurwitz waves as a function of r and dimensionless β for the sine-curve profile (36). With these facts in mind, we can interpret the appearance of the false unstable wave, shown in Figure 11d, for the sine-curve profile (36) with $r = 1$ and the number of subdivisions $N = 6$ and $U''(y)$ expressed in differential form, i.e., $U''(y)= \frac{\pi^2 r^2}{2} \cos \pi r j d$ instead of in difference form, $U''(y)= \frac{1}{d^2} (U_{j+1} + U_{j-1} - 2U_j)$. Yanai and Nitta (1968) have not been successful in analyzing the condition for the "false" instability. Indeed as we compare Figure 11d with Figure 11e ($r = 1.0625$), we find that the main features are the same. Since the r value of the profile considered by Yanai and Nitta (1968) is on the boundary which determines whether the number of unstable wave is 1 or 2, it is possible that errors in the numerical calculation will shift the value of r exactly equal to 1 to that slightly larger than 1 or to that slightly less than 1. In the latter case there are no false waves since the number of unstable waves with $r = 1$ is the same as that with r slightly less than 1. In the former case a "false" unstable wave appears. A spurious wave also appears when $r = 2.0$ with the number of subdivisions $N = 20$ and U" expressed in differential form, as shown in Figure 11j. Hence it is possible that a spurious unstable wave will appear for the sine-curve profile (36) with r equal to 0.5, 1.0, 1.5, 2.0, etc. when numerical methods are used to calculate the stability characteristics. For other values of r, quite different from 0.5, 1.0, 1.5, 2.0, etc., no false unstable waves are reported. When U" is expressed in difference form, it happens that the numerical method will change the value of $r = 1$ or $r = 2$ to that of r slightly smaller than 1 or 2 respectively, so there are no false unstable wave existing, even when the number of subdivisions N is small.

It can be concluded that for the small value of N, the numerical calculation with U" expressed in differential form will increase the value of r slightly, and when r is equal to 0.5, 1.0, 1.5, 2.0, a spurious unstable wave will appear and the stability characteristics will be changed.

CHAPTER VI

EFFECT OF SMOOTHING OF VELOCITY PROFILES ON STABILITY CHARACTERISTICS

As stated above, smoothing techniques may play an important role in the determination of stability characteristics of actual atmospheric wind profiles. Since what interests us is the "large-scale" instability, we should smooth the basic current in order to isolate a result of physical significance and to remove the instability due to the noise. The treatment of smoothing and filtering techniques can be found in Shapiro (1970). First we consider the simple one-dimensional three point operator

$$\overline{U}_j = U_j + S\ (U_{j+1} + U_{j-1} - 2U_j) \tag{40}$$

With smoothing element $S = 0.25$, this smoother will remove two grid-length waves in the basic current. It can be easily shown that the absolute vorticity gradient $Z \equiv \beta - U''$ satisfies (40), i.e.,

$$\overline{Z}_j = Z_j + S\ (Z_{j+1} + Z_{j-1} - 2Z_j). \tag{41}$$

It can be proved that if Z_{j+1} and Z_{j-1} are of the same sign and Z_j is of opposite sign to Z_{j+1} and Z_{j-1}, then, with $S = 0.25$, if

$$|Z_j| < \frac{1}{2}\ |Z_{j+1} + Z_{j-1}|$$

the smoothed $\overline{Z}_j$ will be of the same sign as Z_{j+1} and Z_{j-1}. That is, the two critical points will be smoothed out. We may take $|Z_{j+1} + Z_{j-1}| - 2|Z_j|$ as the strength of the two critical points against the smoothing. If this strength is positive, then the two critical points will disappear after the basic current is smoothed once with the smoothing element S=0.25. If it is negative, then the two critical points will still exist after smoothing.

It is apparent that repeated applications of the simple smoother (40) would be undesirable because of excessive damping of even medium and long waves in the basic current. In fact, it would be desirable to leave waves longer than several gridlengths relatively unaffected. It is possible, by combining several smoothing elements, to design a filtering operator to suit specific requirements. Successive application of two smoothing operators of the form of Eq. (40), with smoothing elements $S_1 = 0.25$, $S_2 = -0.25$ will produce significantly less damping of the intermediate wavelengths.

It is easily seen that smoothing tends to decrease the shear of the basic current and therefore make the basic current more stable. In other words, it will decrease the upper critical wavelength L_o of an unstable wave, since the Rossby-Haurwitz wave can be more easily maintained when the shear is small. Smoothing will also decrease the imaginary part of phase speed c_i and, therefore, the growth rate. Smoothing will also increase the lower critical wavelength $L_\varkappa$ for stability.

In order to study the effect of smoothing further, let us consider the symmetric sine-curve profile $U(y) = \frac{1}{2}(1-\cos \pi r y)$, $r = 1$, $0 < y < 2$, which has been examined numerically by Yanai and Nitta (1968). Figure 13a is the (c_r, c_i)-L diagram for the above profile, except all the digits past the hundredth were truncated when the numerical values of U(y) at the grid points were computed. It is found that a spurious unstable wave appears from the wavelength $L \approx 2$ to $L \approx 13$. However, as shown in Figure 13b, after applying the operator (40), the undesirable unstable wave disappears, although there is a slight change of phase velocities and lower and upper critical wavelengths, as shown in Tables 2 and 3. It seems that smoothing is a powerful technique to eliminate the undesirable unstable waves due to the truncation errors or errors inherent in the finite difference scheme. This enables us to obtain a result of physical significance. The occurrence of the undesirable unstable wave shown in Figure 13a may be interpreted by the fact that a slight change of numerical values of U for the profile with $r = 1$ will shift its stability characteristics into those for the profile with r slightly larger than one, as stated in the last chapter. Therefore, it is possible that the effect of smoothing will reduce the actual value of r for the sine-curve profile. For the sine-curve profile (36) with $r = \frac{1}{2}$, it is found that the profile is still stable after it was smoothed once or twice ($S_1 = 0.25 = S_2$).

Let us now consider the effect of smoothing of the actual atmospheric wind profiles. Take the wind profile at 500 MB, 0000Z April 3, for instance. As mentioned above, in Chapter IV, there are five unstable waves for this wind profile, which are in such a chaotic manner that we are not able to tell the unstable waves of physical significance from other "undesirable" waves due to truncation errors or possibly due to errors inherent in the finite difference approximation. The (c_r, c_i)-L diagram for this profile has been shown in Figure 5. After the profile is smoothed one time ($S_1 = 0.25$), there remain only two unstable waves, as shown in Figure 14a, and the unstable wave which exists at infinite L before smoothing is no longer present in this figure. There is also some combination of unstable waves. This (c_r, c_i)-L diagram represents a "better" configuration since the instability due to shorter waves in the basic current has been suppressed. If we apply the smoothing twice with $S_1 = S_2 = 0.25$, there remains only one unstable wave, as shown in Figure 14b. The real part of the phase velocity c_r for this unstable wave decreases to zero very quickly as the wavelength L increases and it becomes a Rossby-Haurwitz wave at a certain wavelength L_o. Only this unstable wave is of physical significance and represents a "large-scale" instability. There is of course a slight change in the critical wavelengths and growth rates, as shown in Table 4.

In Figure 14c is shown the (c_r, c_i)-L diagram for this profile smoothed twice with smoothing elements $S_1 = -S_2 = 0.25$. In this case there are two unstable waves, since the two critical points close to each other can not be smoothed out by successive application of two smoothing operators of the form of Eq. (40) with $S_1 = -S_2 = 0.25$. However, the growth rates of unstable waves are closer to those for the nonsmoothed profile.

In conclusion, smoothing is a powerful technique to determine the large-scale instability characteristics which are of physical significance and to eliminate the undesirable waves due to truncation errors or errors inherent in the finite difference approximation. In other words, the unstable waves of physical significance can be identified by their insensitivity to smoothing.

CHAPTER VII

STABILITY CHARACTERISTICS OF VELOCITY PROFILES EXTENDING TO INFINITY

The question naturally arises as to the effect of extending the boundaries to infinity on the stability characteristics. Figure 15 shows the symmetric and anti-symmetric sine-curve velocity profiles within a channel, and those extending to infinity. The latter have the same sine-curve velocity profiles as given by

$$U(y) = \tfrac{1}{2} (1 - \cos \pi r y) \qquad r = \tfrac{1}{2}, 1$$

in the central belt $0 < y < 2$ and are constant outside this belt. This will in general tend to increase the instability, since the shear will increase slightly and the boundaries which prevented the momentum transport necessary to maintain unstable disturbances no longer exist. Take the profile with $r = \frac{1}{2}$ for instance. This profile (Figure 15c) is stable if it is in a channel with boundaries at $y = 0$ and 2, while the profile (Figure 15d)

$$U(y) = \tfrac{1}{2} (1 - \cos \tfrac{\pi y}{2}) \qquad 0 < y < 2$$

$$U(y) = 0 \qquad y < 0$$

$$U(y) = 1 \qquad y > 2$$

is unstable (e.g. see Yanai and Nitta, 1968). The profile $U(y) = \frac{1}{2}$ $(1 - \cos \pi y)$, $0 < y < 2$, shown in Figure 15a is more stable than the following profile, plotted in Figure 15b

$$U(y) = \tfrac{1}{2}\,(1 - \cos \pi y) \qquad 0 < y < 2$$

$$U(y) = 0 \qquad\qquad y \leq 0, \quad y \geq 2$$

Furthermore, the profile in Figure 15b has two unstable waves, while the profile in Figure 15a has only one unstable wave (e.g. see Yanai and Nitta, 1968). The increase in the number of unstable waves may also be interpreted by the fact that the extension of the boundaries may increase the actual r slightly.

Now let us consider our atmospheric wind profiles. A glance at the weather maps (Figure 46, 47, 48 and 49) for the levels and time considered in this study shows that the atmosphere below the lower(southeastern) boundary, i.e., over the Gulf of Mexico and Atlantic Ocean south and southeast of Florida, was quite inert. The pressure and wind fields did not change very much as compared to those over the U.S. continent. It seems that we may get a more realistic result of stability characteristics if we extend the lower boundary to infinity with the values of the velocity outside the original boundary equal to the values on this boundary. Then the wind profile will consist of a shear belt in the region $0 < y < 2$ and a constant wind belt for $y < 0$. Since we do not want wind profiles which have a discontinuity in $U'(y)$, we had better use smoothing techniques to eliminate this undesirable discontinuity. For easier manipulation of numerical calculation we place the lower boundary at $y = -1$, i.e., we add ten grid points outside the shear zone to 21 grid points within the shear zone, and use the same boundary condition, i.e., $\varphi = 0$ at $y = -1$.

Figure 16a shows the (c_r, c_i)-L diagram for the 500 MB 0000Z April 3 wind profile extending to infinity and smoothed once and

Figure 16b for that profile extending to infinity and smoothed twice. When we compare Figure 16a and 16b with Figure 14, it is found that the overall features of (c_r,c_i)-L diagram do not change very much. The unstable wave contiguous to the Rossby-Haurwitz wave is not sensitive to the extension of the lower boundary, while the unstable wave existing even at infinite L remains after moving the lower boundary from y = 0 to y = -1. This unstable wave is insensitive to smoothing in contrast to the case for the bounded wind profile. Practically speaking, this unstable wave is not important since its growth rates are small as compared to those of the unstable wave contiguous to the Rossby-Haurwitz wave. There are many (theoretically infinite) singular solutions which originate from the constant-wind belt (Yanai and Nitta, 1968). This can be easily seen from Eq. (21). As $\alpha \rightarrow \infty$, i.e., $L \rightarrow 0$

$$(U - c)\,\varphi = 0$$

or

$$c = U$$

which states that as $L \rightarrow 0$, the phase speed is equal to the basic current at the grid points. These singular c_r-curves, originating from the constant-wind belt, densely cover a portion of the (c_r,c_i)-L diagram. It is also found that no unstable waves are contiguous to the singular waves which originate from the constant-wind belt. The singular waves which originate from the constant-wind always become a Rossby-Haurwitz wave if the constant-wind speed is close to zero (Yanai and Nitta, 1968). It is also found that the growth rates for the semi-infinite wind profile is, in general, larger than those for the corresponding bounded profile, as shown in Table 4, Thus, the extension of the boundary will tend to increase the instability in the sense that it will increase the growth rates of an unstable wave inherent in a bounded profile and produce additional unstable waves.

In Figure 17 is shown a comparison of the amplitude functions φ of unstable waves for the 500 MB 0000Z April 3 wind profile (solid lines) with those for the corresponding extended profile (dotted lines). In Figure 18 is shown the $|\varphi|$ of an unstable wave at various wavelengths for the extended 500 MB 0000Z April 3 wind profile. It is found that the amplitude of unstable waves is confined in the shear belt $0 < y < 2$. The general features of the amplitude do not change much within the shear belt after the extension of the lower boundary from $y = 0$ to $y = -1$. The disturbance stream functions of the most unstable wave (at $L = 2.6$) for the 500 MB 0000Z April 3 in a channel and the corresponding extended profile are shown in Figure 19. The centers of cylonic and anticyclonic vorticity are marked by C and A. The dashed line shows the trough and ridge lines, where v' vanishes. The streamfunctions cover one wavelength in x. The streamlines are drawn at equal intervals on an arbitrary scale. There is only one cyclonic vorticity center and one anticyclonic vorticity center in one wavelength, since the amplitude $|\varphi|$ has only one maximum for this unstable wave, shown in Figure 17a. It is found that for both cases the maximum amplitude of the disturbance occurs at $y = 1$. The location of cyclonic and anticyclonic vorticity centers and the angle of tilt θ do not change much after the extension of the lower boundary to $y = -1$. However, the amplitude of the disturbances for the extended profile is larger than that for the bounded profile. This again indicates that the extension of lower boundary to infinity (actually to $y = -1$ for numerical calculations) tends to increase the degree of instability. The numerical values of momentum transport $\overline{u'v'}$, vorticity transport $\overline{v'\zeta'}$, and the time rate of change of mean momentum $\frac{\partial U}{\partial t}$ are shown in Table 5 for both cases. It is found that the direction of momentum and vorticity transport is the same in the shear belt for both cases. However, the magnitudes of the transports are intensified due to the extension of the lower boundary. In the constant-wind belt, there were positive momentum transport and negative vorticity transports, the magnitudes of which are negligibly small. The time rate of change of the mean-flow kinetic energy for the bounded profile is -7.0940, while that for the extended profile is -10.7061. From the above facts, it is concluded that the extension of the lower boundary will increase the degree of instability.

The amplitude of the additional singular waves due to the extension of the lower boundary to "infinity" is confined to the constant-wind belt, while the amplitude of the original singular waves is confined to the shear belt. Thus, it is easy to identify the additional singular waves due to the extension of the lower boundary from the original singular waves for the bounded wind profile. From Figure 20 we see that this is the case. These singular waves possess discontinuous first derivatives of φ at some points where their phase velocities are equal to the velocities of the basic current. For larger c_r this singular behavior can be seen from the figure, while for smaller c_r, only one of the discontinuities is visible in the figure. The additional singular waves have their $\frac{d\varphi}{dy}$ discontinous in the constant-wind belt and are reflected in the figure as zigzags in the φ.

It should be noted that one of the ten additional solutions φ is a Rossby-Haurwitz wave, whose phase speed is negative. The amplitude function φ of this Rossby-Haurwitz is confined in the constant-wind belt. As L increases, the amplitudes tend to spread into the shear belt. In Figure 21b are shown the φ of Rossby wave of this type for successive wavelengths. It can be seen that for $L > 5.4$ the maximum amplitude is shifted into the shear belt.

The original Rossby-Haurwitz wave, i.e., that inherent in a bounded profile, will change the number of modes from one to two. This Rossby-Haurwitz wave, which is contiguous to an unstable wave, is confined to the shear belt. As L increases it tends to spread into the constant wind zone, in contrast to the Rossby-Haurwitz wave due to the extension of the lower boundary. This can be seen from Figure 21a.

In conclusion, the extension of the lower boundary to "infinity" will increase the degree of instability for a velocity profile. However, the general patterns of the streamlines of the unstable wave and the (c_r, c_i)-L diagram do not change much for the extended wind profiles as compared to the corresponding bounded wind profiles. As already noted, we shall get a more physically meaningful result if we extend the lower boundary to infinity since the observed atmospheric flow for our study below the lower boundary was quite inert.

CHAPTER VIII

DISCUSSION ON THE STABILITY CHARACTERISTICS OF EACH WIND PROFILE

In this study the value of β for calculating the stability characteristics of actual atmospheric wind profiles is assumed constant, though our results have simple extensions for the more general function $\beta(y)$. The dimensional β is taken at latitude 36°. The domain of the atmosphere considered in this study is shown in Figure 46, 47, 48, and 49. We chose 23 x 35 grid points in this domain and on the boundaries. Only 21 x 33 values of u were obtained. Thus, we had 21 values of U(y). Most of our calculations were based on a bounded profile, i.e., we assumed the atmospheric motions occurred in a channel bounded by two rigid walls. This will in general underestimate the growth rates. For the extended profile we add ten grid points in the belt $0 < y < -1$. The gridlength is 95.2 km. Thus it is not feasible to refine the mesh and use a larger value of N. In the following we shall discuss the stability characteristics of each wind profile.

850 MB 0000Z April 3

This profile has three critical points, as denoted by black dots in Figure 22b. There are six unstable waves, as can be seen in the (c_r, c_i)-L diagram in Figure 24a. Of the four "isolated" unstable waves, three are possibly "spurious" waves due to the truncation errors or errors inherent in the finite difference approximation. They are of no practical importance since their c_i are very small. The (c_r, c_i)-L diagram for smoothed profile ($S_1 = -S_2 = 0.25$) is shown in Figure 24c, in which there remain only four unstable waves. This profile is quite unstable and no Rossby-Haurwitz wave exists. However, since the shear is small (see Figure 22a), the largest growth rate is only 0.176/day, as shown in Figure 23, corresponding to an e-folding time of 5.68 days at the most preferred wavelength L = 3.8 (3619 km). The disturbance stream function of the most unstable wave is shown in Figure 24b.

850 MB 1200Z April 3

This profile has only one critical point located at y = 0.36 with $U_\varkappa = 0.074$ and only one unstable wave from L = 1.3 to L = 6.09, where it becomes a Rossby-Haurwitz wave (Figure 25a). This profile is similar to the sine-curve profile (36) with r = 0.75 and the stability characteristics are the same as the corresponding sine-curve profile, i.e., it has only one unstable wave and one Rossby-Haurwitz wave. The largest growth rate is 0.078/day (Figure 23), corresponding to an e-folding time of 12.85 days at the most preferred wavelength L = 3.0 (2857 km). The disturbance stream function of the most unstable wave is shown in Figure 25b.

850 MB 0000Z April 4

This profile has one critical point located at y = 0.27 with $U_\varkappa = 0.13$. The critical point is close to the lower boundary and its $U_\varkappa$ is small as compared to 1. For this type of velocity profile, the c_i are, in general, very small. Only one unstable wave exists between

$L = 3.16$ to $L = 6.36$ where it becomes a Rossby-Haurwitz wave, as can be seen from the (c_r, c_i)-L diagram in Figure 26a. This profile is similar to the sine-curve profile (36) with $r = 0.75$ and the stability characteristics are similar. The growth rate is 0.066/day, corresponding to an e-folding time of 15.20 days at the most preferred wavelength $L = 4.8$ (4572 km). The disturbance stream function of the most unstable wave is shown in Figure 26b.

850 MB 1200Z April 4

This profile has two critical points at $y_\kappa = 0.17$ and $y_\kappa = 1.88$, very close to the boundaries, with corresponding $U_\kappa = 0.14$ and $U_\kappa = 0.049$ respectively. Since the critical points are close to the boundary and the U_κ's are small, we expect a small c_i for this profile. There are three unstable waves and two Rossby-Haurwitz waves for this profile (Figure 27a). The maximum growth rate is 0.029/day, corresponding to an e-folding time of 33.50 days at the most preferred wavelength L=1.6 (1524 km). The smoothed profile becomes stable with no critical point. The disturbance streamfunction of the most unstable wave is shown in Figure 27b.

700 MB 0000Z April 3

This profile has one critical point located at $y_\kappa = 1.88$ with corresponding $U_\kappa = 0.74$ (Figure 28). The critical point is close to the upper boundary and is located in a region where the shear is small. It is easily seen that the c_i of the unstable wave for this profile is very small. There are three Rossby-Haurwitz waves and one unstable wave, as shown in Figure 30a. The maximum growth rate is 0.011/day

(Figure 29), corresponding to an e-folding time of 85.38 days at the most preferred wavelength L = 1.6 (1524 km). The smoothed profile should be stable since the only critical point can easily be smoothed out. There are two cyclonic vorticity centers and two anticyclonic centers in the disturbance stream function (Figure 36b) since the $|\varphi|$ has two maxima (Figure 7).

700 MB 1200Z April 3

This profile has two critical points located at $y_\kappa = 0.19$ and $y_\kappa = 1.83$, very close to the boundaries, with corresponding $U_\kappa = 0.040$ and $U_\kappa = 0.40$ respectively. We do not expect a large growth rate for this profile. There are three unstable waves (Figure 31a). One is contiguous to a Rossby-Haurwitz wave and has a peculiar behavior, i.e., the gradient of c_r with respect to L of this unstable wave increases L at some wavelengths. This profile corresponds to the sine-curve profile (36) with r somewhere between 0.75 to 1.50. Also, its stability characteristics are similar to the sine-curve profile with r = 1.125, except for this profile one unstable wave is an "isolated" one. The maximum growth rate is 0.018/day, corresponding to an e-folding time of 32.96 days at the most preferred wavelength L = 3.6 (3429 km). The disturbance stream function is shown in Figure 31b.

700 MB 0000Z April 4

This profile has two critical points located at $y_\kappa = 0.23$ and $y_\kappa = 1.83$ with corresponding $U_\kappa = 0.19$ and $U_\kappa = 0.52$. The critical points are also close to the boundaries. There are three unstable waves

(Figure 32a), two of which should be the same one, as can be easily seen from the figure. This profile corresponds to the sine-curve profile (36) with r equal to some value between 0.75 to 1.50. Indeed, its stability characteristics are similar to the sine-curve profile with r = 1.125. The maximum growth rate is 0.125/day, corresponding to an e-folding time of 7.89 days at wavelength L = 3.0 (2857 km). The disturbance stream function is shown in Figure 32b.

700 MB 1200Z April 4

This profile has two critical points located at $y_\varkappa = 0.44$ and $y_\varkappa = 1.76$ with corresponding $U_\varkappa = 0.24$ and $U_\varkappa = 0.69$, respectively. The shear of the profile near the latter critical point is small and thus the unstable wave due to this critical point, if any, is expected to contribute little growth rate. There are three unstable waves (Figure 33a), one of which is obviously spurious. The smoothed profile has two unstable waves.(Figure 33c). One of the original unstable waves has been eliminated by smoothing. The maximum growth rate for the non-smoothed profile is 0.055/day, corresponding to an e-folding time of 18.11 days at the most preferred wavelength L = 4.8 (4572 km). The disturbance stream function of the most unstable wave is shown in Figure 33b.

500 MB 0000Z April 3

This profile has been discussed previously. The e-folding time of the most unstable wave, and the most preferred wavelength are shown in Table 8. This profile is quite similar to the sine-curve profile (36) with $r \approx 0.9$, if we exclude the two critical points too close to each other. And the "true" stability characteristics are similar to those for the sine-curve profile with $r = 0.9$, i.e., only one unstable wave and one Rossby-Haurwitz wave.

500 MB 1200Z April 3

This profile has three critical points at $y_\varkappa = 0.23$, $y_\varkappa = 0.39$ and $y_\varkappa = 1.53$, with corresponding $U_\varkappa = 0.60$, $U_\varkappa = 0.71$ and $U_\varkappa = 0.40$, respectively. The former two critical points are too close to each other and located at the region where the shear is smaller (Figure 34) as compared to the third one, and therefore they should contribute smaller growth rate. There are three unstable waves (Figure 36a), but only one is contiguous to Rossby-Haurwitz wave. It is expected that for the smoothed profile only the unstable wave associated with the Rossby-Haurwitz wave will remain. The maximum growth rate (Figure 35) for the nonsmoothed profile is 0.145/day corresponding to an e-folding time of 6.91 days at the most preferred wavelength $L = 3.8$ (3619 km). Disturbance stream function of the most unstable wave is shown in Figure 36b.

500 MB 0000Z April 4

This profile has two critical points located at $y_\varkappa = 0.34$ and $y_\varkappa = 1.59$ with corresponding $U_\varkappa = 0.72$ and $U_\varkappa = 0.38$ respectively. There are five unstable waves (Figure 37a), one of which contributes to large growth rate and has a large gradient of c_r with respect to L. For this profile there is no Rossby-Haurwitz wave. This profile corresponds to the sine-curve profile (36) with r equal to some value between 0.5 and 1.0. However, its stability characteristics are quite different from the corresponding sine-curve profile, even the smoothed profile, as shown in Figure 37c. For the smoothed profile there appears a Rossby-Haurwitz wave at a large wavelength. The maximum growth rate for the nonsmoothed profile is 0.265/days corresponding to an e-folding time of 3.77 days at the most preferred wavelength L = 5.0 (4762 km). The maximum growth rate for the smoothed profile is 0.235/days, corresponding to an e-folding time of 4.25 days at L = 5.2 (4953 km).

500 MB 1200Z April 4

This profile has two critical points at $y_\varkappa = 0.59$ and $y_\varkappa = 1.68$ with corresponding $U_\varkappa = 0.61$ and $U_\varkappa = 0.37$, respectively. The c_i of the unstable wave, if any, due to the former critical point will be smaller, since the critical point is located in the region where the shear is small. There are three unstable waves (Figure 38a). One of them should be "spurious" and can be easily eliminated by smoothing. The maximum growth rate is 0.234/days, corresponding to an e-folding time of 4.27 days at the most preferred wavelength L = 4.2 (4000 km).

300 MB 0000Z April 3

This profile has two critical points at $y_\varkappa = 0.22$ and $y_\varkappa = 1.70$ (Figure 39) with corresponding $U_\varkappa = 0.85$ and $U_\varkappa = 0.20$ respectively. The latter critical point is too close to the upper boundary and the former critical point is in the region where the shear is small. It is expected that they contribute little to the growth rates. There are four unstable waves (Figure 41a). Two of the unstable waves are actually the same unstable wave which will be contiguous to a Rossby-Haurwitz wave. Due to the boundary effect, the smoothed profile (Figure 41c) has three critical points, two of which are very close to the upper boundary and to each other. If the smoothed profile is to be smoothed once more there might be no more critical point. The maximum growth rate (Figure 40) for the nonsmoothed profile is 0.053/day, corresponding to an e-folding time of 18.97 days at the most preferred wavelength L = 4.4 (4191 km). The disturbance stream function is shown in Figure 41b.

300 MB 1200Z April 3

This profile has two critical points located at $y_{\varkappa} = 0.42$ and $y_{\varkappa} = 1.73$ with corresponding $U_{\varkappa} = 0.73$ and $U_{\varkappa} = 0.29$. There are five unstable waves (Figure 42a) . Two of the unstable waves are actually the same unstable wave which will be contiguous to a Rossby-Haurwitz wave, at wavelength L = 9.74. The maximum growth rate is 0.149/day, corresponding to an e-folding time of 6.71 days at the most preferred wavelength L = 2.0 (1905 km). The disturbance stream function is shown in Figure 42b.

300 MB 0000Z April 4

This profile has four critical points, two of which are very close to each other. From the shape of the profile and the location of the critical points, it is expected that the c_i of unstable waves for this profile is large. There are four unstable waves (Figure 43a), one of which is contiguous to a Rossby-Haurwitz wave and has a larger c_i and growth rate. For the extended profile the (c_r, c_i)-L diagrams are shown in Figures 43c and 43d. The maximum growth rate for non-smoothed profile is 0.278/day, corresponding to an e-folding time of

3.60 days at the most preferred wavelength L = 3.8 (3619 km). The corresponding disturbance stream function is shown in Figure 43b.

300 MB 1200Z April 4

This profile has two critical points located at $y_\varkappa = 0.40$ and $y_\varkappa = 1.60$ with corresponding $U_\varkappa = 0.38$ and $U_\varkappa = 0.53$ respectively. From the shape of the profile and the location of critical points, it is expected that the c_i of the unstable waves are quite large. Indeed this is the case. There are two unstable waves (Figure 44a), which should be the same unstable wave contiguous to a Rossby-Haurwitz wave. This profile is similar to the sine-curve profile with r equal to 0.9375. Their stability characteristics are also quite the same. The maximum growth rate is 0.341/day, corresponding to an e-folding time of 2.93 days at the most preferred wavelength L = 4.0 (3810 km).

CHAPTER IX

THE EFFECT OF β, SHEAR AND THE DISTANCE BETWEEN CRITICAL POINTS ON THE STABILITY CHARACTERISTICS

As has been noted in the introduction, the β-effect is, in general, to reduce the instability of westerly jets and to increase the instability of easterly jets. Well-known examples are the Bickley jet ($U(y)=\mathrm{sech}^2 y$, $-\infty < y < \infty$) and the symmetric sine-curve profile ($U(y)=\frac{1}{2}(1-\cos \pi y)$, $0 < y < 2$) (Kuo, 1973). Yamasaki and Wada (1972a) also noted that the stability characteristics of easterly currents are different from those of westerly currents.

It is generally known that longer waves are much more influenced by the β-term than shorter ones for a given velocity profile. It can be concluded that the β-effect will reduce the instability of westerly jets and increase the stability of easterly jets, especially at larger wavelengths, while at shorter wavelengths the β-effect is not so prominant. In Figure 45 is shown the growth rate as a function of wavenumber α and β for the symmetric sine-curve profile. It can be easily seen that the easterly current ($\beta < 0$) is made more unstable by the β-effect in a fan-shaped region at smaller α (larger L), while the westerly current ($\beta > 0$) is made more stable, especially at smaller α. For larger α, i.e., smaller wavelength, the β-effect is not prominant. There are some controversies over the existence of an upper critical wavelength L_o for the easterly current ($\beta < 0$). Nitta and

Yanai (1969) showed that in the case of easterlies the upper critical wavelength L_0 does not exist. In other words, there are no long neutral waves of Rossby and Haurwitz and all disturbances are unstable for wavelengths larger than $L_\varkappa$. Yamasaki and Wada (1972a) contended that there exists an upper critical wavelength for instability and the unstable waves may travel faster than the minimum velocity of the basic current (in dimensionless form c_r may be larger than 1). Kuo (1973) did not mention the upper critical wavelength. However, his figure did not show an upper critical wavelength for the easterly current. The author tested the problem by two different methods and found that there is indeed an upper critical wavelength. One method is to find the phase speed c as a function of β, setting $\alpha = 0$. It is found that for β approximately smaller than -0.409 the c_i vanishes. The result is shown in Table 7. Another method is to find the α as a function β after setting $c_i = 0$ and varying c_r from 1 to about 1.2. It is found that there is an upper critical wavelength beyond which the unstable wave becomes Rossby-Haurwitz wave and the unstable wave may travel with a phase speed c_r larger than 1. The numerical values of the calculated β, α and c_r are shown in Table 6 and plotted in Figure 45, as line A.

Kuo (1973) also noted the destabilization of the easterly ($\beta < 0$) sine-curve profile $U(y) = \sin \pi y$, $0 < y < 2$, by the influence of β. It is easily seen that if an easterly current with a continuous and differentiable profile has no critical point in the field of flow when $\beta = 0$, it may have critical points for $\beta < 0$. Thus, it is destablized by the β-effect, since this kind of jet has its $-U''$ everywhere positive in the field of flow and the $\beta(< 0)$ will overbalance $-U''$ to make $\beta - U''$

change sign in the field of flow.

Positive β will make the critical points closer to the boundary or the region where the shear is small, and away from each other, if there are two critical points for a bounded profile. The effect of negative β is just the inverse of positive β. Thus, the positive β will reduce the instability and negative β will increase the instability. However, if the magnitude of negative β is too large, it will bring the two critical points too close to each other such that the degree of instability will be reduced. Thus, for larger degrees of instability, the distance of critical points should not be too large or too small. Hence, it is intuitively concluded that the resistance of the critical points against being smoothed out plays an important role in estimating the growth rate.

The shear affects the instability through the equation for the time rate of change of kinetic energy (16) and the inequality for the upper bound on the growth rate $\alpha\ c_i$ (33). If a critical point is located in a region where shear is small, the c_i of the unstable wave due to this critical point is also small, since the critical point is easily smoothed out by successive applications of the smoother of the form (40).

The above discussion is only a heuristic approach. However, if we examine the distance between two critical points and the location of the critical points, we may estimate the growth rate of an unstable wave for a velocity profile.

CHAPTER X

BAROTROPIC INSTABILITY IN RELATION TO THE GENERATION OF TORNADOES AND SEVERE ATMOSPHERIC VORTICES

On 0000Z April 3, 1974, a remarkable cyclone development took place over western Kansas. This cyclone moved toward the northeast through Iowa and Wisconsin and reached its maximum intensity on 0000Z April 4 over eastern Wisconsin. During this period, a quasi-permanent anticyclone was located over Cuba and its intensity did not change. As the cyclone moved toward the northeast, the flow field between the cyclone and anticyclone was intensified and a jet developed over the region between the Mississippi and the Atlantic coast. Shortly after 0000Z April 4 a tornado outbreak took place over this area. In the early stage of cyclone development and the intensification of the flow field the underlying physical process was primarily the baroclinic instability. However, baroclinic instability alone could not account for the variations of the jet which played a significant role in the tornado outbreak in that area. Now let us consider the effect of barotropic instability, which in general rarely occurs in the middle latitudes. After the cyclone has developed due to baroclinicity, the barotropic process may account for the subsequent intensification of the flow field.

Table 8 shows the e-folding time of the most unstable wave, and the most preferred wavelength for each profile. Most of the most preferred wavelengths ofthe unstable waves are comparable to actual wavelengths in the pressure system shown in Figures 46-49, except the wind profiles at 850 MB 1200Z April 4, 700 MB 0000Z April 3 and 300 MB 1200Z April 3, which are significantly less than the dominant wavelength of the pressure system. This means that the actual growth rate for these profiles could be smaller.

In the linear theory assumed in this study, the growth rates represent only the initial growth. After the disturbances have grown to some extent the linear theory is no longer valid.

As already noted, the calculated growth rates may underestimate the actual growth rates of the disturbances. The artificial boundaries prevent the momentum transports necessary to maintain unstable disturbances. Furthermore, with artificial boundaries, the dimensional U_{min} may have been overestimated, which will reduce the value of growth rate. Thus, the actual e-folding times may be smaller than those shown in Table 8.

Thus, it is found that the atmosphere at all levels over the domain chosen is barotropically most unstable during 0000Z April 4, i.e., shortly before and at the time of the tornado outbreak, except at 850 MB, where its degree of instability was decreasing from 0000Z April 3. It is also found that the atmosphere at the upper level is barotropically more unstable than the lower level, which is generally accepted to be true.

In Figures 46-49 the dotted line in the domain chosen is the line where $\beta - \frac{\partial^2 u}{\partial y^2} = 0$. At the center part of the domain $\beta - \frac{\partial^2 u}{\partial y^2}$ is positive, while near the northwestern and southeastern boundaries it is negative. It is interesting to note that the hardest hit area (Indiana, Ohio, Kentucky, Tennesee and Alabama, which may be identified in the figures) was located just at the region in which the distance between the critical points is shortest. If we take the local u(x,y) as mean flow instead of the averaged U(y), it is found that this region is most unstable. Hence, the five states were confined to this most unstable area and were hardest hit by tornadoes.

The equation for the time rate of change of mean-flow kinetic energy

$$\frac{\partial \bar{E}}{\partial t} = \int \overline{u'v'} \; \frac{\partial U}{\partial y} \, dy \qquad (16a)$$

still holds approximately. The momentum transport is proportional to the tilting of troughs and ridges, as already noted. It is found from Figures 46-49 that the tilting of troughs and ridges was in a direction such that the mean-flow kinetic energy would decrease with respect to time. This means that the tilting of troughs and ridges, in relation to the position of the mean jet, was favorable for instability to occur.

From the above results it is concluded that barotropic instability may be synoptically associated with the generation of tornadoes and severe atmospheric vortices.

CHAPTER XI

CONCLUDING REMARKS

In middle latitudes, where baroclinicity predominates, the importance of barotropic instability, despite its simpler physical mechanism, is always overshadowed by the importance of baroclinic instability. Most studies have not associated barotropic instability with geophysical phenomena, possibly due to the fact that the geophysical applications of barotropic instability are now in their exploratory stage. The present work performed a barotropic instability analysis of wind profiles over the area hardest hit by the April 3-4 tornado outbreak. It was found that the atmosphere over this area was barotropically most unstable during this tornado outbreak. This result indicates the possibility that barotropic instability may have been synoptically associated with that outbreak. Additional case studies should be done to confirm the above results. Also, the relative importance of baroclinic and barotropic instability should be evaluated. Another promising area for future research would be to investigate whether the atmosphere over areas where tornadoes occur most often is barotropically unstable.

REFERENCES

Brown, R. A., 1972: On the Physical Mechanism of the Inflection Point Instability. J. Atmos. Sci., 29, 984-986.

Case, K. M., 1960: Stability of Inviscid Plane Couette Flow. Phys. Fluid, 3, 143-148.

Dickinson, R. E., and F. J. Clare, 1973: Numerical Study of the Unstable Modes of a Hyperbolic-Tangent Barotropic Flow. J. Atmos. Sci., 30, 1035-1049.

Dikii, L. A., 1960: The Stability of Plane Parallel Flows of an Ideal Fluid. Doklady Akad. Nauk SSSR, 135, 1068-1071.

Drazin, P. G., and L. N. Howard, 1966: Hydrodynamic Stability of Parallel Flow of Inviscid Fluid. Adv. Appl. Mech., 9, 1-89.

Eliassen, A., and E. Kleinschmidt, 1957: Dynamic Meteorology. Encyclopedia of Physics, 48, 1-154.

Fjortoft, R., 1950: Application of Integral Theorems in Deriving Criteria of Stability for Laminar Flows and for the Baroclinic Circular Vortex. Geofys. Publ., 17, No. 6, 1-52.

Foote, J. R., and C. C. Lin, 1950: Some Recent Investigations in the Theory of Hydrodynamic Stability. Quart. Appl. Math., 8, 265-280.

Haltiner, G. J., 1971: Numerical Weather Prediction. John Wiley & Sons, New York, 317 pp.

_______, and R. T. Song, 1962: Dynamic Instability in Barotropic Flow. Tellus, 14, 383-393.

Hoiland, E., 1953: On Two Dimensional Perturbation of Linear Flow. Geofys. Publ., 18, No. 9, 1-12.

Howard, L. N., 1961: Note on a Paper of John M. Miles. J. Fluid Mech., 10, 509-512.

_______, and P. G. Drazin, 1964: On Instability of Parallel Flow of Inviscid Fluid in a Rotating System with Variable Coriolis Parameter. J. Math Phys., 43, 83-99.

Jacobs, S. J., and A. Wiin-Nielsen, 1966: On the Stability of a Barotropic Basic Flow in a Stratified Atmosphere. J. Atmos. Sci., 23, 682-687.

Kuo, H. L., 1949: Dynamic Instability of Two-Dimensional Nondivergent Flow in a Barotropic Atmosphere. J. Meteor., 6, 105-122.

_______, 1951: Dynamical Aspects of the General Circulation and the Stability of Zonal Flow. Tellus, 3, 268-284.

_______, 1973: Dynamics of Quasigeostrophic Flows and Instability Theory. Adv. Appl. Mech., 13, 247-330.

Lin, C. C., 1955: The Theory of Hydrodynamic Stability. Cambridge University Press, 155 pp.

Lipps, F. B., 1962: The Barotropic Stability of the Mean Wind in the Atmosphere. J. Fluid Mech., 12, 397-407.

_______, 1963: Stability of Jets in a Divergent Barotropic Fluid. J. Atmos. Sci., 20, 120-129.

_______, 1965: The Stability of an Asymmetric Zonal Current in the Atmosphere. J. Fluid Mech., 21, 225-239.

_______, 1970: Barotropic Stability and Tropical Disturbances. Mon. Wea. Rev., 98, 122-131.

Lorenz, E. N., 1972: Barotropic Instability of Rossby Wave Motion. J. Atmos. Sci., 29, 258-264.

Myers, G. E., 1971: Analytic Methods in Conduction Heat Transfer. McGraw-Hill, New York, 508 pp.

Nitta, T., and M. Yanai, 1969: A Note on the Barotropic Instability of the Tropical Easterly Current. J. Meteor. Soc. Japan, 47, 127-130.

Pedlosky, J., 1963: Baroclinic Instability in Two Layer Systems. Tellus, 15, 20-25.

Rayleigh, Lord, 1880: On the Stability or Instability of Certain Fluid Motions. Scientific Papers, 1, 474-487, Cambridge University Press.

_______, 1913: On the Stability of the Laminar Motion of an Inviscid Fluid. Scientific Papers, 6, 197-204, Cambridge University Press.

Reid, W. H., 1965: The Stability of Parallel Flows. Basic Development in Fluid Dynamics, Maurice Holt, Editor, Vol. I, 249-307.

Shapiro, R., 1970: Smoothing and Filtering, and Boundary Effects. Rev. Geophys. Space Phys., 8, 359-387.

Stern, M., 1961: The Stability of Thermoclinic Jet. Tellus, 13, 503-508.

Taylor, G. I., 1915: Eddy Motion in the Atmosphere. Phil. Trans. Roy. Soc. A., 215, 1-26.

Tollmien, W., 1935: Ein Allgemeines Kriterium der Instabilitat Laminarer Geschwindigkeitsverteilungen. Nachr. Ges. Wiss. Gottingen, Math-Phys. Klasse, 50, 79-114.

Wiin-Nielsen, A., 1961: On the Short and Long-Term Variations in Quasi-Barotropic Flow. Mon. Wea. Rev., 89, 461-476.

Yamasaki, M., and M. Wada, 1972a: Barotropic Instability of an Easterly Zonal Current. J. Meteor. Soc. Japan, 50, 110-120.

_______, 1972b: Vertical Structure of the Barotropic Unstable Wave in a Tropical Easterly Current. J. Meteor. Soc. Japan, 50, 271-284.

Yanai, M., and T. Nitta, 1968: Finite Difference Approximation for the Barotropic Instability Problem. J. Meteor. Soc. Japan, 46, 389-403.

Yih, C. S., 1969: Fluid Mechanics. McGraw-Hill, New York, 622 pp.

APPENDIX

FINITE DIFFERENCE SCHEME

A. Real Part and Imaginary Part of Phase Speed

We divide the channel $0 < y < 2$ into N subdivisions of width $2/N$ by $N-1$ equally spaced points within the channel. After we write φ'' and U'' in difference representations

$$\varphi'' \approx \frac{N^2}{4} (\varphi_{j+1} + \varphi_{j-1} - 2\varphi_j)$$

$$U'' \approx \frac{N^2}{4} (U_{j+1} + U_{j-1} - 2U_j) \equiv \frac{N^2}{4} U''_j \quad ,$$

the equation

$$(U-c)\ (\varphi'' - \alpha^2\varphi) + (\beta - U'')\ \varphi = 0 \qquad (21)$$

becomes

$$a^2\, U_j\, \varphi_{j-1} + (Z_j - 1^2\, U_j)\varphi_j + a^2\, U_j\, \varphi_{j+1}$$
$$- c(a^2\, \varphi_{j-1} - 1^2\, \varphi_j + a^2\, \varphi_{j+1}) = 0 \qquad j = 2,3,\ldots,N \qquad (A1)$$

where

$$a^2 = \frac{N^2}{4}$$

$$1^2 = \alpha^2 + 2a^2$$

$$Z_j = \beta - a^2\, U''_j \quad .$$

If we use the boundary condtions

$$\varphi_1 = \varphi_{N+1} = 0 \quad ,$$

we get from (A1) a linear homogeneous system in $\varphi_2, \varphi_3, \ldots \varphi_N$.

This linear homogeneous system takes the form

$$(B - cD)\,P = 0 \quad , \qquad P = \begin{pmatrix} \varphi_2 \\ \varphi_3 \\ \vdots \\ \varphi_N \end{pmatrix}$$

where B is a square matrix of the form

$$B = \begin{pmatrix} Z_2-1^2U_2 & a^2U_2 & 0 & 0 \cdots\cdots & \\ a^2U_3 & Z_3-1^2U_3 & a^2U_3 & 0 \cdots\cdots & \\ 0 & a^2U_4 & Z_4-1^2U_4 & a^2U_4 & 0 \cdots \\ 0 & \ddots & \ddots & \ddots & \\ \vdots & & & & \end{pmatrix}$$

and D is a square matrix of the form

$$D = \begin{pmatrix} -1^2 & a^2 & 0 & 0 \cdots\cdots & & \\ a^2 & -1^2 & a^2 & 0 \cdots\cdots & & \\ 0 & a^2 & -1^2 & a^2 & 0 \cdots & \\ \vdots & 0 & a^2 & -1^2 & a^2 & 0 \cdots \\ \vdots & \vdots & & & & \end{pmatrix}$$

If D is nonsingular, we can write

$$(D^{-1}B - c\,I)\,P = 0 \quad ,$$

where D^{-1} is the inverse of D and I the unit matrix. The condition for a nontrivial solution of P is

$$\text{Det}\,(D^{-1}B - c\,I) = 0$$

Thus, the phase speeds c are the eigenvalues of the matrix $D^{-1}B$ and the amplitude functions φ in P are similarly its eigenvectors. When we divide the interval into N subdivisions, we get N-1 series of the phase speeds c. When unstable waves exist, phase speeds $c_i \neq 0$ are obtained as comples conjugates.

B. Lower and Upper Critical Wavelength $L_\varkappa$, L_o

The equations (34) and (35) may be written in

$$\varphi'' + \frac{\beta - U''}{U-c}\varphi - \alpha^2\varphi = 0 . \qquad \text{(B1)}$$

The finite difference form of the above equation is

$$a^2\varphi_{j-1} + \left(\frac{Z_j}{U_j - c} - 2a^2\right)\varphi_j + a^2\varphi_{j+1} - \alpha^2\varphi_j = 0\ , \quad j = 2,3,\ldots,N \qquad \text{(B2)}$$

where again,

$$a^2 = \frac{N^2}{4}$$

$$Z_j = \beta - a^2\,U''_j$$

With the boundary conditions

$$\varphi_1 = \varphi_{N+1} = 0 .$$

(B2) can be written in matrix form

$$(A - \alpha^2 I)\, P = 0$$

where

$$A = \begin{pmatrix} \frac{Z_2}{U_2-c} - 2a^2 & a^2 & 0 & 0 & \cdots & \\ a^2 & \frac{Z_3}{U_3-c} - 2a^2 & a^2 & 0 & & \\ 0 & a^2 & \frac{Z_4}{U_4-c} - 2a^2 & a^2 & 0 & \\ \vdots & & & \ddots & & \end{pmatrix}$$

and

$$P = \begin{pmatrix} \varphi_2 \\ \varphi_3 \\ \vdots \\ \varphi_N \end{pmatrix}$$

Hence, α^2 are eigenvalues of A and φ in P are the corresponding eigenfunctions. If we set $c = U_\kappa$, the lower critical wavelength can be found. U_κ are interpolated linearly by

$$U_\kappa = U_j + \frac{Z_j}{Z_j - Z_{j+1}} (U_{j+1} - U_j)$$

where $Z_j = \beta - a^2 U''_j$. Z_j and Z_{j+1} are of opposite sign.

If we set $c = 0$, we obtain the upper critical wavelength L_o for a westerly basic current ($\beta < 0$). For an easterly current ($\beta > 0$) there arise some problems in determining L_o by setting $c = 1$. For an easterly basic current with symmetric sine-curve profile

$$U(y) = \tfrac{1}{2}\,(1 - \cos \pi y), \quad 0 < y < 2 \ ,$$

we can find L_o as the minimum value of $L = L(c)$ by varying c from 1 to, say, 1.2 with a specified β. The results are shown in Table 6 and Figure 45.

It should be noted that the matrix A is real symmetric. There are some theorems on the real symmetric matrix:

a. Two eigenvectors of a real symmetric matrix, corresponding to different eigenvalues, are orthogonal.

b. The eigenvalues of such a matrix are always real.

C. Numerical Solutions of Eigenvalue Problems

The numerical method of solving eigenvalue problems was coded in FORTRAN as EISPAC and run on the IBM 370 at the Education and Research Computing Center, University of Oklahoma.

D. Accuracy of Finite Difference Methods

It is found that the best method to test the accuracy of the finite difference scheme is to compare the numerical values of $\frac{\partial U}{\partial t}$ calculated by

$$\frac{\partial U}{\partial t} = \tfrac{1}{2}\,\alpha(\varphi_r\,\varphi_i'' - \varphi_i\,\varphi_r'')\,e^{2\alpha c_i t} \tag{27a}$$

and those calculated by

$$\frac{\partial U}{\partial t} = - \frac{\alpha c_i}{2} \frac{(\beta - U'')|\varphi|^2}{|U-c|^2} e^{2\alpha c_i t} \tag{27b}$$

The maximum root mean square of difference is 0.7935×10^{-3}. The maximum percentage error is less than 0.01%. Therefore, the accuracy is satisfactory.

E. Finite Element Method

The equation

$$(U-c)\ (\varphi'' - \alpha^2\varphi) + (\beta - U'')\ \varphi = 0 \tag{21}$$

together with the boundary conditions

$$\varphi = 0 \quad \text{at} \quad y = 0, \; y = 2$$

can be transformed into a variational problem $\delta I = 0$ where

$$I = \int_0^2 [(\varphi')^2 + Q\ \varphi^2]\ dy \quad . \tag{E1}$$

with $Q = \alpha^2 - \frac{\beta - U''}{U-c}$. It follows that the problem of determining the solution of (21), subject to the boundary conditions, is equivalent to the problem of determining the functions satisfying the boundary conditions, which render (E1) stationary. This variational principle can be used to formulate finite-element method to find the solution numerically. A simple treatment of finite element formulation is found in Myers, 1971. The result is

$$\left(3a^2 - \frac{Q^{(p)}}{2}\right) \varphi_{j-1} - \left(6a^2 + Q^{(p)} + Q^{(q)}\right) \varphi_j$$

$$+ \left(3a^2 - \frac{Q^{(q)}}{2}\right) \varphi_{j+1} = 0 \qquad j = 2, \ldots, N \qquad \text{(E2)}$$

where

$$a^2 = \frac{N^2}{4}$$

and $Q^{(p)}$ is the value of Q in the element p between grid points j-1 and j and $Q^{(q)}$ is the value of Q in the element q between grid points j and j+1. We may take $Q^{(p)} = Q_{j-\frac{1}{2}}$ and $Q^{(q)} = Q_{j+\frac{1}{2}}$. Thus, (E2) is equivalent to the

$$A\,P = 0$$

where

$$P = \begin{pmatrix} \varphi_2 \\ \varphi_3 \\ \cdot \\ \cdot \\ \cdot \\ \varphi_N \end{pmatrix}$$

and A is an (N-1) X (N-1) matrix whose elements are

$$A_{j-1,j-1} = -\left(6a^2 + Q_{j-\frac{1}{2}} + Q_{j+\frac{1}{2}}\right) \qquad j = 2, \ldots, N$$

$$A_{j-2,j-1} = 3a^2 - \tfrac{1}{2} Q_{j-\frac{1}{2}} \qquad j = 3, 4, \ldots, N$$

$$A_{j-1,j} = 3a^2 - \tfrac{1}{2} Q_{j+\frac{1}{2}} \qquad j = 2, 3, \ldots, N-1$$

all other $\quad A_{ij} = 0$

Determining the eigenvalue α or c of (E1) amounts to finding the complex roots of the function $F(c,\alpha) = \det[A(c,\alpha)]$ with c or α specified.

The finite-element method is proposed but not used for finding the stability characteristics in this study.

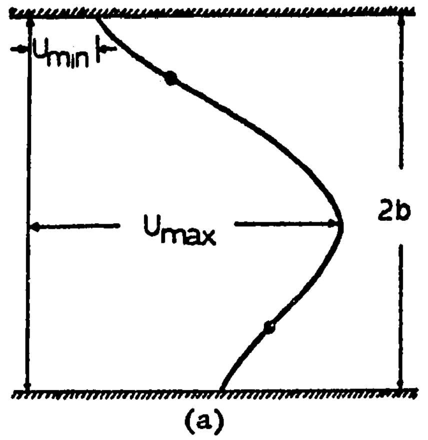

Figure 1. An atmospheric wind profile. The critical points are denoted by black dots. (a) dimensional profile, (b) dimensionless and normalized profile.

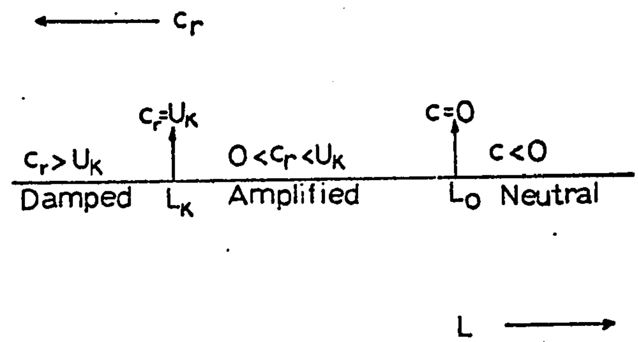

Figure 2. Distribution of damped, amplified, and neutral waves as related to basic current and wavelength for a westerly jet.

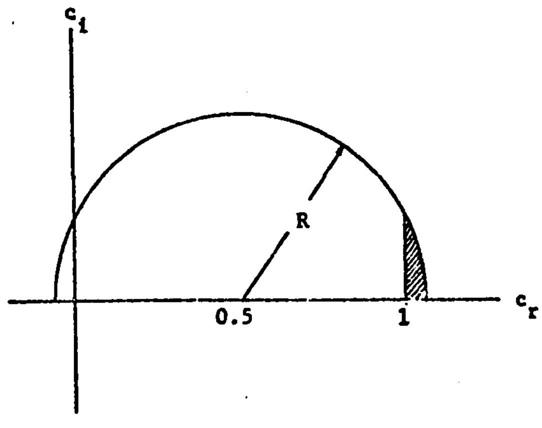

Figure 3. Howard's semicircle theorem for westerlies ($\beta > 0$). The complex phase speed must lie in the semicircle in the complex velocity plane. The shaded region is not a possible region for c. The radius of the semicircle is given by $R = \frac{1}{2}(1 + \beta / \alpha^2)$.

y(95.2km)	U(y)(m/sec)	U(y)	β-U''(10^{-11}/sec-m)
0	18.205	0.048	—
0.1	18.759	0.079	-1.267
0.2	19.596	0.125	-3.229
0.3	20.894	0.198	-3.141
0.4	22.645	0.296	-3.604
0.5	24.891	0.421	-4.354
0.6	27.700	0.578	-2.777
0.7	30.929	0.758	8.166
0.8	33.585	0.907	15.200
0.9	35.030	0.987	15.266
1.0	35.258	1.000	16.258
1.1	34.179	0.940	14.924
1.2	31.914	0.813	7.132
1.3	29.170	0.660	-0.849
1.4	26.671	0.520	-1.289
1.5	24.457	0.397	-2.392
1.6	22.628	0.295	-0.716
1.7	21.032	0.205	0.805
1.8	19.531	0.122	-0.055
1.9	18.203	0.047	-3.417
2.0	17.353	0	—

$y_\varkappa = 0.63$	$U_\varkappa = 0.624$	$L_\varkappa = 1.570$
$y_\varkappa = 1.29$	$U_\varkappa = 0.676$	$L_\varkappa = 1.308$
$y_\varkappa = 1.29$	$U_\varkappa = 0.676$	$L_\varkappa = 3.501$
$y_\varkappa = 1.64$	$U_\varkappa = 0.253$	$L_\varkappa = 3.877$
$y_\varkappa = 1.79$	$U_\varkappa = 0.127$	$L_\varkappa = 4.452$

$L_o = 5.497$

Table 1. Dimensional and dimensionless U(y) and β-U'' at each grid point, and low critical wavelength $L_\varkappa$ and upper critical wavelength L_o calculated from (34) and (35), for the 500 MB 0000Z April 3 wind profile. Dimensional U(y) is plotted in Figure 34a and dimensionless U(y), in Figure 34b. The corresponding (c_r, c_i)-L diagram is shown in Figure 5.

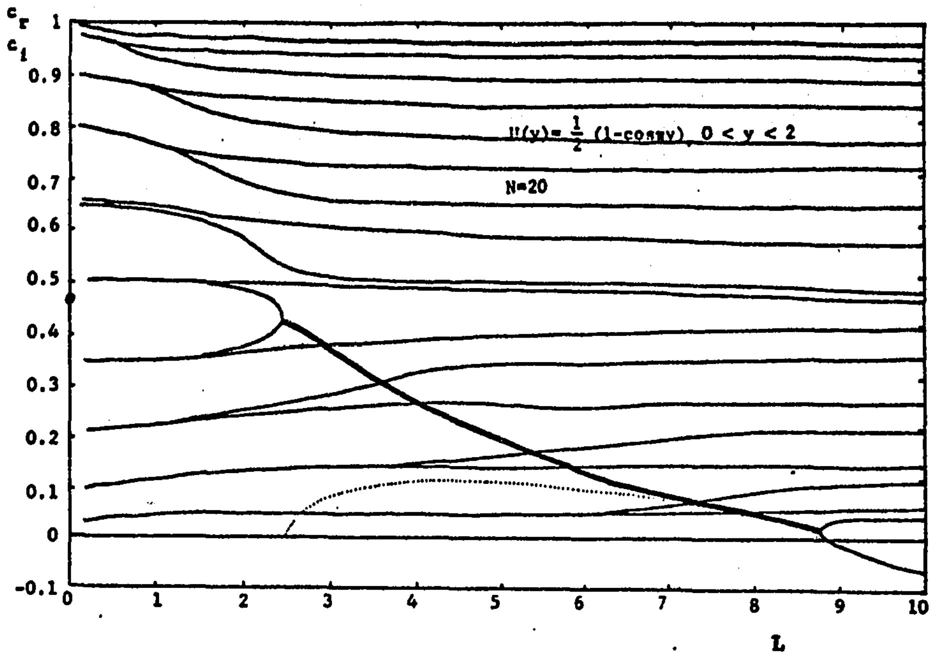

Figure 4. A (c_r,c_i)-L diagram for symmetric sine-curve velocity profile $U(y) = \frac{1}{2}(1-\cos \pi y)$ when $\beta = 0.375$ and $N = 20$. The thick solid line and the dotted line correspond to c_r and c_i of the unstable wave respectively. Black dot on the ordinate represents $U_\varkappa$.

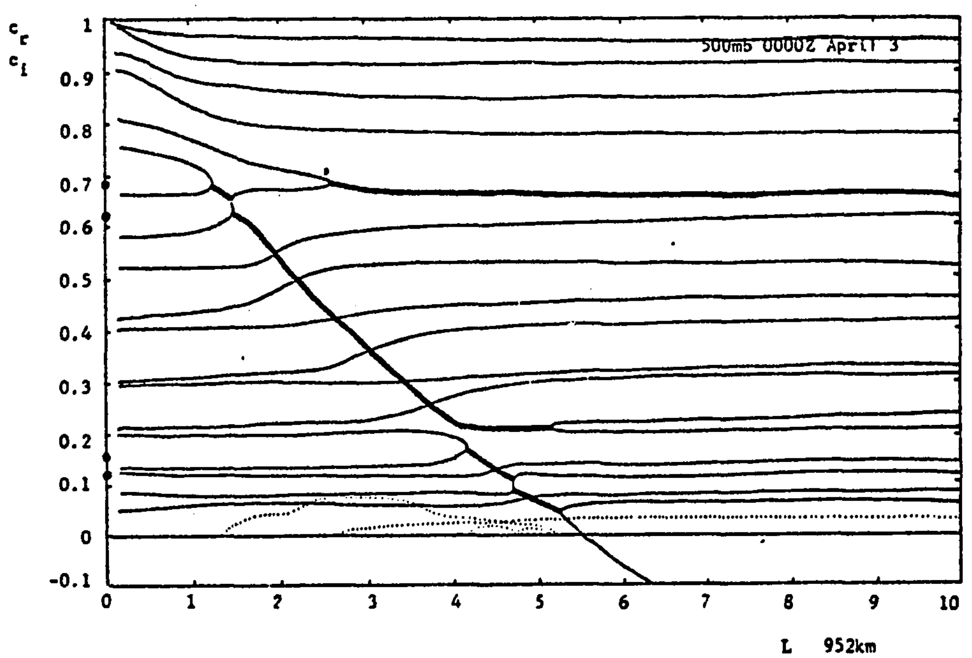

Figure 5. A (c_r,c_i)-L diagram for 500 MB 0000Z April 3 wind profile. The thick solid lines and the dotted lines correspond to c_r and c_i of unstable waves respectively. Black dots on the ordinate represent $U_\varkappa$'s.

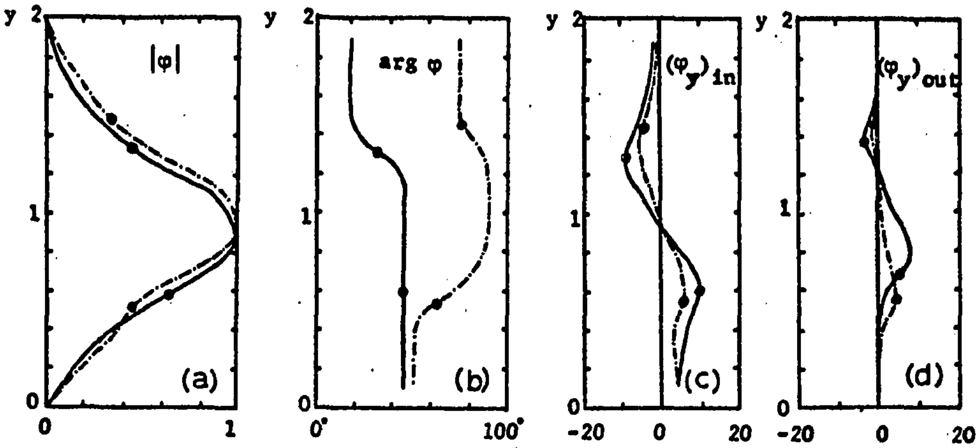

solid line L=1.8 c_r=0.587 c_i=0.0440

chain line L=2.6 c_r=0.434 c_i=0.0740

Figure 6. Unstable solutions for 500 MB 0000Z April 3 wind profile; (a) Absolute value of eigenfunction φ. (b) Phase of φ in degrees. (c) Derivatives of φ in phase with φ. (d) Derivatives of φ out of phase with φ. Note the singular behavior at the points, denoted by black dots, where c_r is equal to the velocity of the basic current.

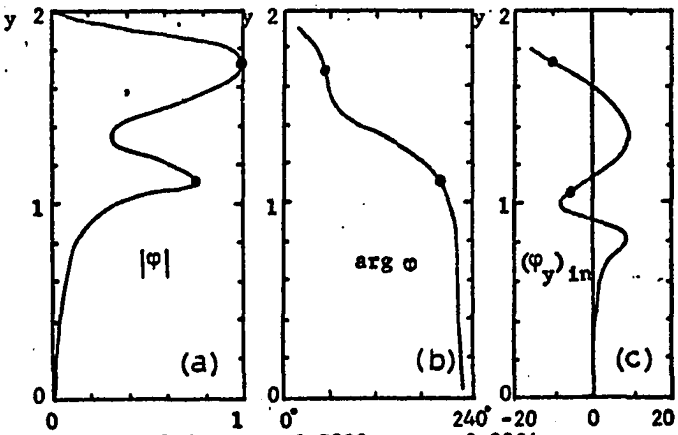

L=1.6 c_r=0.7329 c_i=0.0084

Figure 7. Unstable solution for 700 MB 0000Z April 3 wind profile. (a) Absolute value of eigenfunction φ. (b) Phase of φ in degrees. (c) Derivative of φ in phase with φ. Note the singular behavior at the points, denoted by black dots, where c_r is equal to the velocity of the basic current.

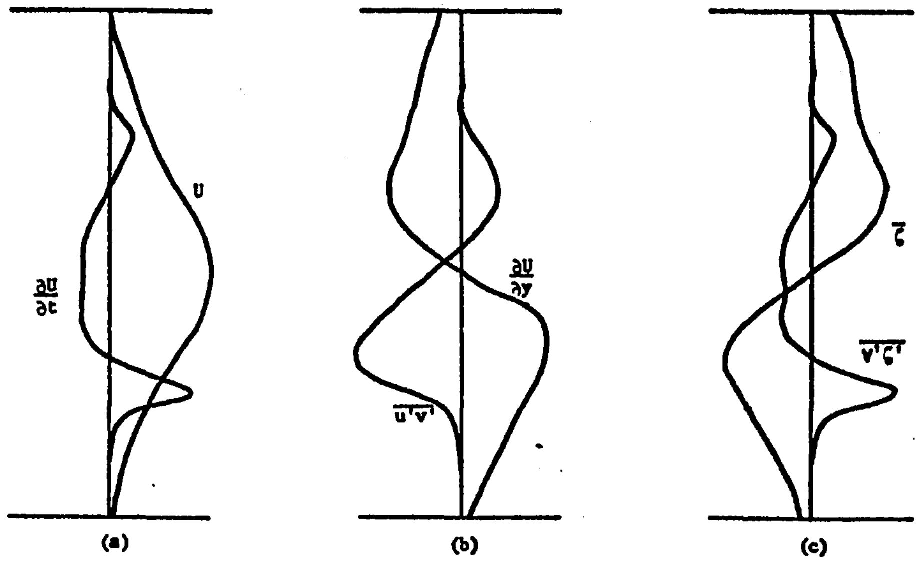

Figure 8. U, $\frac{\partial U}{\partial t}$, $\overline{u'v'}$, $\frac{\partial U}{\partial y}$, $\overline{\zeta}$ and $\overline{v'\zeta'}$ for 500 MB 0000Z April 3 wind profile.

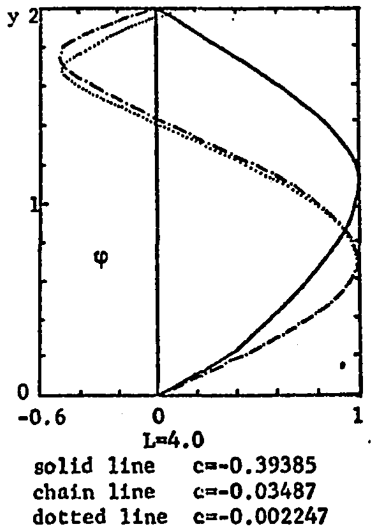

Figure 9. Rossby-Haurwitz wave solutions for 700 MB 0000Z April 3 wind profile.

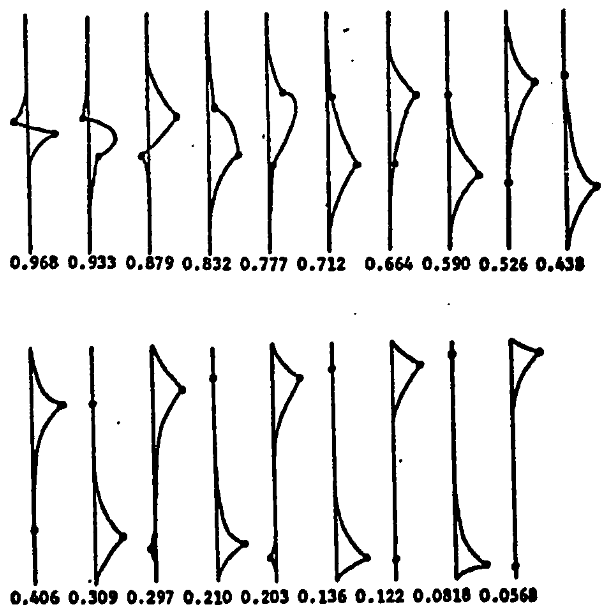

Figure 10. Eigenfunction φ of singular waves at L=1.0 for 500 MB 0000Z April 3 wind profile. Nondimensionalized phase velocities are shown below. The singular waves possess phase velocities equal to the basic current velocity at the points indicated by black dots.

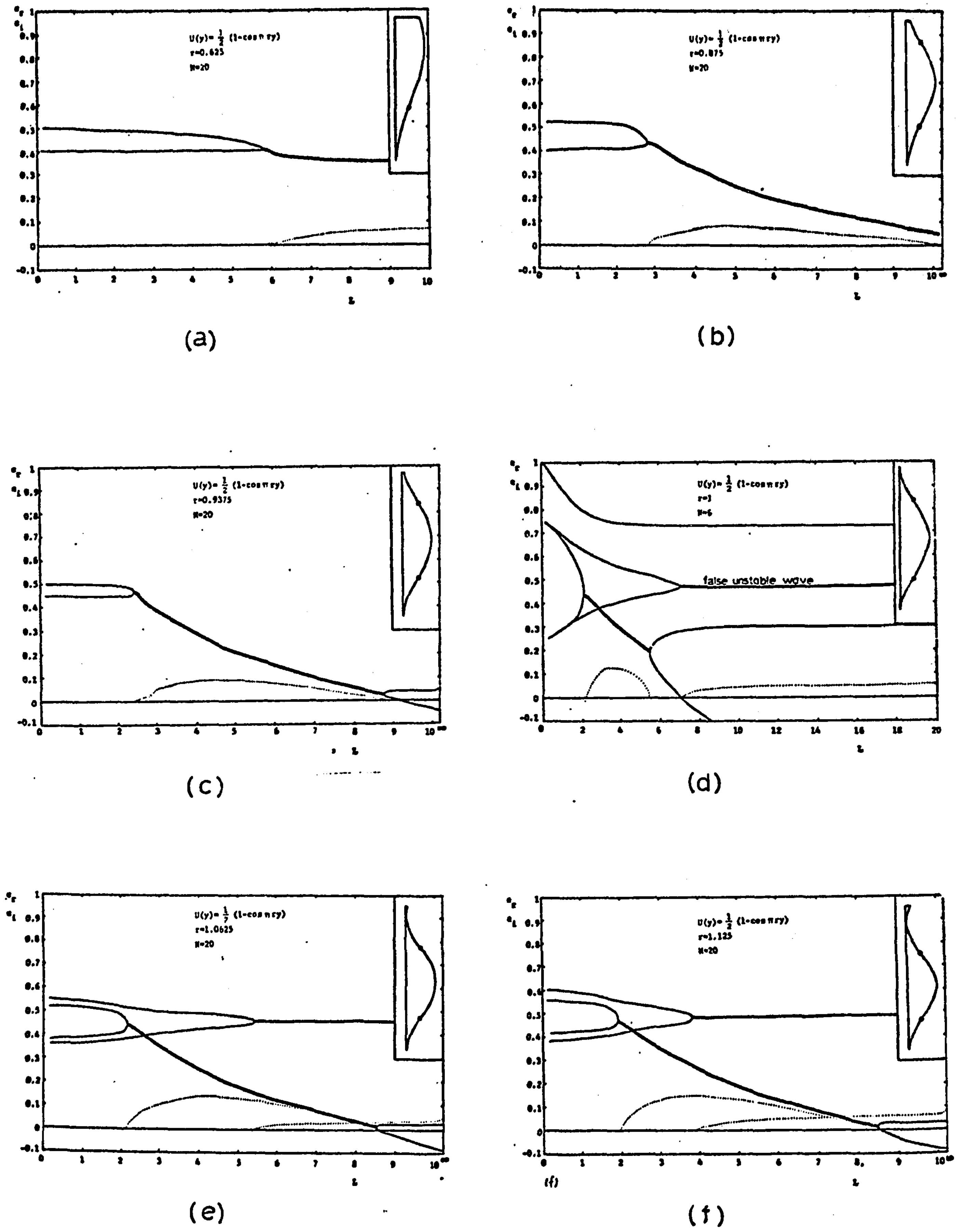

Figure 11. (Caption on next page.)

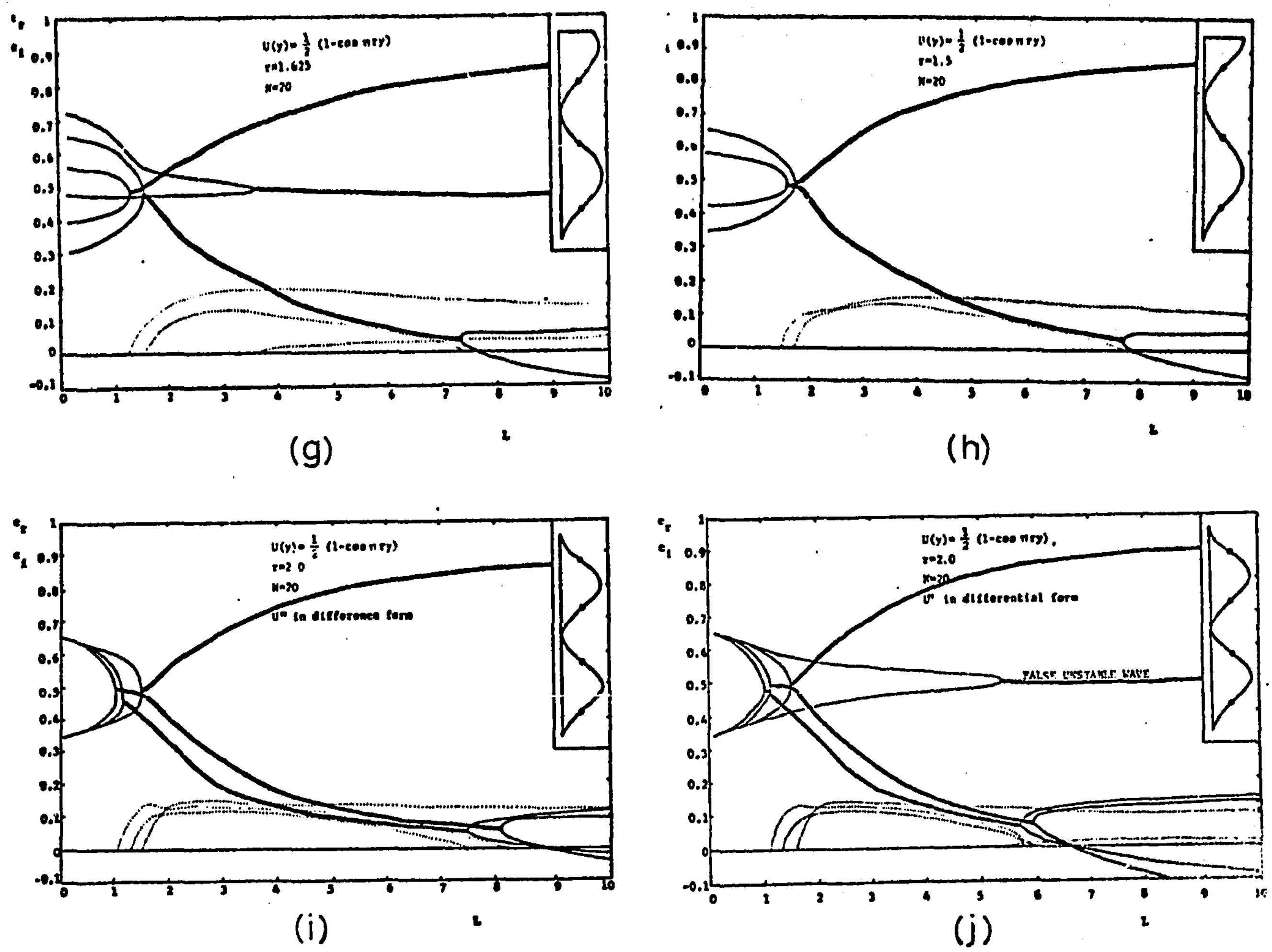

Figure 11. (c_r, c_i)-L diagrams for sine-curve velocity profile $U(y) = \frac{1}{2}(1 - \cos \pi r y)$, $0 < y < 2$, with various values of r.

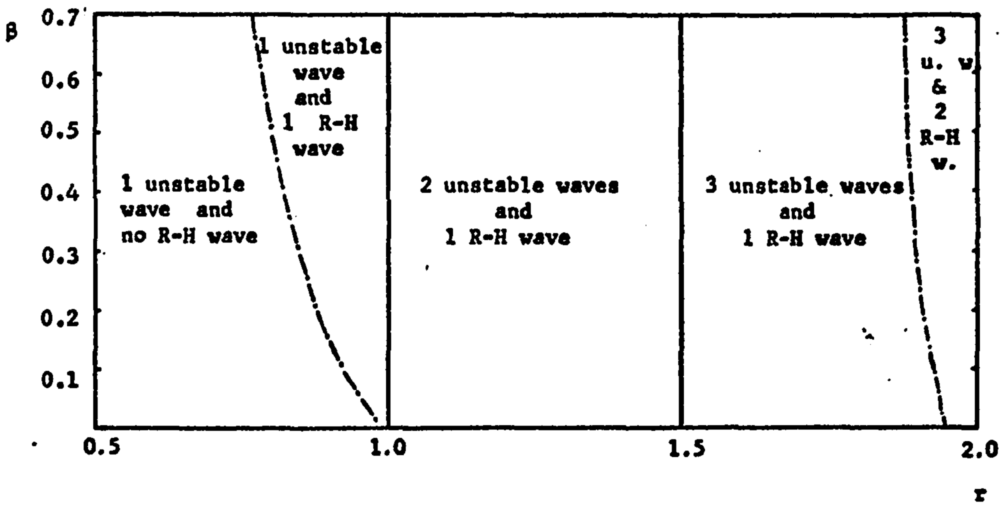

Figure 12. Number of unstable waves and R-H waves for sine-curve profile as a function of r and β.

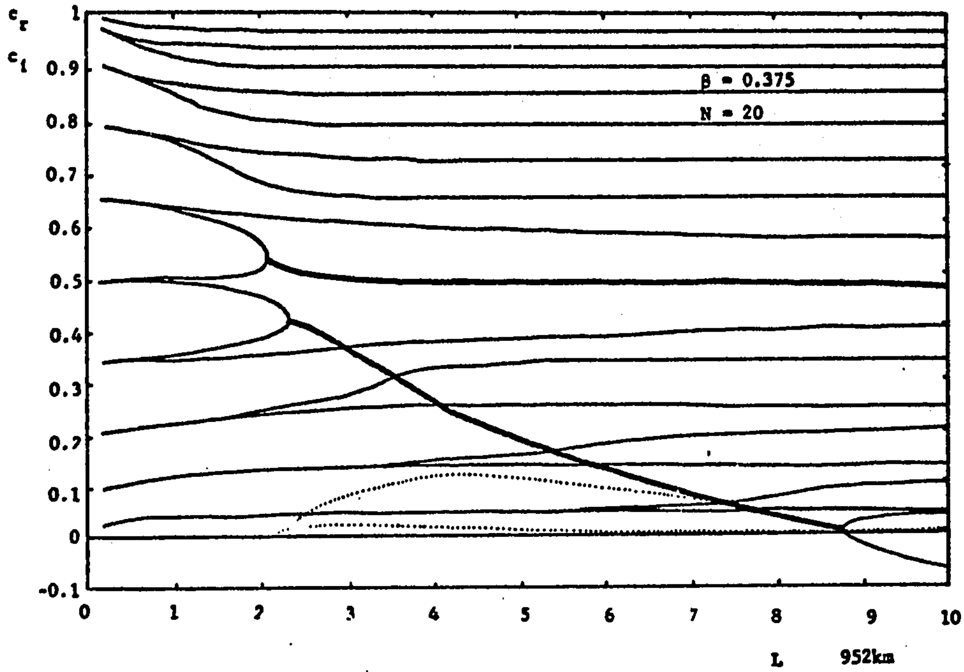

Figure 13a. A (c_r, c_i)-L diagram for symmetric sine-curve profile $U(y) = \frac{1}{2}(1 - \cos \pi y)$ when $\beta = 0.375$ and $N = 20$ and all the figures past hundredth in the numerical value of $U(y)$ are truncated. Compare this figure with Figure 4.

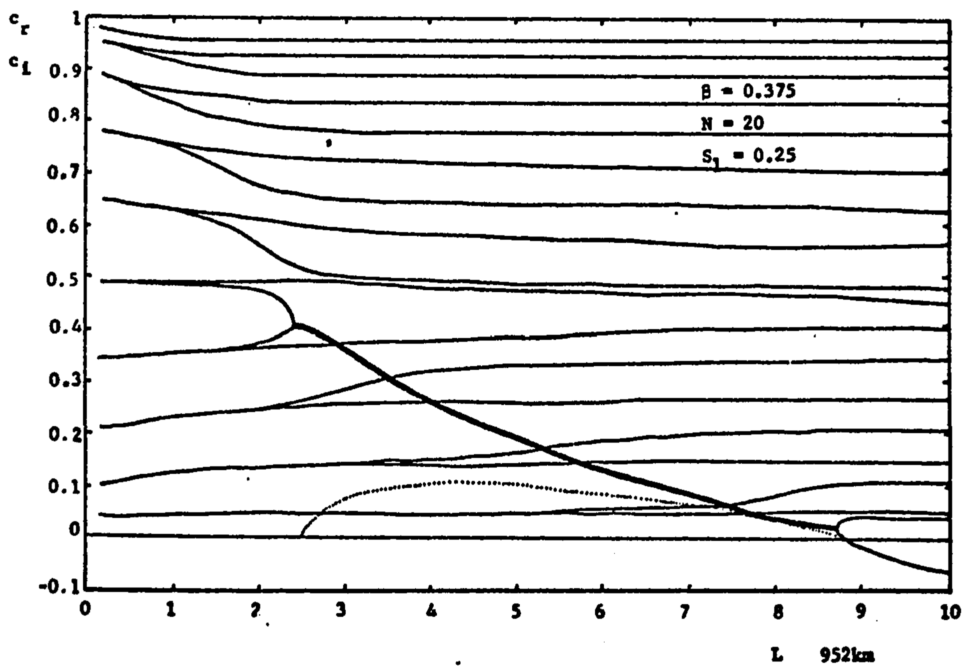

Figure 13b. A (c_r, c_i)-L diagram for a smoothed truncated symmetric sine-curve profile $U(y) = \frac{1}{2}(1 - \cos \pi y)$. Note that the unstable wave due to truncation has been eliminated by smoothing of the profile.

L	nonsmoothed	smoothed once	truncated		truncated smoothed once
1.0	0	0	0	0	0
1.5	0	0	0	0	0
2.0	0	0	0	0	0
2.5	—	0.024	0.025	0.041	0.028
3.0	0.078	0.075	0.081	0.021	0.077
3.5	—	0.092	0.099	0.019	0.095
4.0	0.110	0.106	0.113	0.017	0.108
4.5	—	0.109	0.116	0.016	0.111
5.0	0.111	0.106	0.113	0.015	0.107
5.5	—	0.090	0.105	0.014	0.099
6.0	0.095	0.088	0.096	0.013	0.090
6.5	—	0.078	0.086	0.012	0.080
7.0	0.071	0.064	0.073	0.011	0.066
7.5	—	0.046	0.057	0.010	0.048
8.0	0.040	0.032	0.041	0.0096	0.033
8.5	—	0.013	0.024	0.0088	0.014
9.0	0	0	0	0.0080	0
9.5	0	0	0	0.0072	0
10.0	0	0	0	0.0065	0
10.5	0	0	0	0.0057	0
11.0	0	0	0	0.0049	0
11.5	0	0	0	0.0039	0
12.0	0	0	0	0.0029	0
12.5	0	0	0	0.0012	0
13.0	0	0	0	0	0
13.5	0	0	0	0	0
corresponding (c_r, c_i)-L diagram is shown in:	Fig. 4	—	Fig. 13a		Fig. 13b

Table 2. The c_i of unstable waves calculated in various cases for the symmetric sine-curve profile $U(y) = \frac{1}{2}(1-\cos \pi y)$, $0 < y < 2$ when $\beta = 0.375$ and $N = 20$.

β	nonsmoothed N=20	smoothed once N=20	truncated N=20	truncated smoothed N=20	nonsmoothed N=40
1.5	4.40	4.36	4.39	4.35	4.40
0.75	6.25	6.20	6.24	6.19	6.25
0.5	7.67	7.61	7.66	7.60	—
0.375	8.87	8.80	8.85	8.78	8.86
0.3	9.92	9.84	9.90	9.82	9.92
0.25	10.87	10.78	10.84	10.76	—
0.2143	11.74	11.65	11.72	11.62	11.74
0.1875	12.55	12.45	12.53	12.43	—
0.1666	13.32	13.21	13.29	13.18	—
0.15	14.04	13.93	14.01	13.90	14.04

Values of L_0 as a function of β, calculated from (35)

β	nonsmoothed N=20	smoothed once N=20	truncated, N=20			truncated, smoothed once, S = 0.25		
1.5	2.35	2.36	2.55	2.23	14.74	2.41	2.34	—
0.75	2.35	2.36	2.35	2.05	5.62	2.39	2.27	—
0.5	2.35	2.36	2.41	2.07	5.97	2.42	2.19	8.22
0.375	2.35	2.36	2.44	2.08	6.19	2.44	2.06	4.87
0.3	2.35	2.36	2.46	2.09	6.34	2.45	1.78	3.52
0.25	2.35	2.36	2.48	2.09	6.46	2.46	1.17	2.85
0.2143	2.35	2.36	2.49	2.10	6.54	2.47	0.57	2.69
0.1875	2.35	2.36	2.49	2.10	6.61	2.48	2.26	—
0.1666	2.35	2.36	2.50	2.10	6.67	2.48	2.26	—
0.15	2.35	2.36	2.51	2.10	6.72	2.49	2.21	—

Theoretical value = 2.3094106

Values of L_x calculated from (34)

Table 3. The upper and lower critical wavelength calculated in various cases for the profile $U(y) = \frac{1}{2}(1-\cos \pi y)$, $0 < y < 2$.

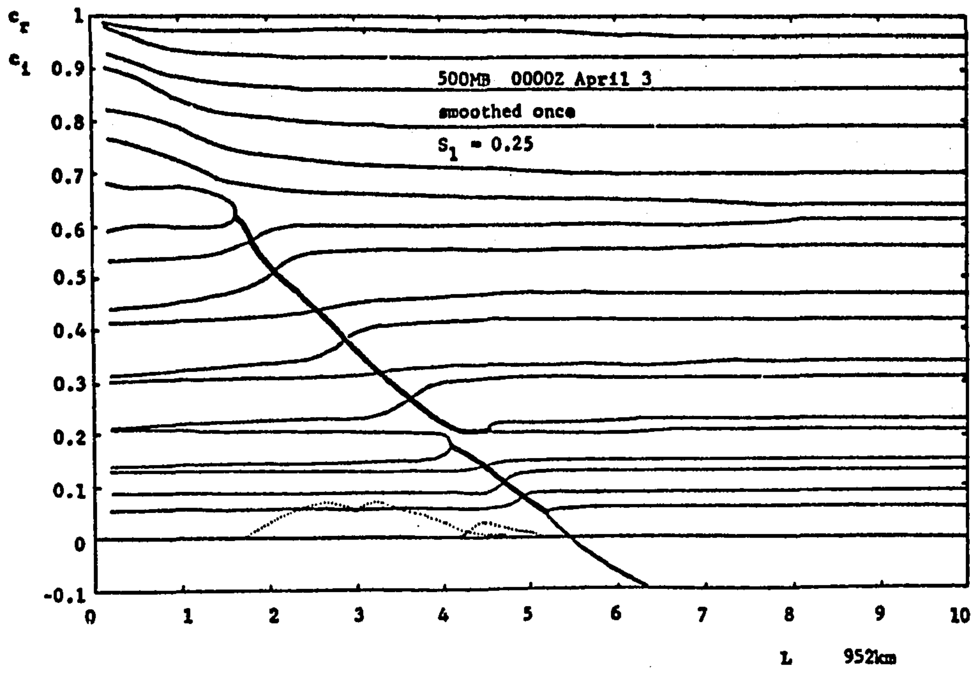

Figure 14a. A (c_r, c_i)-L diagram for 500 MB 0000Z April 3 wind profile smoothed once. Compare this figure with Figure 5.

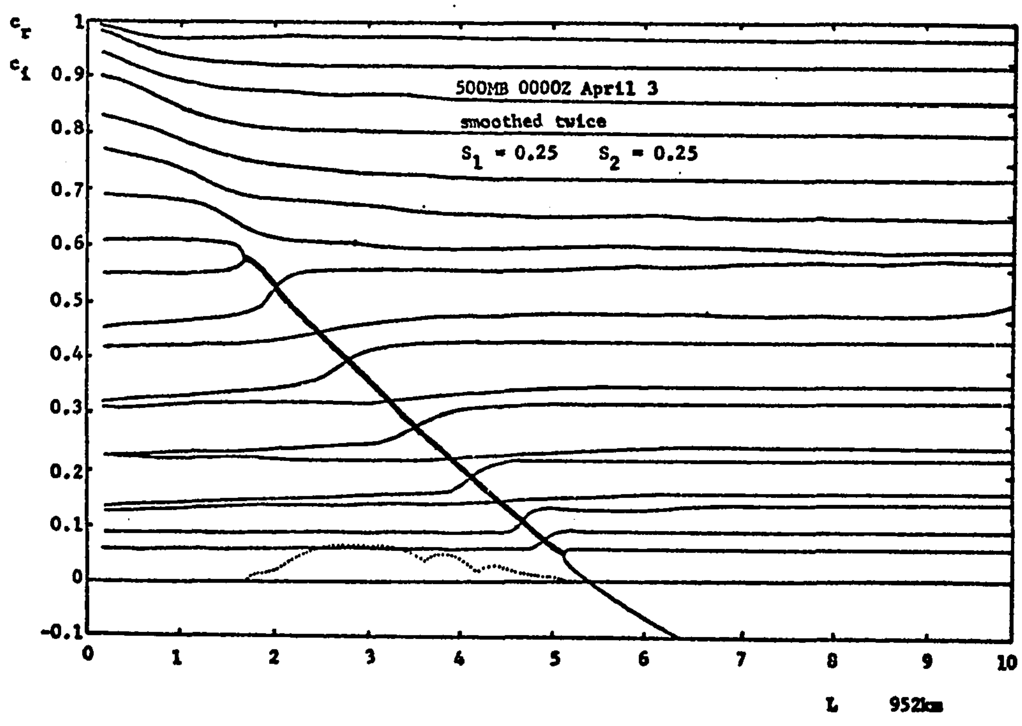

Figure 14b. A (c_r, c_i)-L diagram for 500 MB 0000Z April 3 wind profile smoothed twice. Compare this figure with Figure 14a and Figure 5.

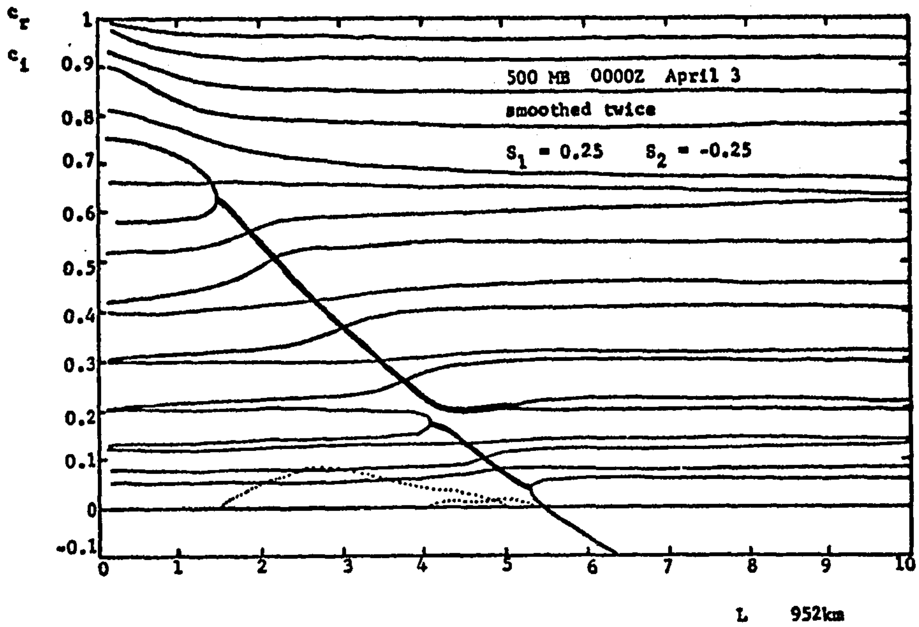

Figure 14c. A (c_r, c_i)-L diagram for 500 MB 0000Z April 3 wind profile smoothed twice. $S_1 = 0.25$ $S_2 = -0.25$.

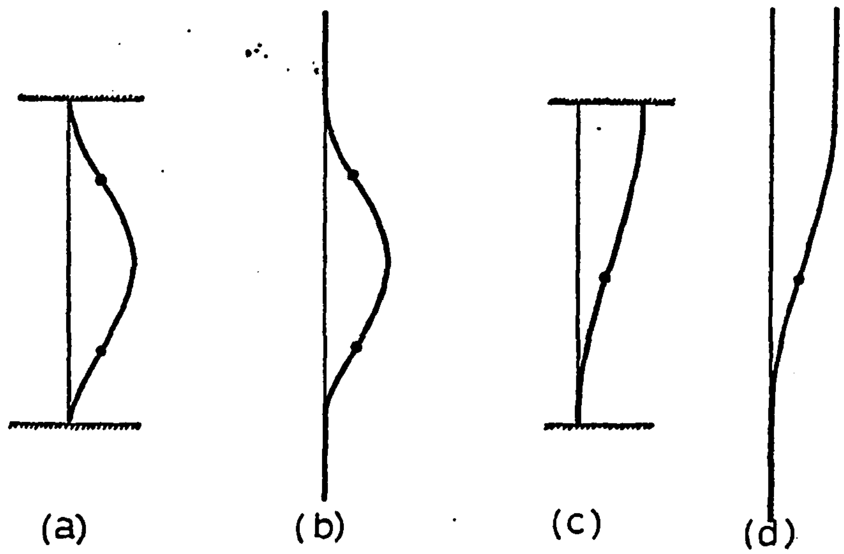

Figure 15. Symmetric and antisymmetric sine-curve profiles within rigid walls and extending to infinity.

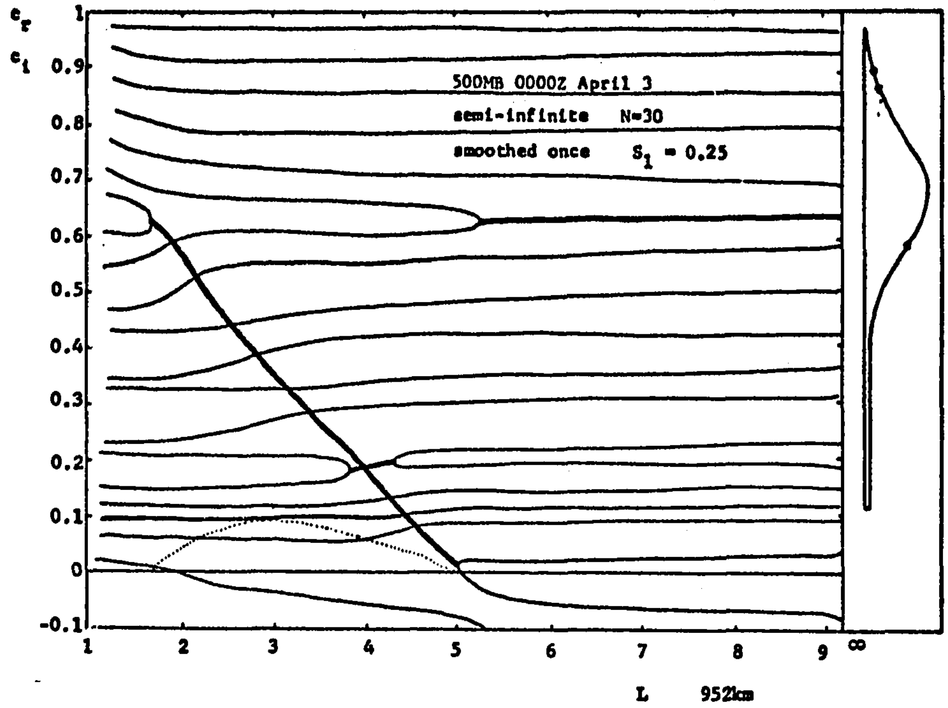

Figure 16a. A (c_r, c_i)-L diagram for 500 MB 0000Z April 3 wind profile when the lower boundary is extended to infinity and the resulting profile is smoothed once with $S_1 = 0.25$. Some of the singular waves are not shown.

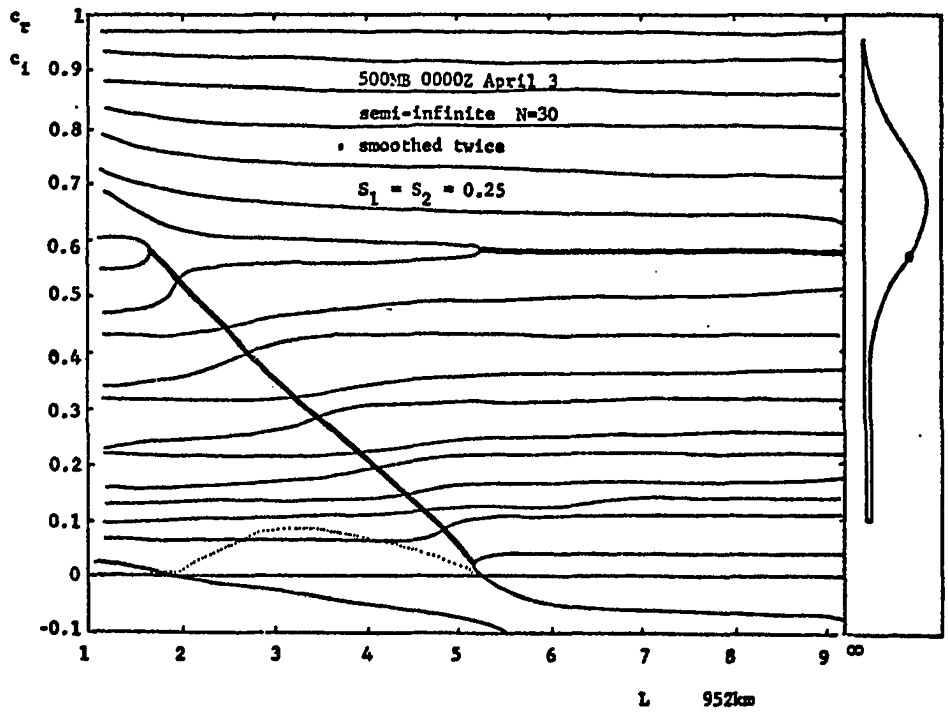

Figure 16b. A (c_r, c_i)-L diagram for 500 MB 0000Z April 3 wind profile when the lower boundary is extended to infinity and the resulting profile is smoothed twice with $S_1 = S_2 = 0.25$. Some of the singular waves are not shown.

L	bounded nonsmoothed			bounded, smoothed once, $S_1=0.25$		semiinfinite smoothed twice, $S_1=S_2=0.25$	semiinfinite smoothed once, $S_1=0.25$		semiinfinite smoothed twice, $S_1=S_2=0.25$
1.0	0	0	0	0	0	0	0	0	0
1.2	0	0	0	0	0	0	0	0	0
1.4	0.061	0	0	0	0	0	0	0	0
1.6	0.208	0	0	0	0	0	0	0	0
1.8	0.249	0	0	0.076	0	0.043	0.0737	0	0.054
2.0	0.201	0	0	0.143	0	0.043	0.155	0	0.132
2.2	0.238	0	0	0.241	0	0.216	0.275	0	0.246
2.4	0.289	0	0	0.270	0	0.235	0.303	0	0.266
2.6	0.290	0	0	0.260	0	0.218	0.297	0	0.259
2.8	0.268	0.034	0	0.230	0	0.195	0.283	0	0.265
3.0	0.232	0.047	0	0.211	0	0.204	0.280	0	0.269
3.2	0.213	0.054	0	0.205	0	0.193	0.269	0	0.255
3.4	0.195	0.057	0	0.181	0	0.162	0.246	0	0.231
3.6	0.161	0.059	0	0.140	0	0.123	0.218	0	0.208
3.8	0.113	0.060	0	0.116	0	0.117	0.193	0	0.187
4.0	0.100	0.060	0	0.098	0	0.093	0.164	0	0.157
4.2	0.063	0.060	0	0.030	0.032	0.047	0.126	0.0209	0.128
4.4	0.033	0.059	0.053	0.014	0.061	0.057	0.107	0.0169	0.103
4.6	0.033	0.059	0.022	0	0.049	0.038	0.083	0	0.075
4.8	0.033	0.058	0.015	0	0.016	0.013	0.057	0	0.043
5.0	0.009	0.057	0.043	0	0.024	0.012	0.034	0	0.0164
5.2	0	0.056	0.027	0	0	0	0	0	0
5.4	0	0.055	0	0	0	0	0	0	0.0089
5.6	0.0	0.053	0	0	0	0	0	0	0.0143
5.8	0	0.052	0	0	0	0	0.0129	0	0.0177
6.0	0	0.051	0	0	0	0	0.0183	0	0.0201
corresponding (c_r, c_i)-L diagram is shown in:	Fig. 5			Fig. 14a		Fig. 14b	Fig. 16a		Fig. 16b

Table 4. The growth rate in 1/day calculated in various cases for the 500 MB 0000Z April 3 wind profile.

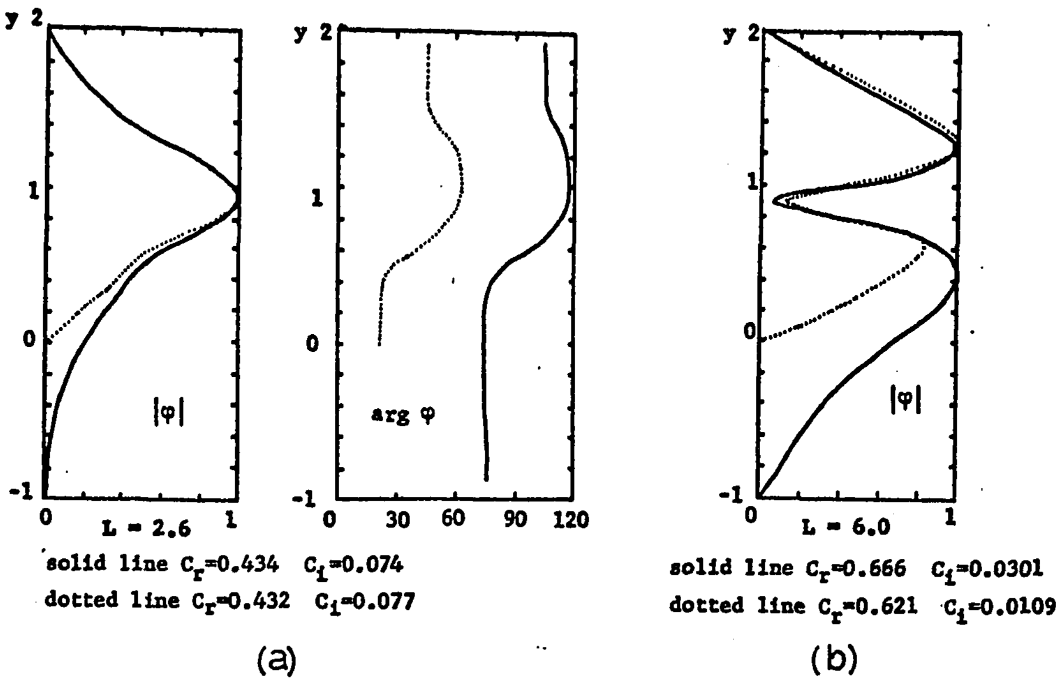

Figure 17. A comparison of the amplitude function of unstable waves for the 500 MB 0000Z April 3 (solid line) with that for corresponding extended profile (dotted line).

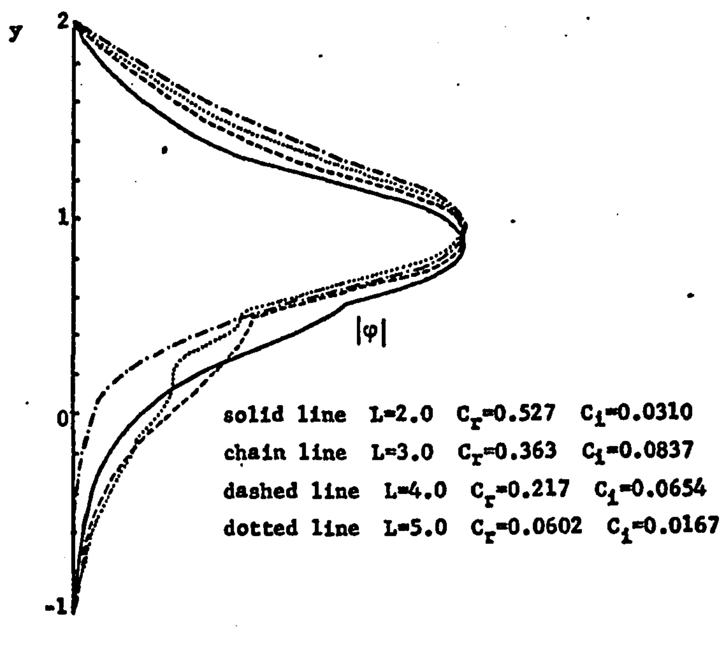

Figure 18. Absolute value of φ of an unstable wave at various wavelengths for extended 500 MB 0000Z April 3 wind profile. Note that the |φ|'s are confined in the shear-belt.

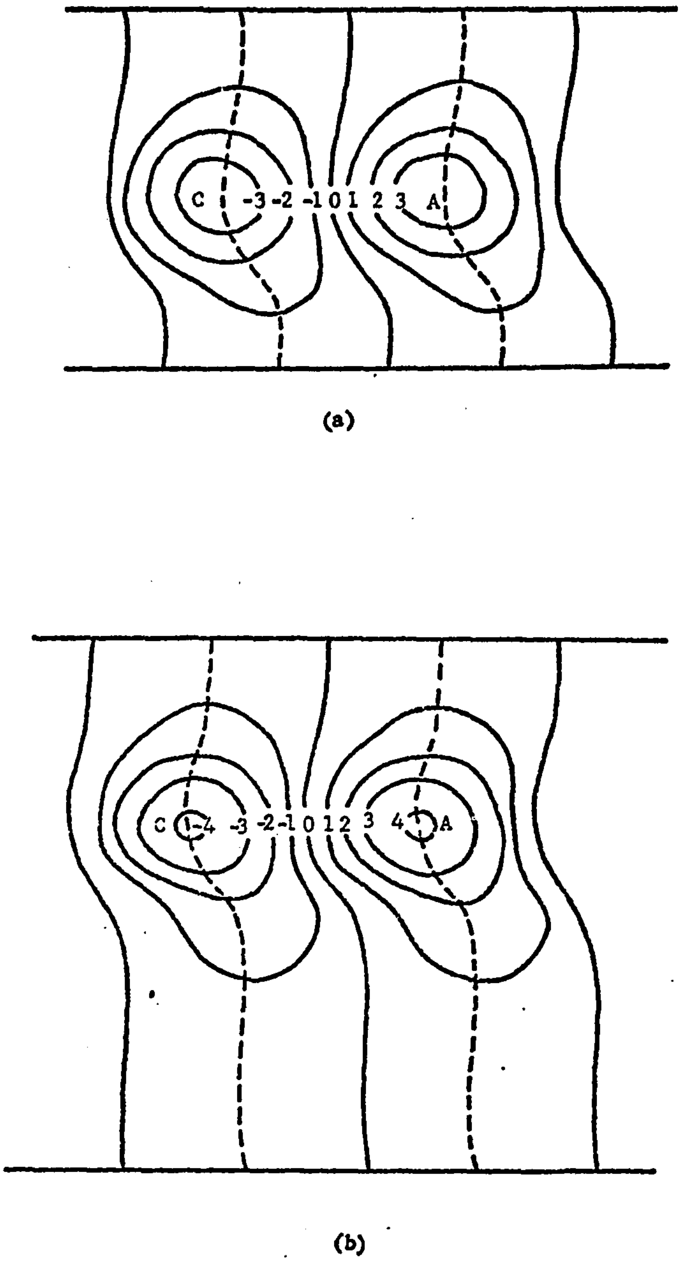

Figure 19. Disturbance stream function of most unstable wave at L=2.6 for 500 MB 0000Z April 3 wind profile. The primary centers of cyclonic and anticyclonic vorticity are marked by C and A. The dashed line shows where v' vanishes, i.e., trough and ridge lines. (a) case for bounded profile, (b) case for extended profile.

y	$\overline{u'v'}$		$\frac{\partial U}{\partial t}$, $\overline{v'\zeta'}$	
	bounded	extended	bounded	extended
-1	—	0	—	0
-0.9	—	0.0	—	-0.000
-0.8	—	0.0	—	-0.002
-0.7	—	0.0	—	-0.005
-0.6	—	0.001	—	-0.011
-0.5	—	0.003	—	-0.021
-0.4	—	0.006	—	-0.038
-0.3	—	0.011	—	-0.070
-0.2	—	0.021	—	-0.125
-0.1	—	0.038	—	-0.223
0	0	0.004	0	0.912
0.1	-0.002	-0.067	0.042	0.502
0.2	-0.033	-0.221	0.581	2.583
0.3	-0.169	-0.648	2.143	5.961
0.4	-0.824	-2.075	10.954	22.576
0.5	-5.612	-9.299	84.805	121.890
0.6	-10.736	-16.734	17.678	26.810
0.7	-10.453	-16.312	-23.355	-35.233
0.8	-7.697	-12.183	-31.760	-47.360
0.9	-4.717	-7.754	-27.844	-41.212
1.0	-1.892	-3.586	-28.641	-42.146
1.1	0.929	0.554	-27.785	-40.656
1.2	3.110	3.736	-15.846	-22.993
1.3	3.760	4.683	2.355	4.057
1.4	3.069	3.770	10.972	14.208
1.5	1.305	1.592	24.301	29.357
1.6	0.034	0.046	1.115	1.546
1.7	-0.009	-0.012	-0.263	-0.375
1.8	0.004	0.006	0.004	0.006
1.9	0.002	0.003	0.042	0.061
2.0	0	0	0	0

Table 5. The numerical values of momentum transport $\overline{u'v'}$ and vorticity transport $\overline{v'\zeta'}$ of the most unstable wave (L=2.6) for the bounded and extended 500 MB 0000Z April 3 wind profile. The unit is arbitrary. These values for the case of the bounded profile are plotted in Figure 8.

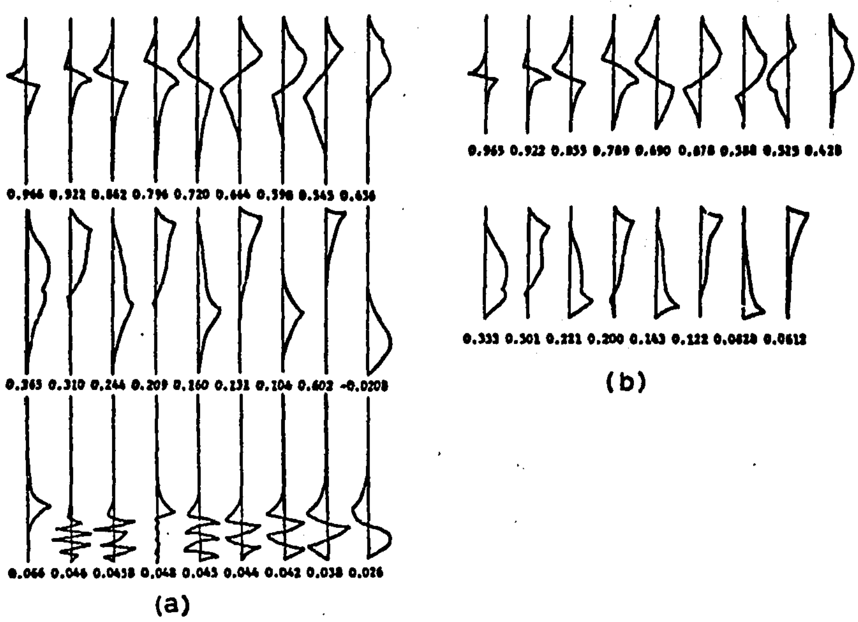

Figure 20. A comparison of the φ's of singular waves for bounded 500 MB 0000Z April 3 wind profile (a) and those for corresponding extended profile (b). Nondimensional normalized phase speeds are shown below.

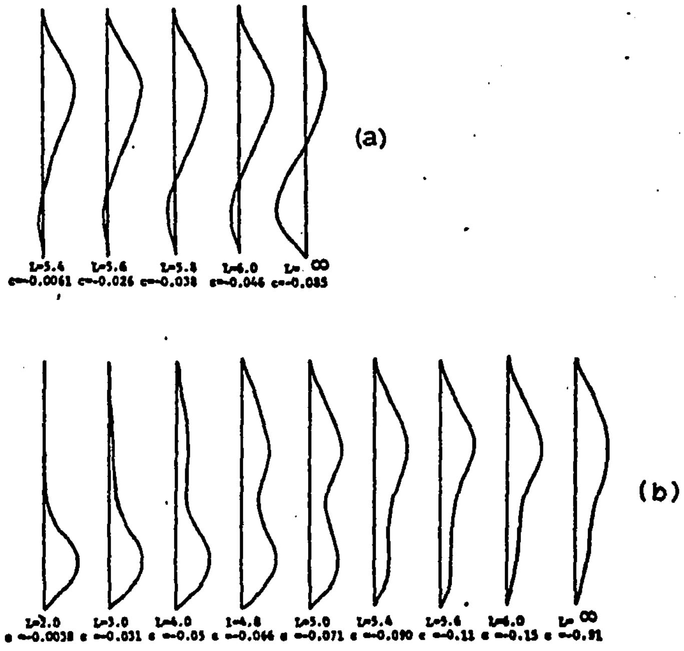

Figure 21a. Amplitude function φ of a Rossby-Haurwitz wave for 500 MB 0000Z April 3 wind profile.

Figure 21b. Amplitude function φ of Rossby-Haurwitz wave at various wavelengths due to the extension of lower boundary to infinity for 500 MB 0000Z April 3 wind profile.

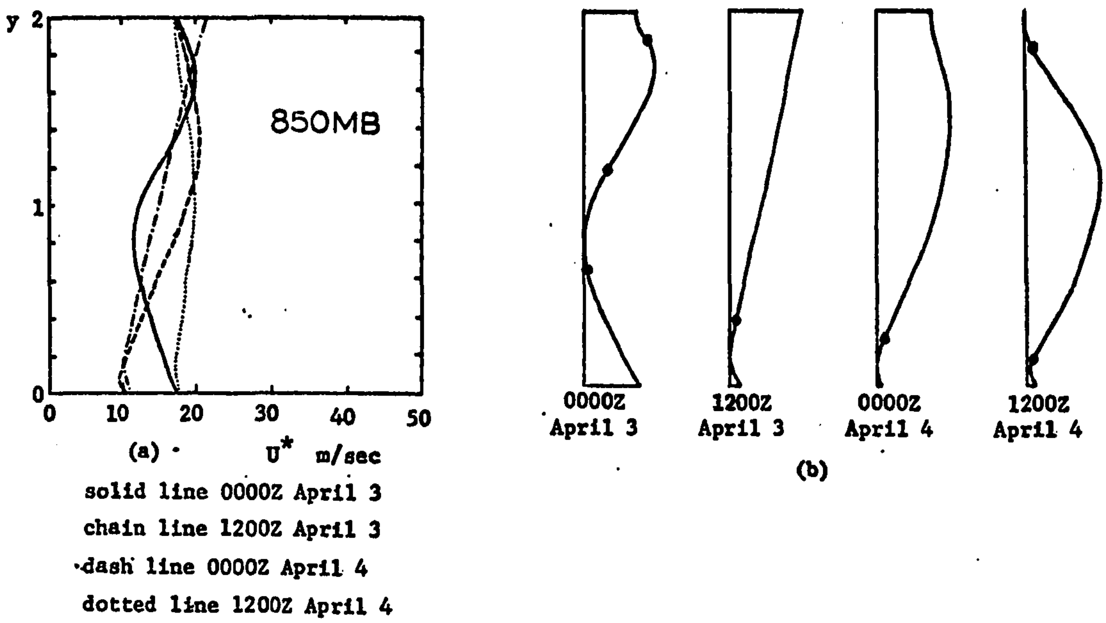

Figure 22. Atmospheric wind profiles at 850 MB. (a) dimensional profiles, (b) dimensionless and normalized profiles.

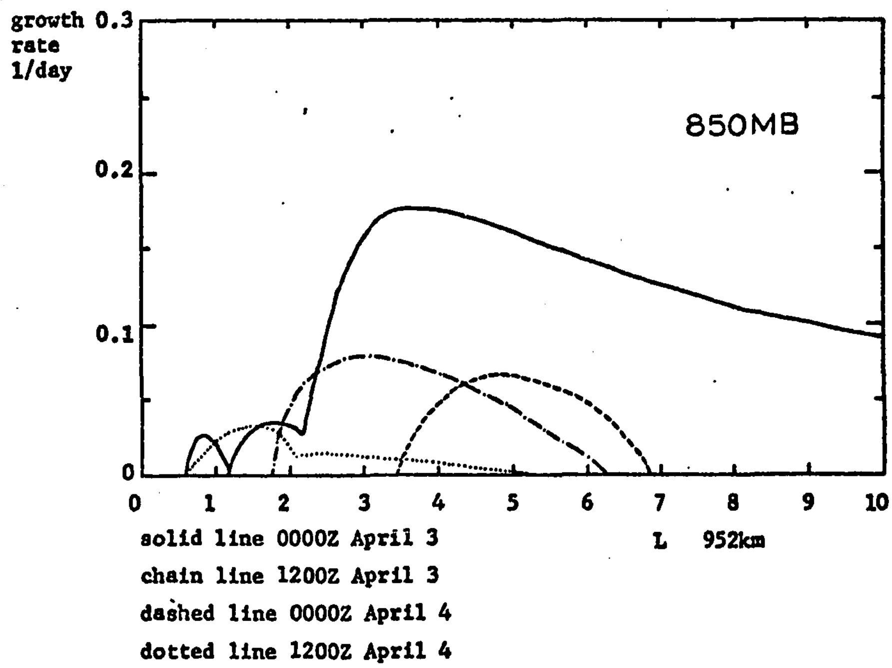

Figure 23. Growth rate versus wavelength for 850 MB profiles.

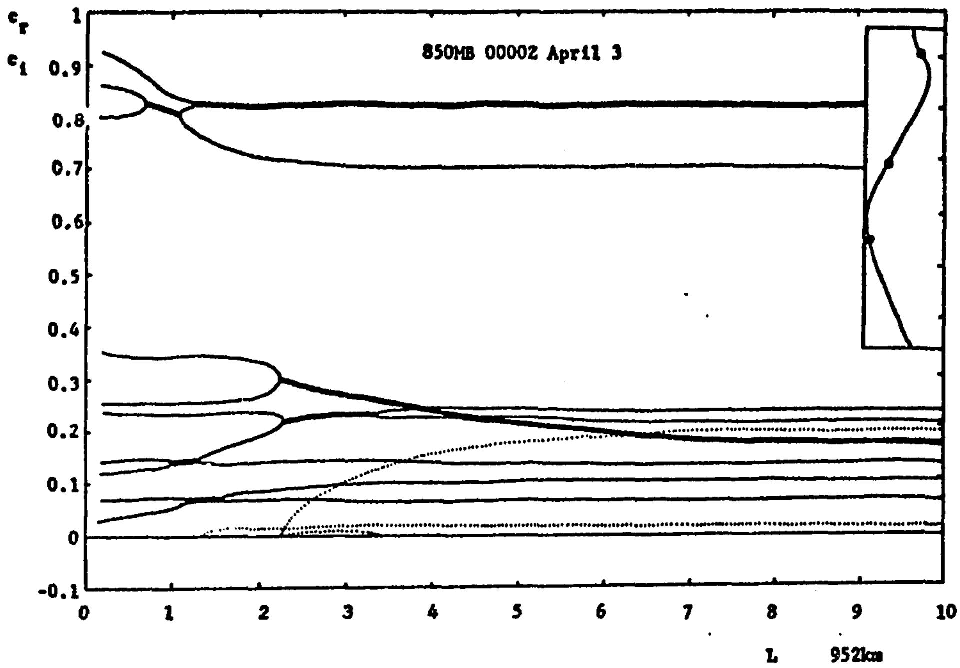

Figure 24a. A (c_r, c_i)-L diagram for 850 MB 0000Z April 3 wind profile.

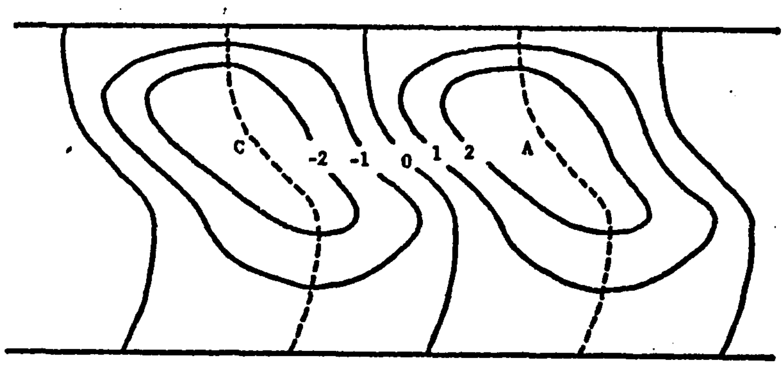

Figure 24b. Disturbance stream function of most unstable wave at L=3.8 (3619 km) for 850 MB 0000Z April 3 wind profile.

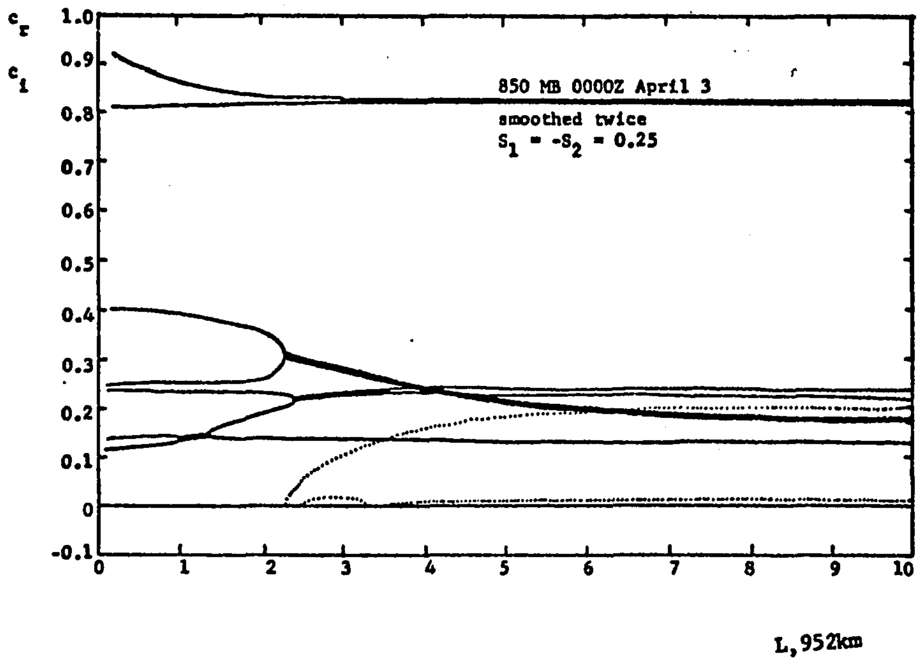

Figure 24c. A (c_r, c_i)-L diagram for 850 MB 0000Z April 3 wind profile smoothed twice with $S_1 = -S_2 = 0.25$.

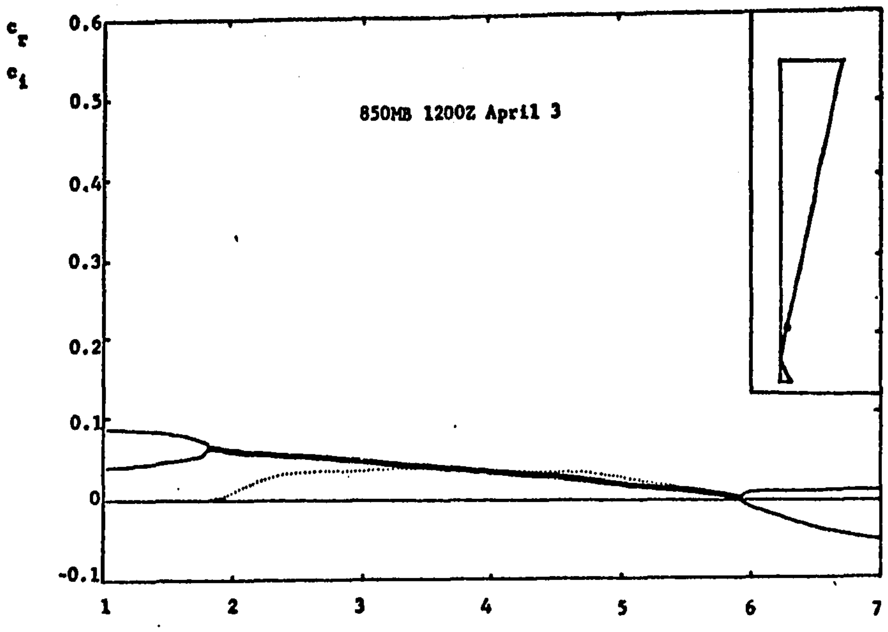

Figure 25a. A (c_r, c_i)-L diagram for 850 MB 1200Z April 3 wind profile.

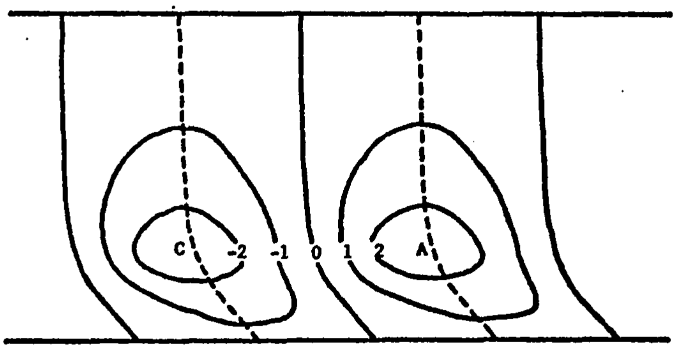

Figure 25b. Disturbance stream function of most unstable wave at L=3.0 (2857 km) for 850 MB 1200Z April 3 wind profile.

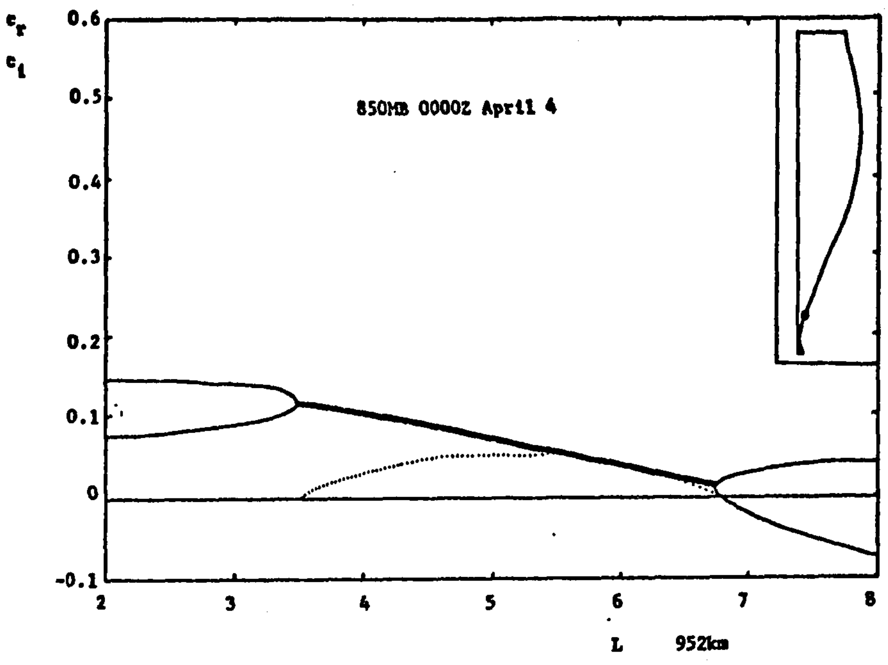

Figure 26a. A (c_r, c_i)-L diagram for 850 MB 0000Z April 4 wind profile.

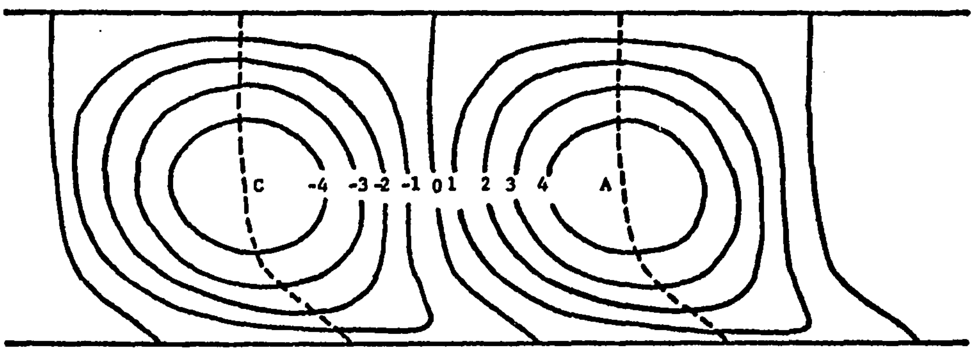

Figure 26b. Disturbance stream function at most unstable wave at L=4.8 (4572 km) for 850 MB 0000Z April 4 wind profile.

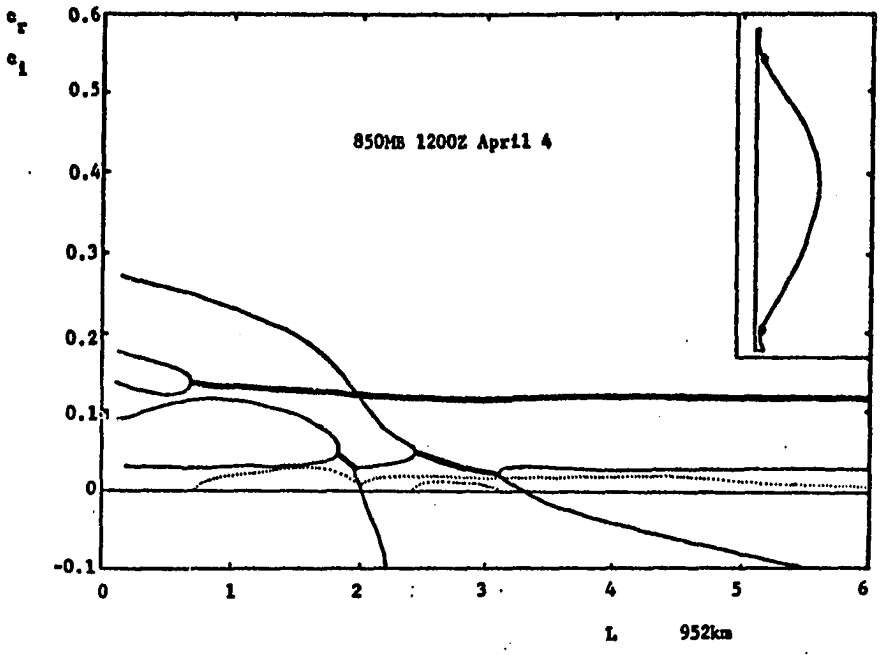

Figure 27a. A (c_r, c_i)-L diagram for 850 MB 1200Z April 4 wind profile.

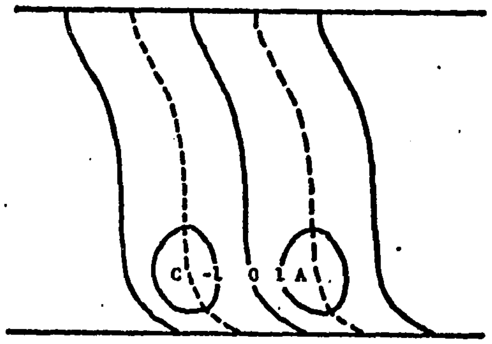

Figure 27b. Disturbance stream function at most unstable wave at L=4.8 (1524 km) for 850 MB 1200Z April 4 wind profile.

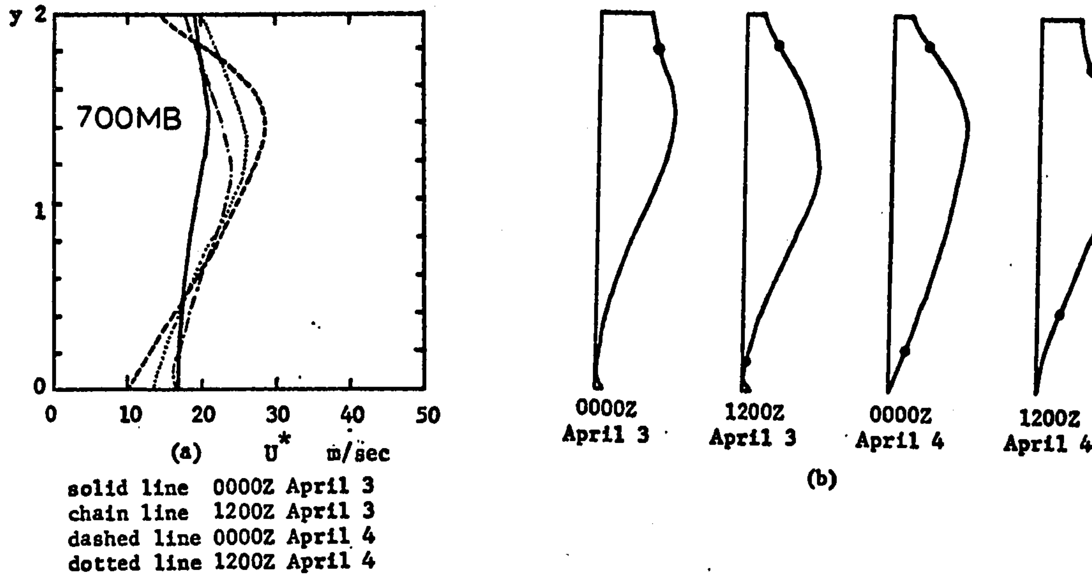

Figure 28. Atmospheric wind profiles at 700 MB. (a) dimensional profiles, (b) dimensionless and normalized profiles.

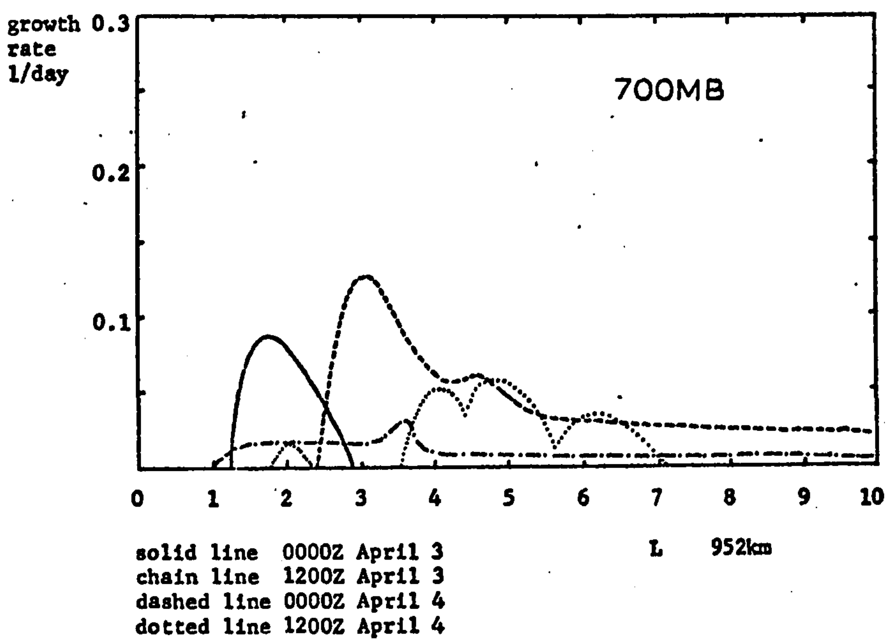

Figure 29. Growth rate versus wavelength for 700 MB profiles.

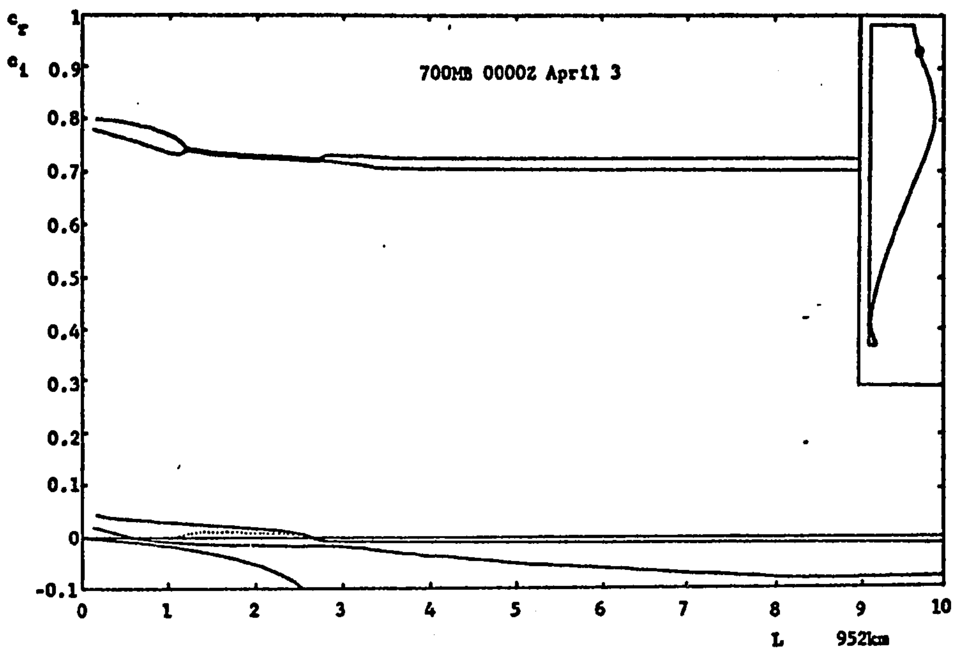

Figure 30a. A (c_r, c_i)-L diagram for 700 MB 0000Z April 3 wind profile.

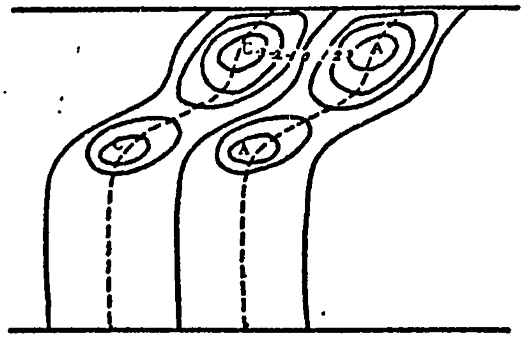

Figure 30b. Disturbance stream function at most unstable wave at L=1.6 (1524 km) for 700 MB 0000Z April 3 profile.

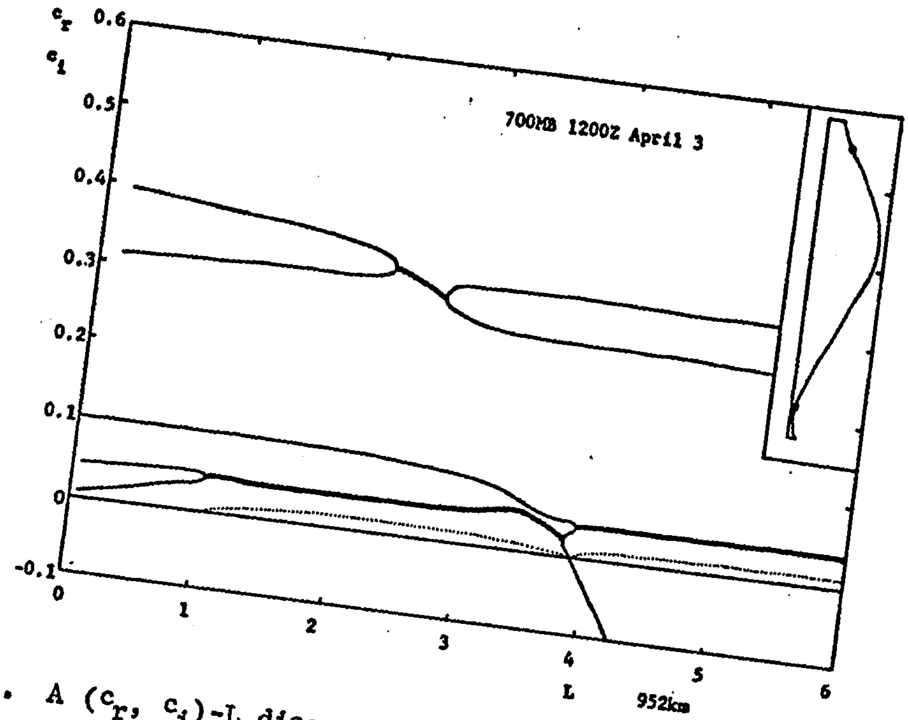

Figure 31a. A (c_r, c_i)-L diagram for 700 MB 1200Z April 3 wind profile.

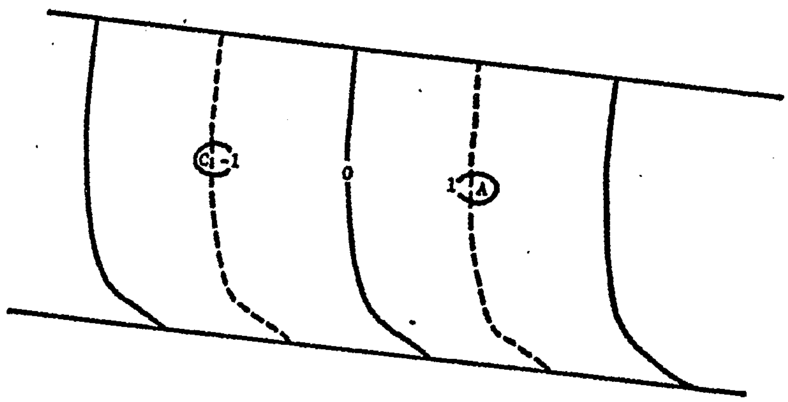

Figure 31b. Disturbance stream function at most unstable wave at L=3.6 (3429 km) for 700 MB 1200Z April 3 profile.

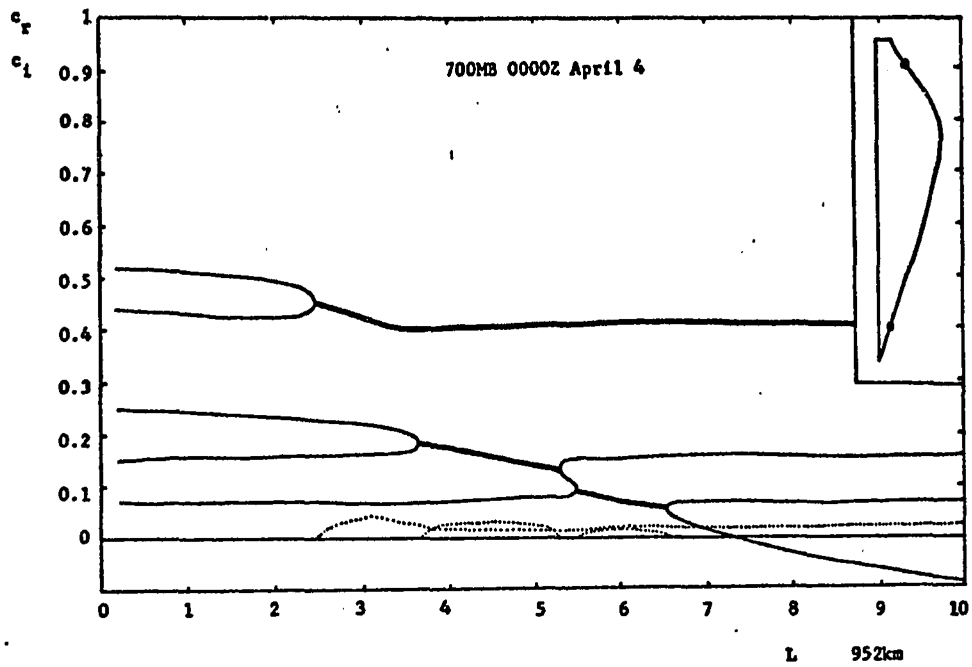

Figure 32a. A (c_r, c_i)-L diagram for 700 MB 0000Z April 4 wind profile.

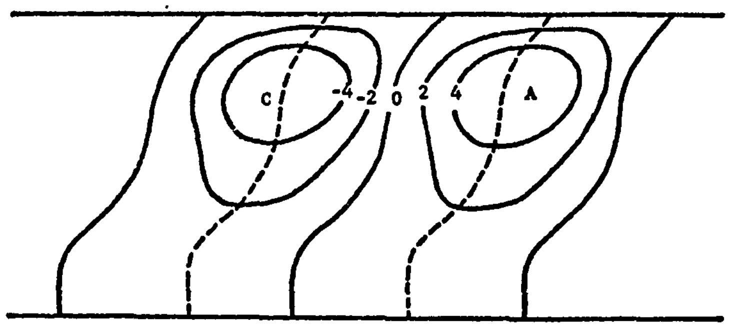

Figure 32b. Disturbance stream function at most unstable wave at L=3.0 (2857 km) for 700 MB 0000Z April 4 profile.

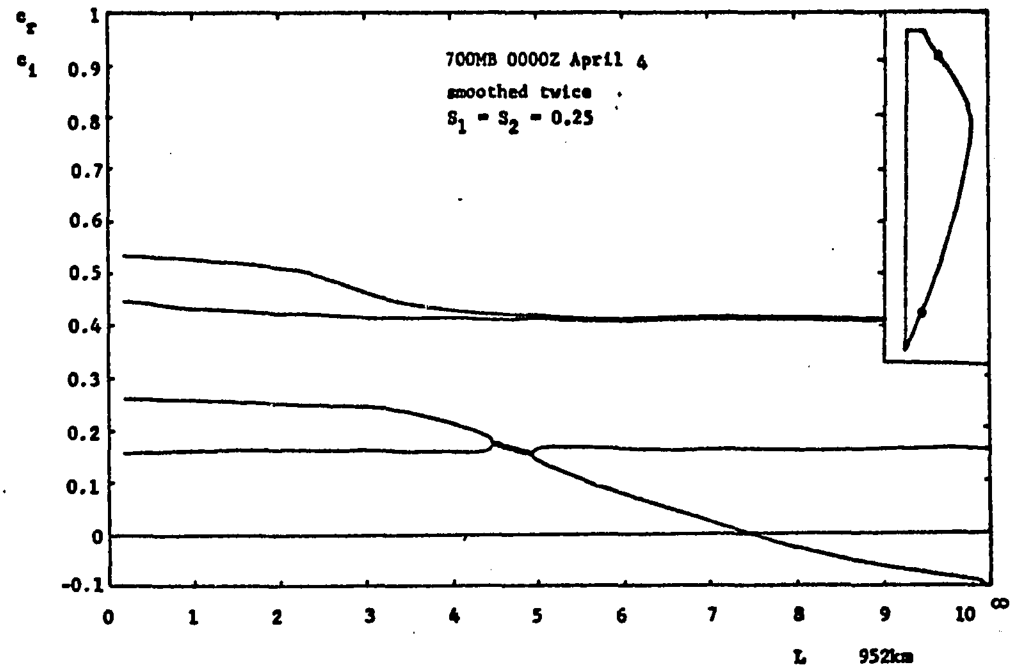

Figure 32c. A (c_r, c_i)-L diagram for 700 MB 0000Z April 4 wind profile smoothed twice with $S_1 = S_2 = 0.25$.

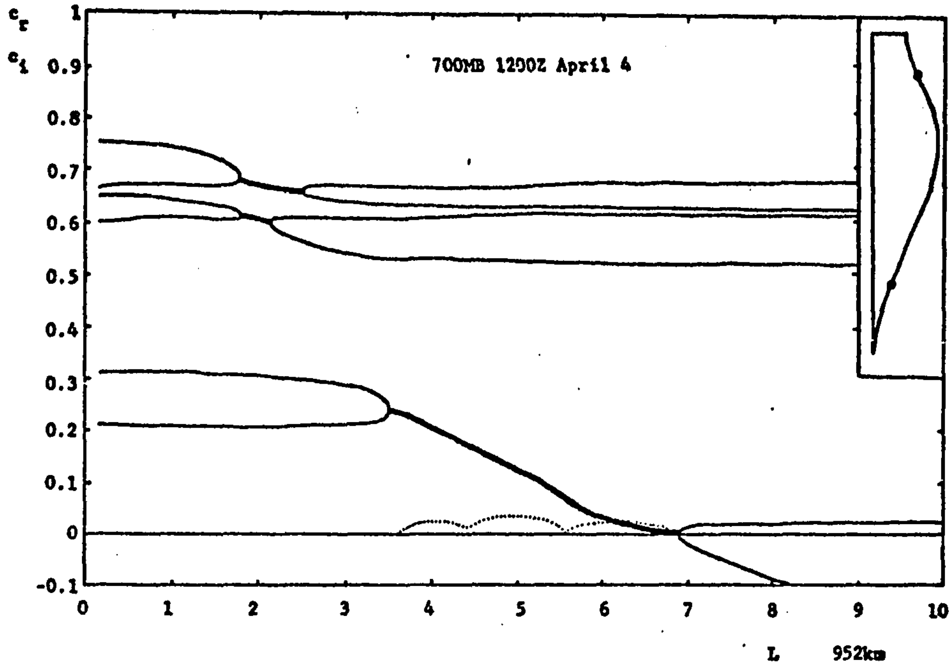

Figure 33a. A (c_r, c_i)-L diagram for 700 MB 1200Z April 4 wind profile.

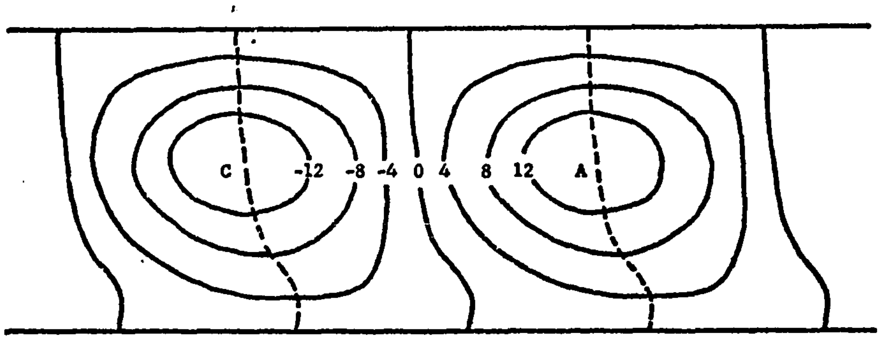

Figure 33b. Disturbance stream function of most unstable wave at L=4.8 (4872 km) for 700 MB 1200Z April 4 profile.

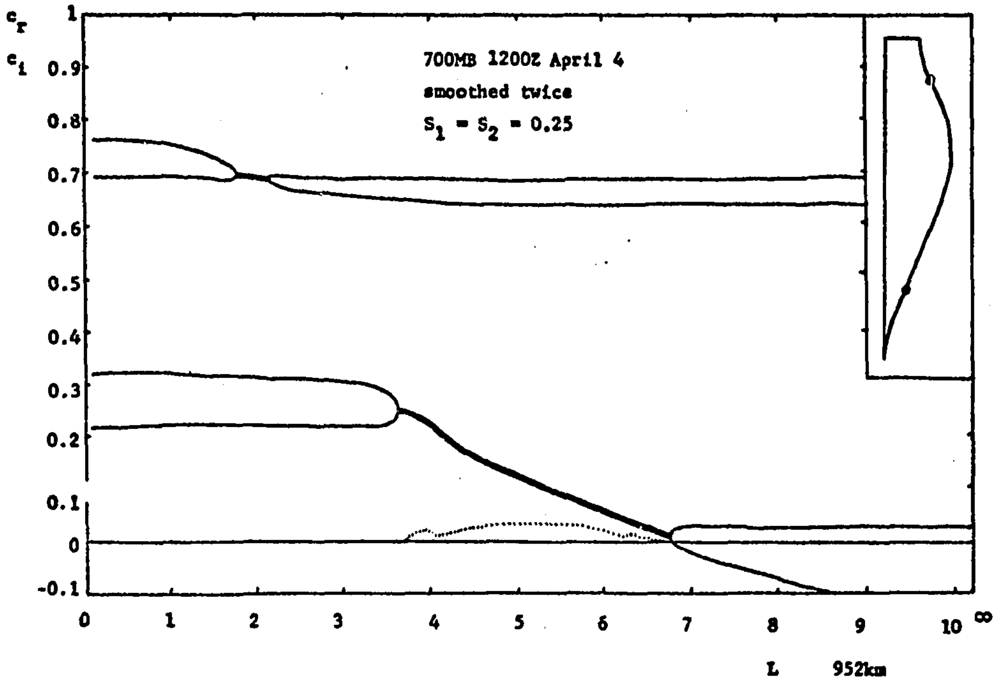

Figure 33c. A (c_r, c_i)-L diagram for 700 MB 1200Z April 4 wind profile smoothed twice with $S_1 = S_2 = 0.25$.

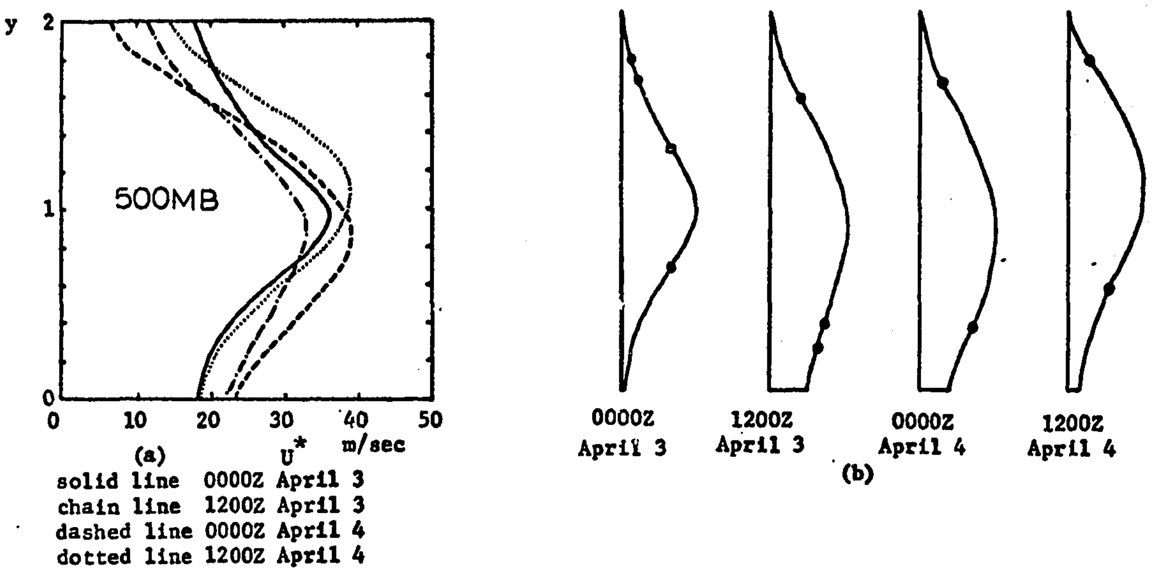

Figure 34. Atmospheric wind profiles at 500 MB. (a) dimensional profiles, (b) dimensionless and normalized profiles.

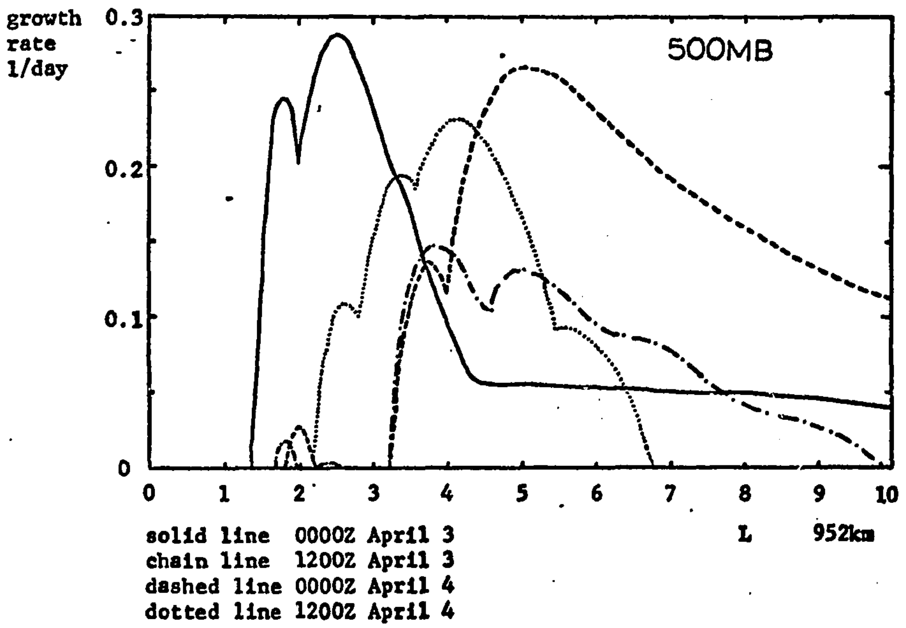

Figure 35. Growth rate versus wavelength for 500 MB profiles.

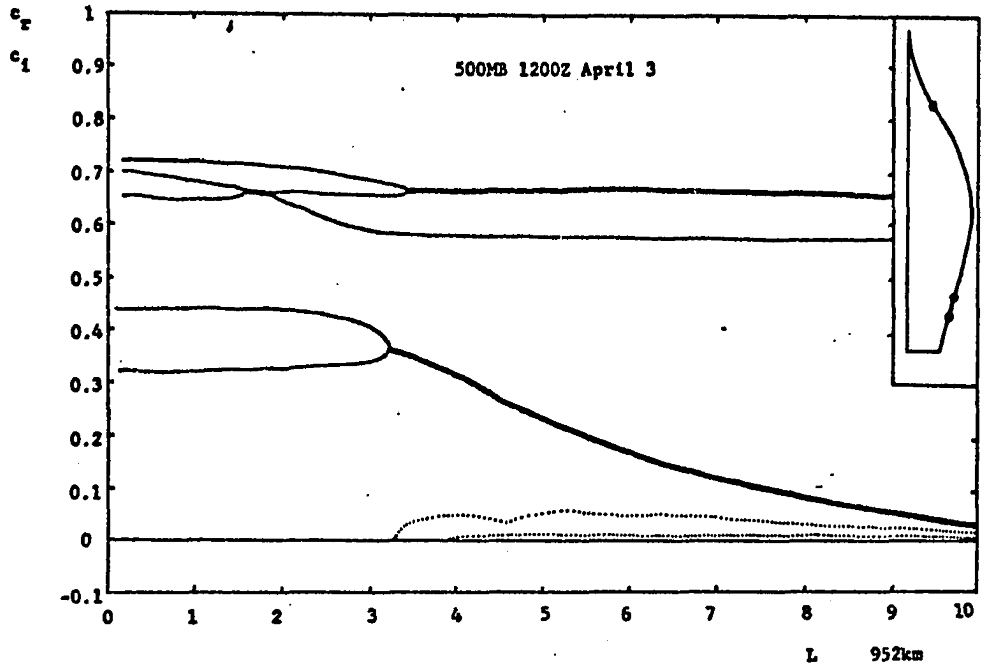

Figure 36a. A (c_r, c_i)-L diagram for 500 MB 1200Z April 3 wind profile.

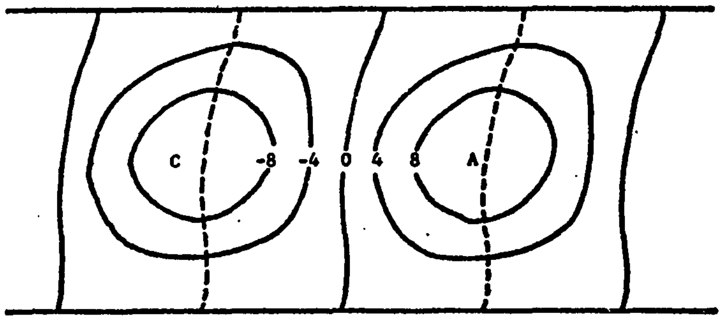

Figure 36b. Disturbance stream function of most unstable wave at L=3.8 (3619 km) for 500 MB 1200Z April 3 wind profile.

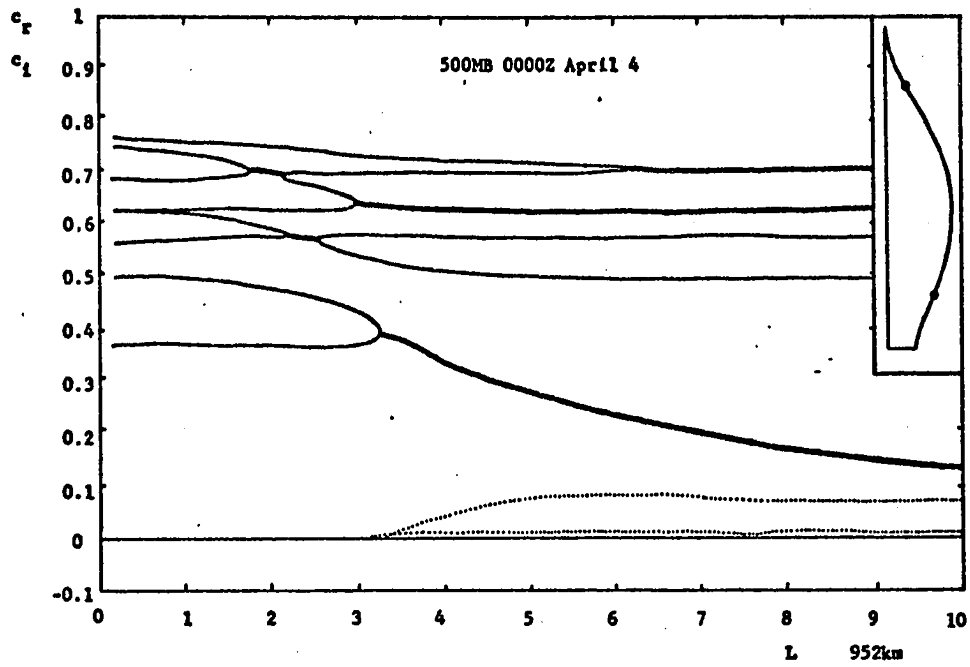

Figure 37a. A (c_r, c_i)-L diagram for 500 MB 0000Z April 4 wind profile.

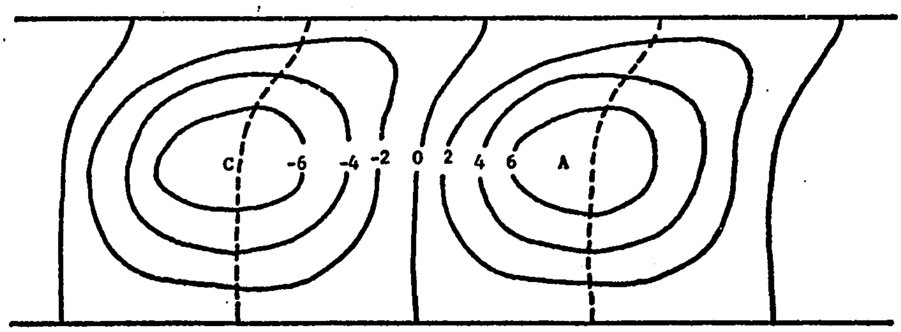

Figure 37b. Disturbance stream function of most unstable wave at L=5.0 (4762 km) for 500 MB 0000Z April 4 wind profile.

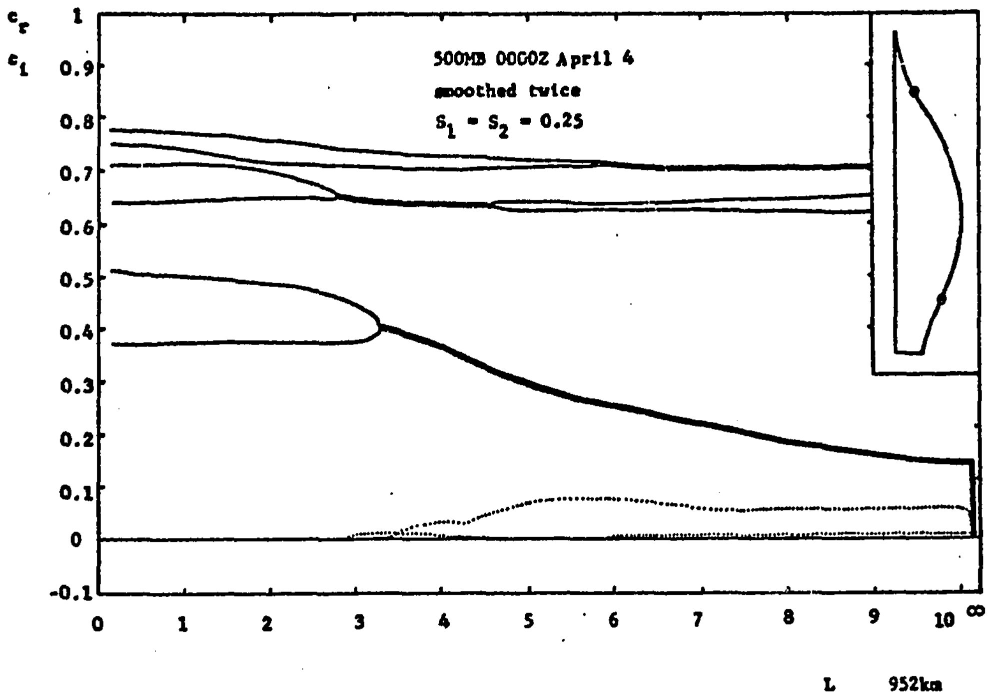

Figure 37c. A (c_r, c_i)-L diagram for 500 MB 0000Z April 4 wind profile smoothed twice with $S_1 = S_2 = 0.25$.

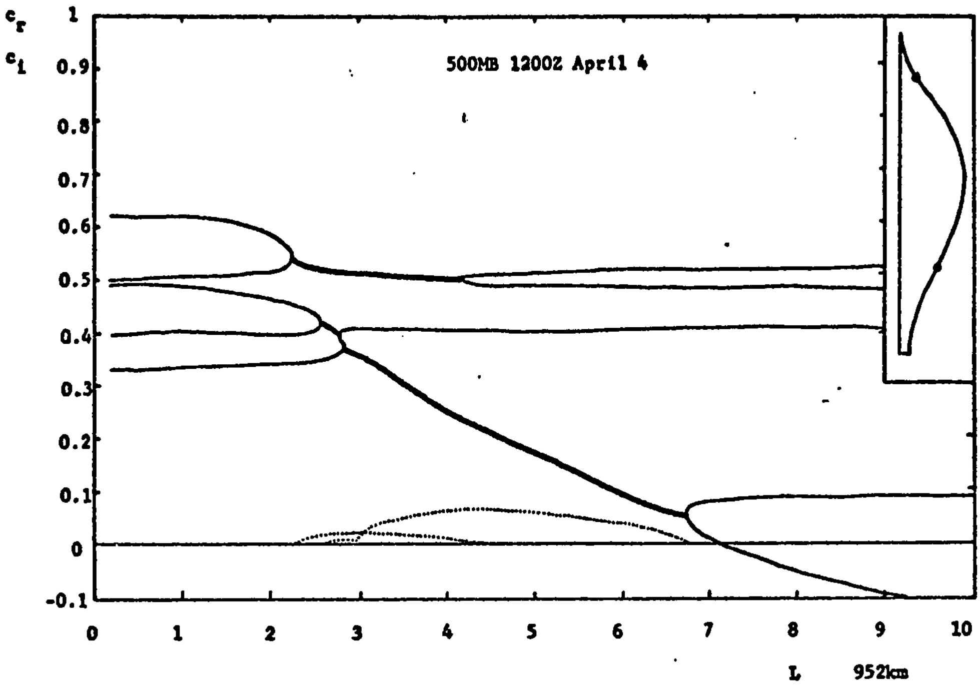

Figure 38a. A (c_r, c_i)-L diagram for 500 MB 1200Z April 4 wind profile.

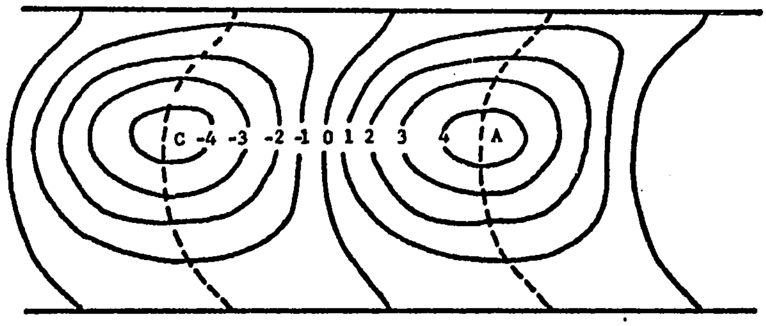

Figure 38b. Disturbance stream function of most unstable wave at L=4.2 (4000 km) for 500 MB 1200Z April 4 profile.

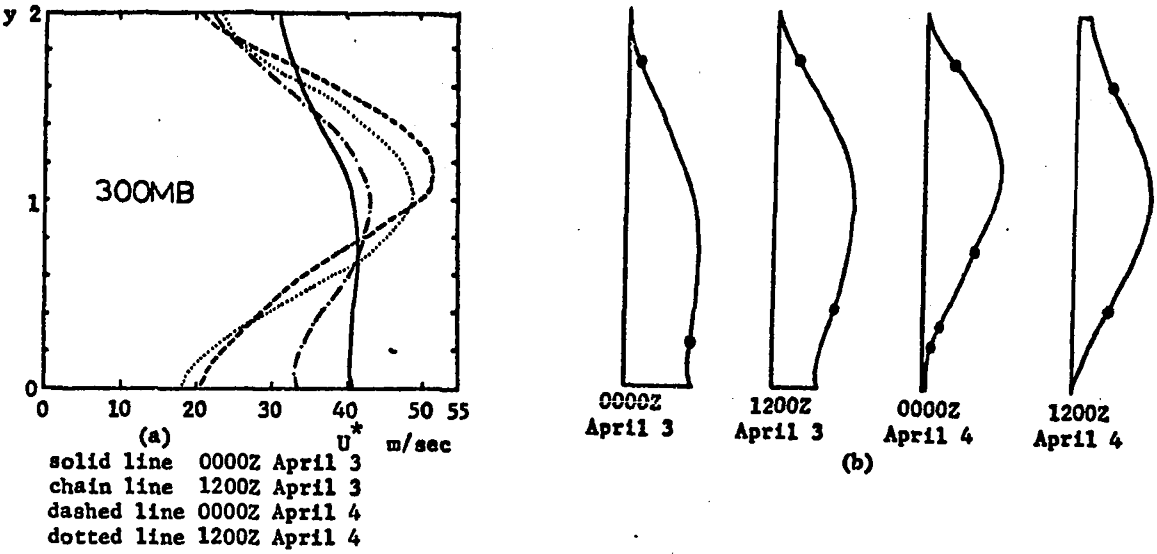

Figure 39. Atmospheric wind profiles at 300 MB. (a) dimensional profiles, (b) dimensionless and normalized profiles.

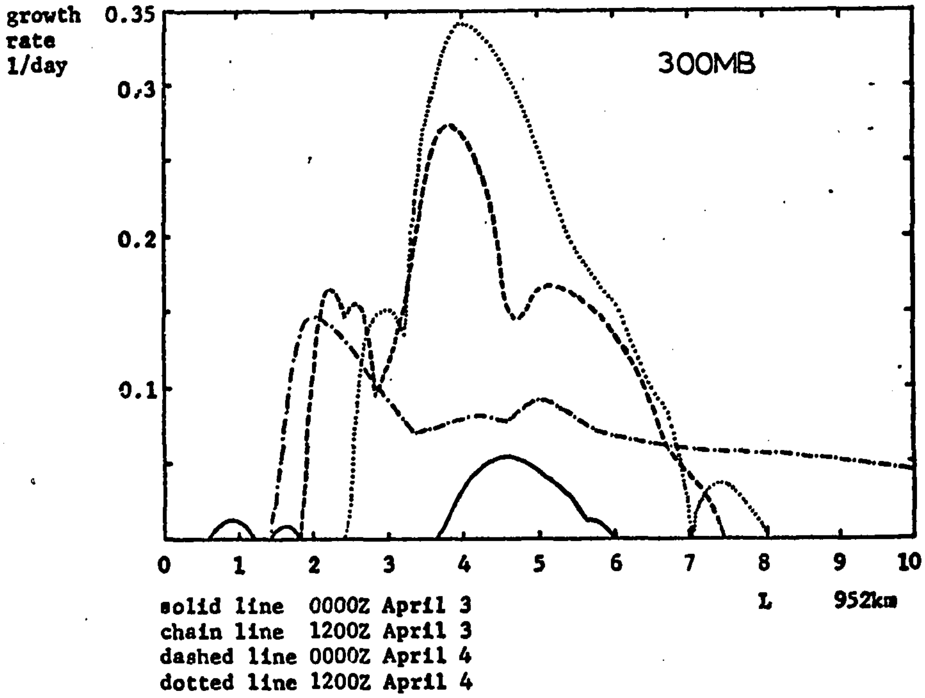

Figure 40. Growth rate versus wavelength for 300 MB profiles.

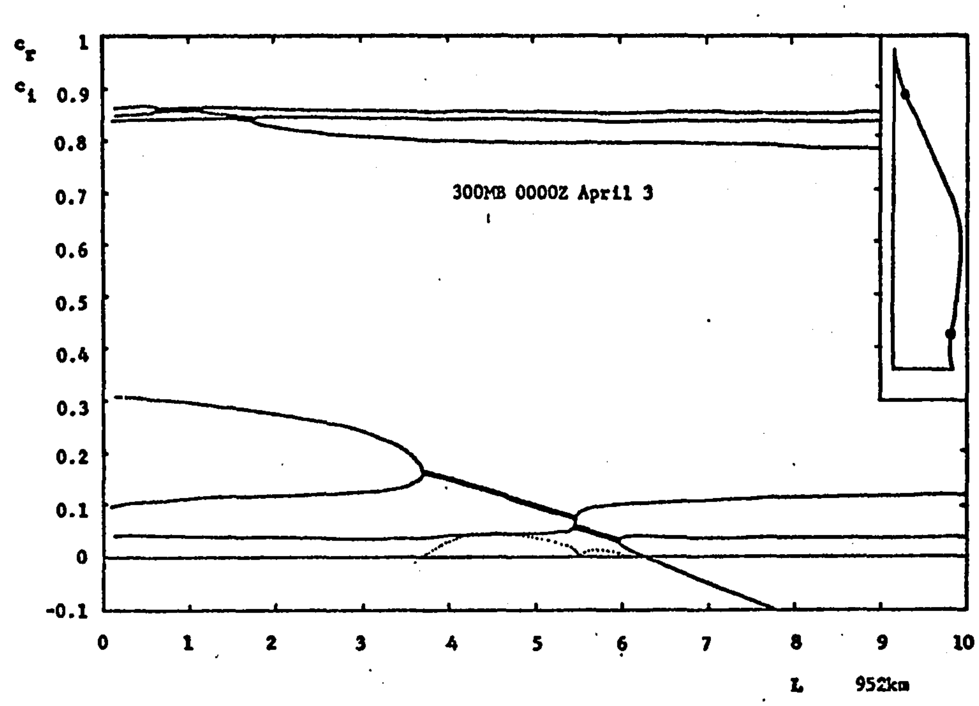

Figure 41a. A (c_r, c_i)-L diagram for 300 MB 0000Z April 3 wind profile.

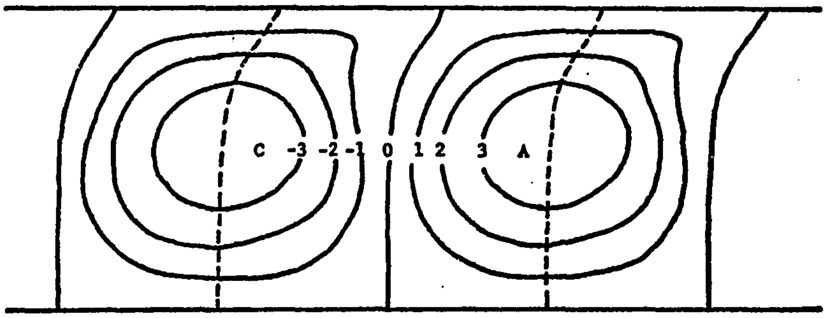

Figure 41b. Disturbance stream function of most unstable wave at L=4.4 (4191 km) for 300 MB 0000Z April 3 profile.

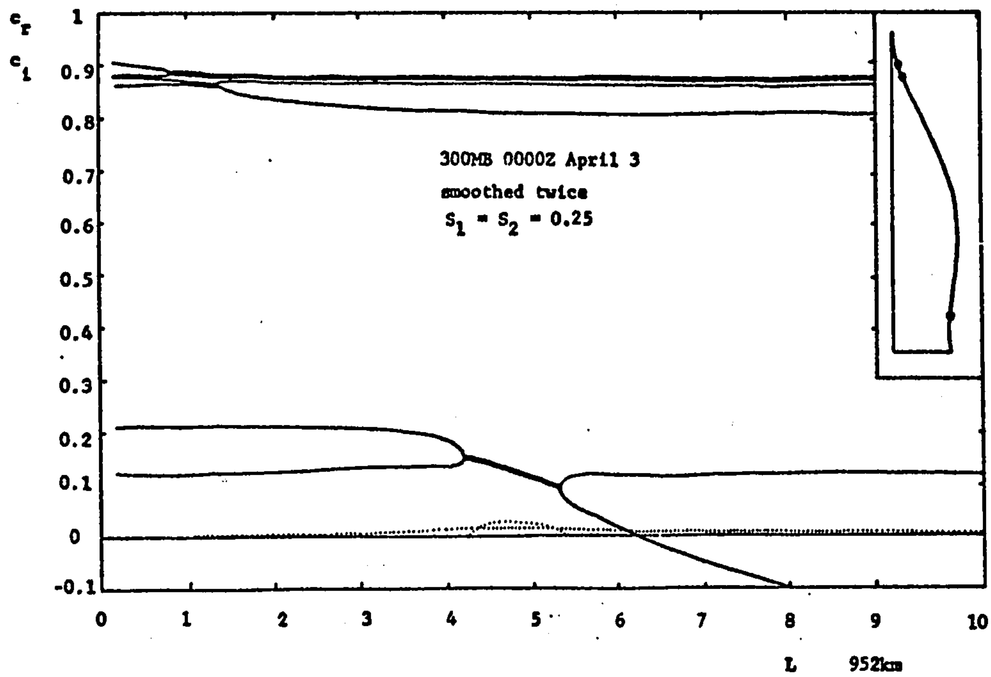

Figure 41c. A (c_r, c_i)-L diagram for 300 MB 0000Z April 3 wind profile smoothed twice with $S_1 = S_2 = 0.25$.

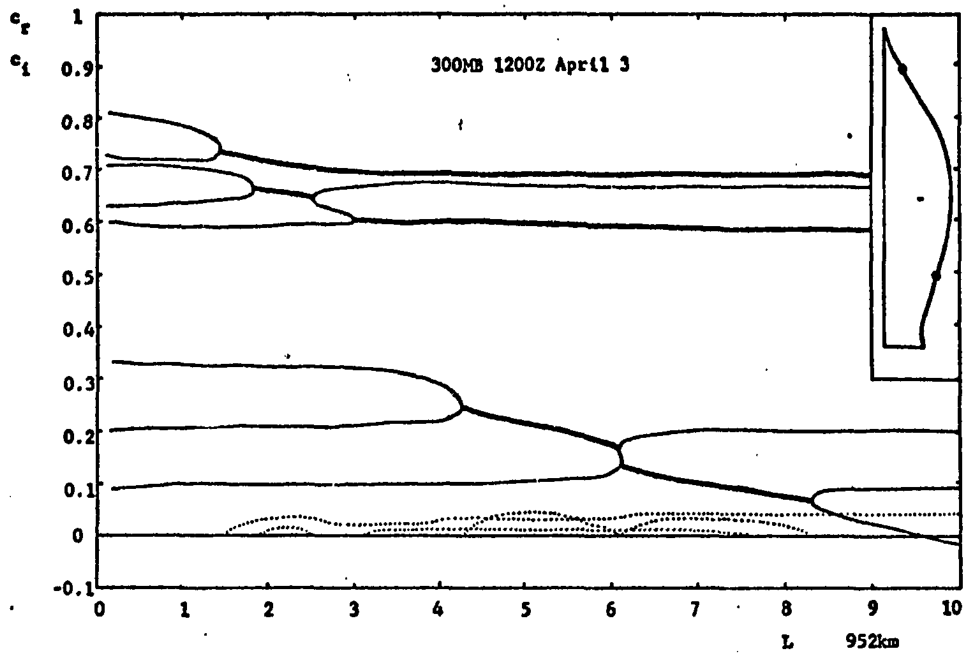

Figure 42a. A (c_r, c_i)-L diagram for 300 MB 1200Z April 3 wind profile.

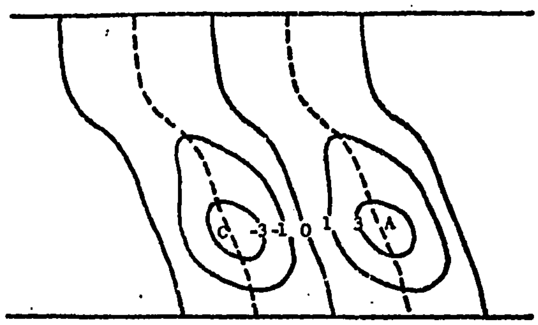

Figure 42b. Disturbance stream function of most unstable wave at L=2. (1905 km) for 300 MB 1200Z April 3 profile.

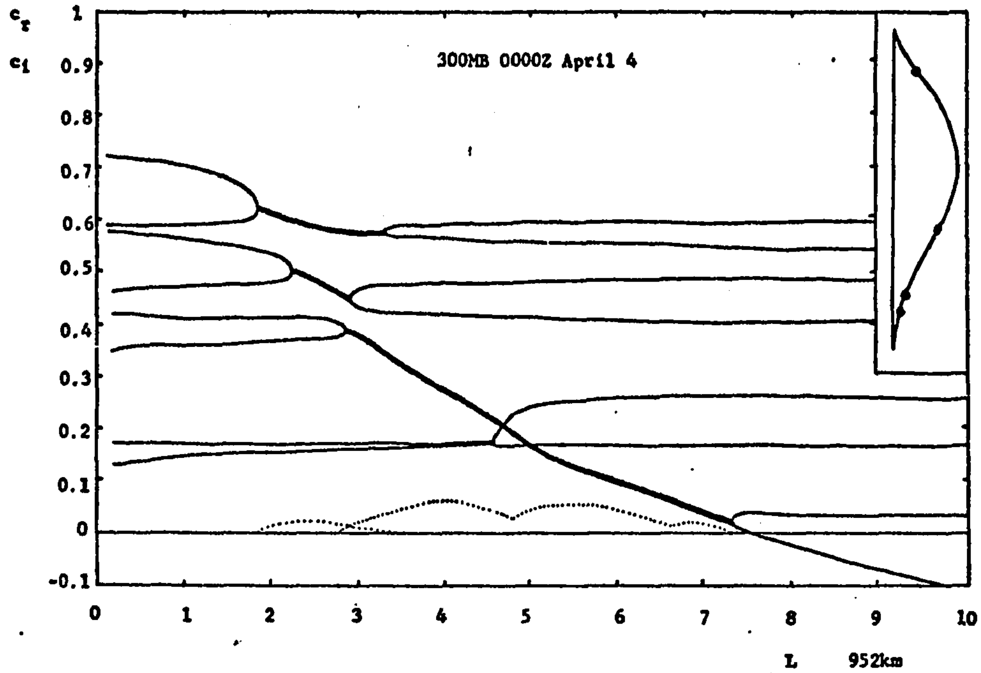

Figure 43a. A (c_r, c_i)-L diagram for 300 MB 0000Z April 4 wind profile.

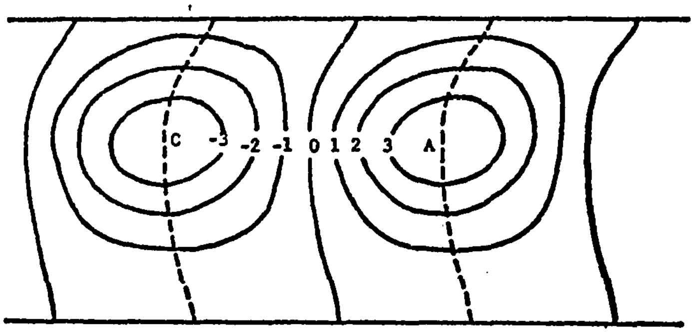

Figure 43b. Disturbance stream function of most unstable wave at L=3.8 (3619 km) for 300 MB 0000Z April 4 profile.

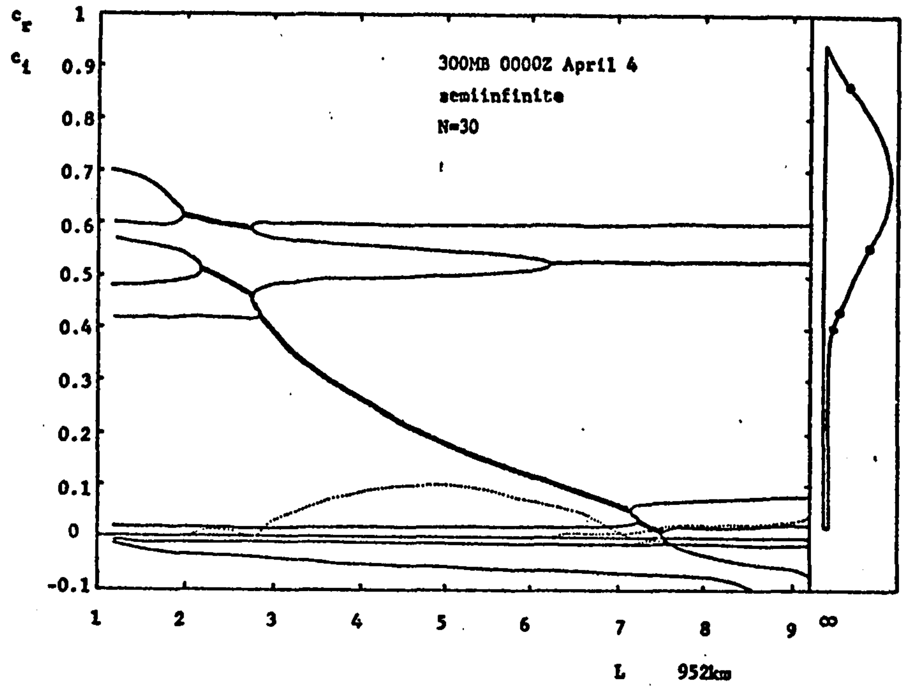

Figure 43c. A (c_r, c_i)-L diagram for 300 MB 0000Z April 4 profile when the lower boundary is extended to infinity.

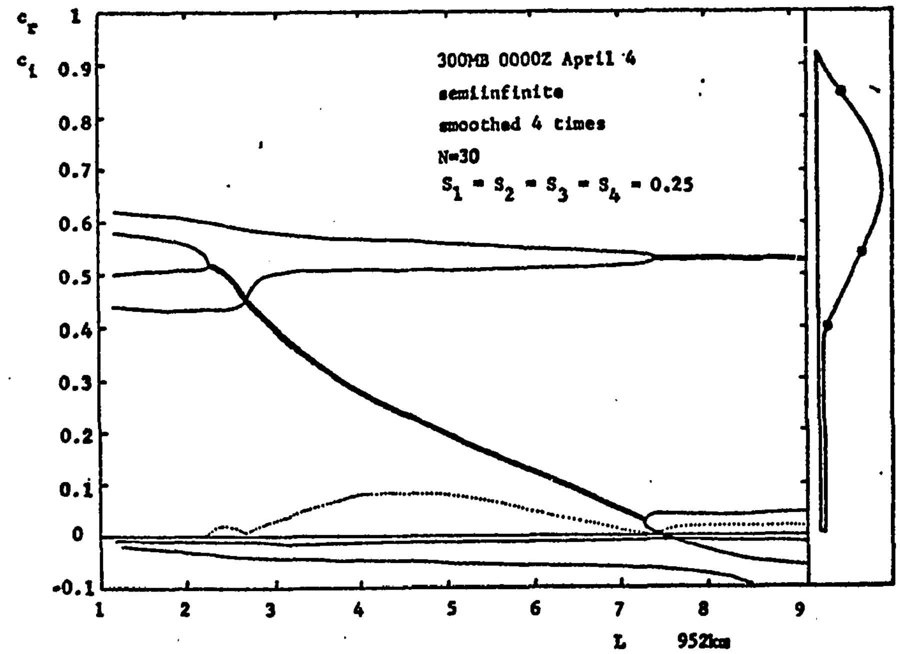

Figure 43d. A (c_r, c_i)-L diagram for 300 MB 0000Z April 4 profile when the lower boundary is extended to infinity and the resulting profile is smoothed four times $S_1 = S_2 = S_3 = S_4 = 0.25$.

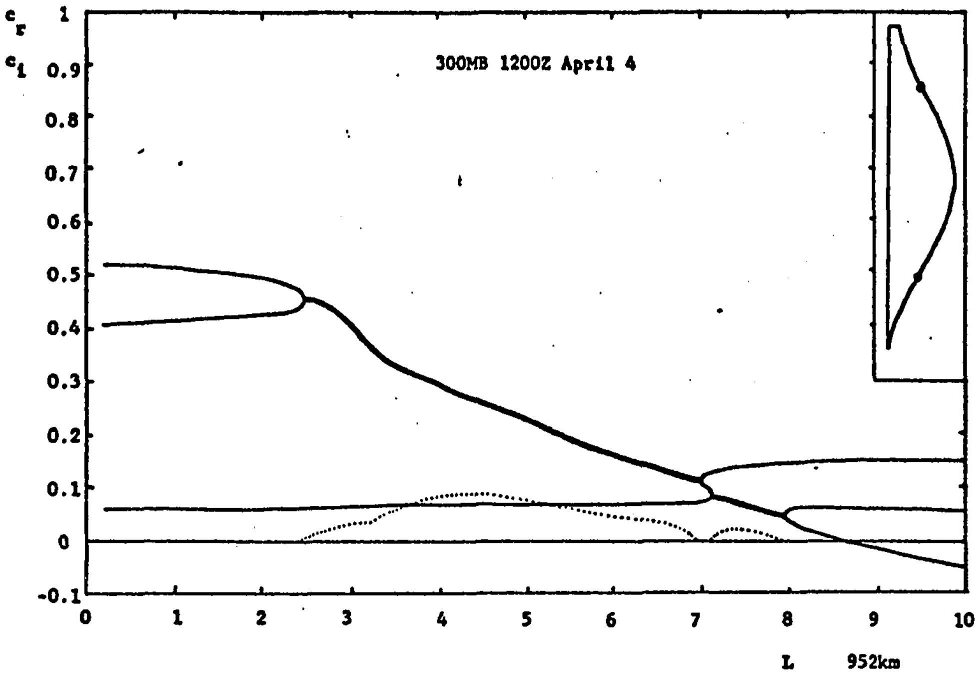

Figure 44a. A (c_r, c_i)-L diagram for 300 MB 1200Z April 4 wind profile.

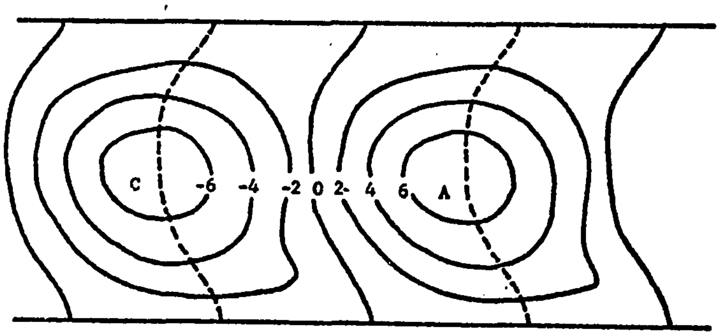

Figure 44b. Disturbance stream function of most unstable wave at L=4.0 (3810 km) for 300 MB 1200Z April 4 profile.

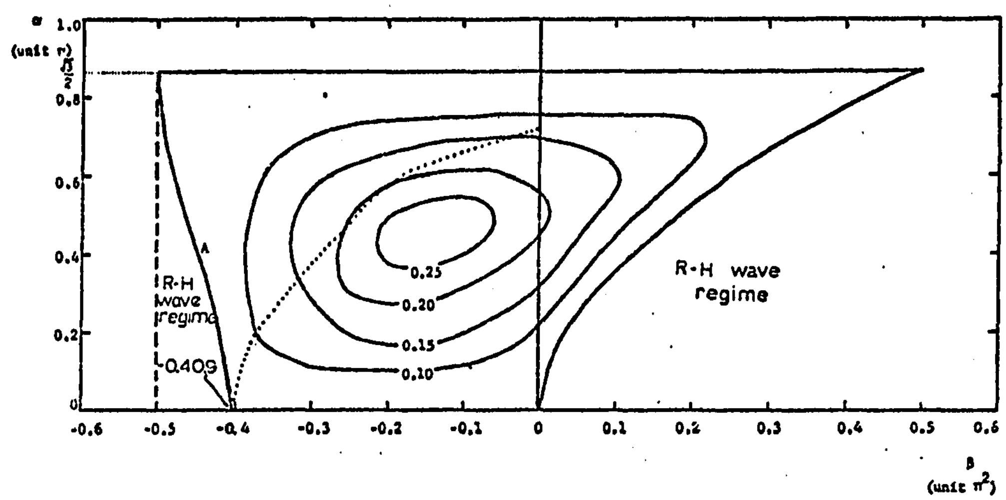

Figure 45. Growth rate versus α and β for the symmetric sine-curve profile $U(y) = \frac{1}{2}(1 - \cos \pi y)$, $0 < y < 2$. The dashed line is the boundary of unstable wave region proposed by Nitta and Yanai (1969) and by Kuo (1973) and line A proposed by Yamasaki and Wada (1972a).

β	α	c_r
-0.5	0.866	1.000
-0.485	0.649	1.012
-0.470	0.537	1.018
-0.455	0.442	1.042
-0.440	0.3471	1.06
-0.430	0.2787	1.07
-0.420	0.1973	1.09
-0.410	0.0619	1.10
-0.409	0.0221	1.103

Table 6. The β, α and c_r values on the upper critical wavelength for the easterly current ($\beta<0$) with the velocity profile $U(y)=\frac{1}{2}(1-\cos \pi y)$, $0 < y < 2$. These values of β and α are plotted in Figure 45, as line A.

β	c_i
-0.409	0
-0.40885	0.00165
-0.40880	0.00682
-0.408	0.0273
-0.407	0.0402
-0.406	0.0498
-0.405	0.0578
-0.404	0.0647
-0.403	0.0710
-0.402	0.0767
-0.401	0.0820
-0.400	0.0869
-0.390	0.124
-0.380	0.152
-0.370	0.174
-0.360	0.192

Table 7. The c_i values on $\alpha=0$ as a function of β for the easterly current ($\beta<0$) with the velocity profile $U(y)=\frac{1}{2}(1-\cos \pi y)$, $0 < y < 2$.

		850 MB	700 MB	500 MB	300 MB
0000Z April 3	(a)	(5.68, 3619)	(85.38, 1524)	(3.44, 2476)	(18.97, 4191)
	(b)	—	stable	(3.70, 2286	—
	(c)	(6.35, 3619)	—	(3.20, 2286)	—
1200Z April 3	(a)	(12.85, 2857)	(32.96, 3429)	(6.91, 3619)	(6.71, 1905)
0000Z April 4	(a)	(15.20, 4572)	(7.98, 2857)	(3.77, 4762)	(3.60, 3619)
	(b)	—	(117, 4572)	—	—
	(c)	—	—	(3.76, 4572)	(2.74, 4000)
1200Z April 4	(a)	(33.50, 1524)	(18.11, 4572)	(4.27, 4000)	(2.93, 3810)
	(b)	stable	—	—	—
	(c)	(29.49, 1524)	—	—	—

(a) for a bounded nonsmoothed profile

(b) for a bounded profile smoothed once $S_1 = 0.25$

(c) for a semiinfinite profile

(d) for a semiinfinite profile smoothed once $S_1 = 0.25$

Table 8. The e-folding time of the most unstable wave, and the most preferred wavelength, for each wind profile considered in this study. The first value in the parenthesis is the e-folding time in days, the second value is the most preferred wavelength in km.

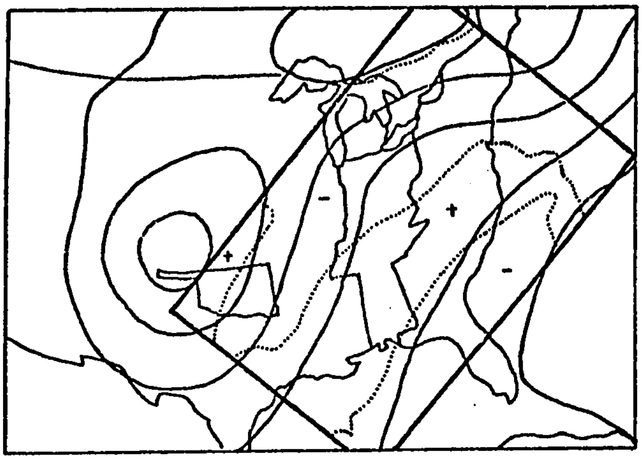

850 MB 0000Z April 3

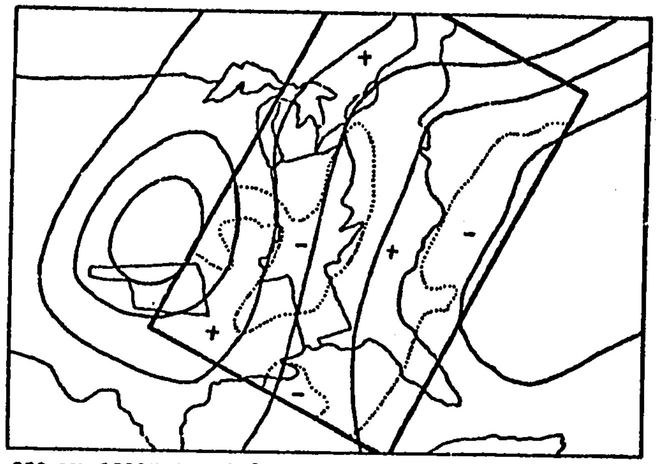

850 MB 1200Z April 3

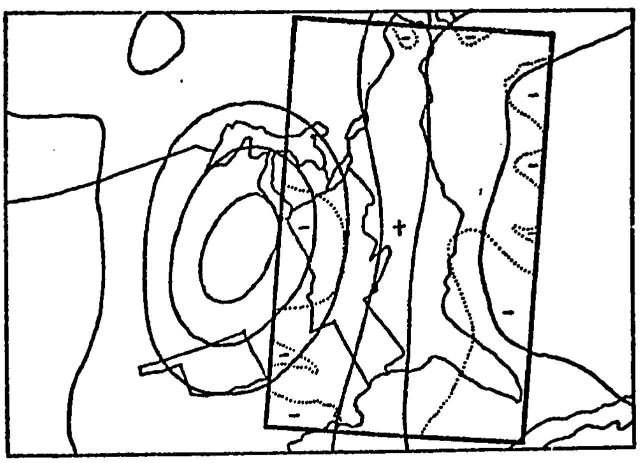

850 MB 0000Z April 4

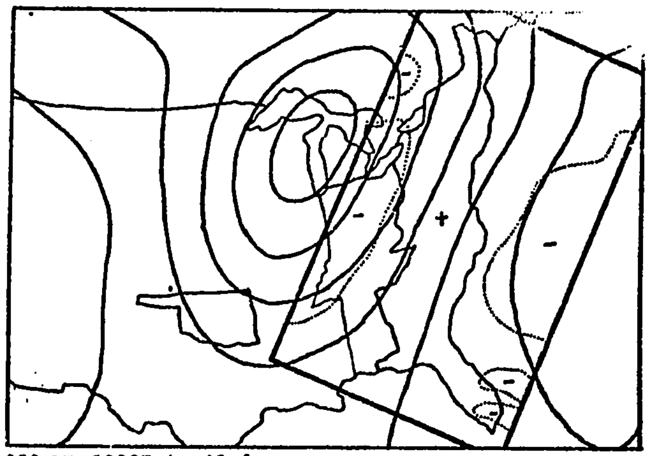

850 MB 1200Z April 4

Figure 46. Weather maps at 850 MB for four time steps and the domains considered in this study.

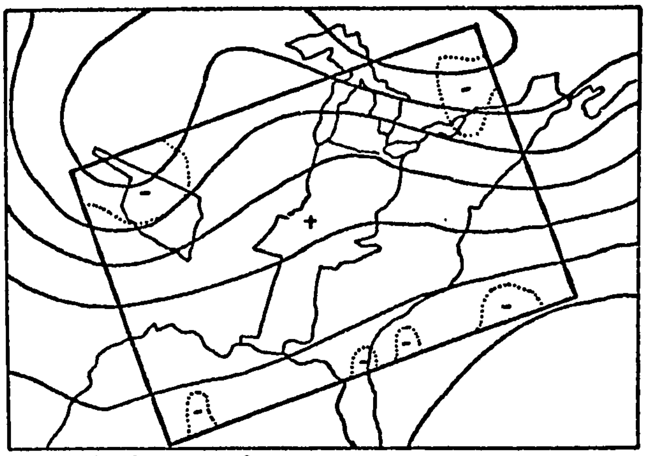

700 MB 0000Z April 3

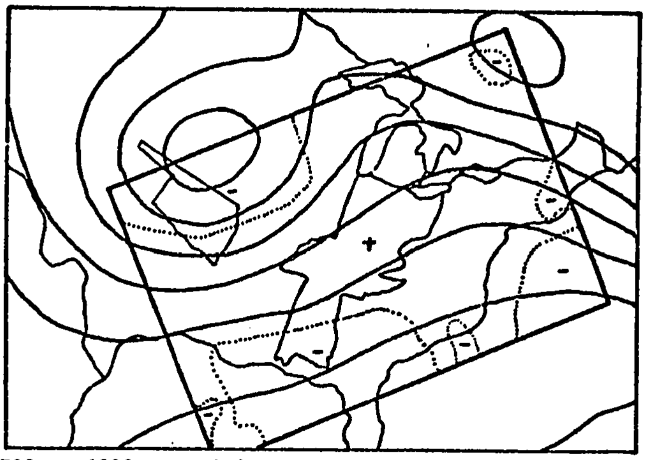

700 MB 1200Z April 3

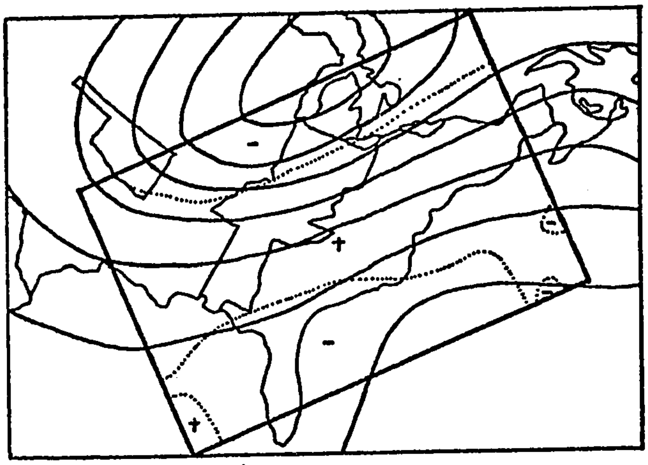

700 MB 0000Z April 4

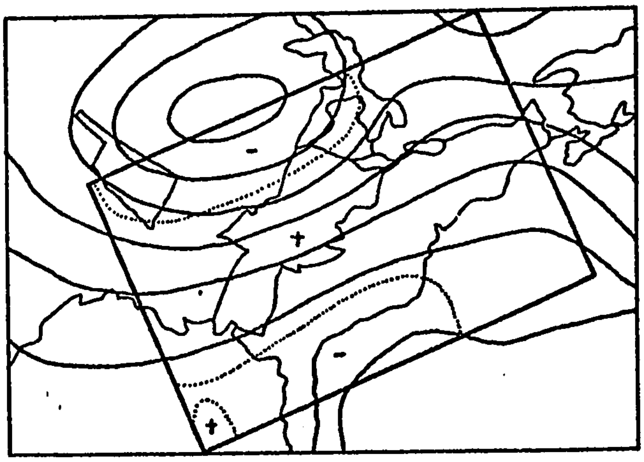

700 MB 1200Z April 4

Figure 47. Weather map at 700 MB for four time steps and the domains considered in this study.

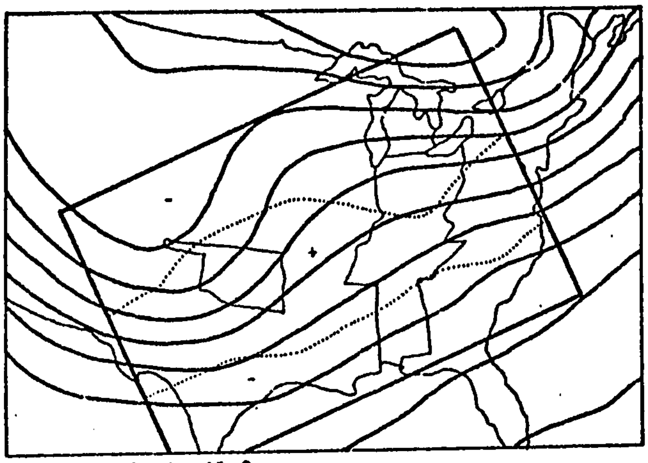

500 MB 0000Z April 3

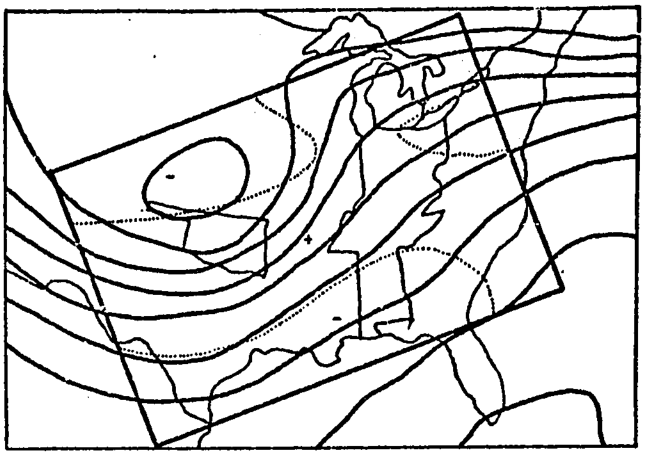

500 MB 1200Z April 3

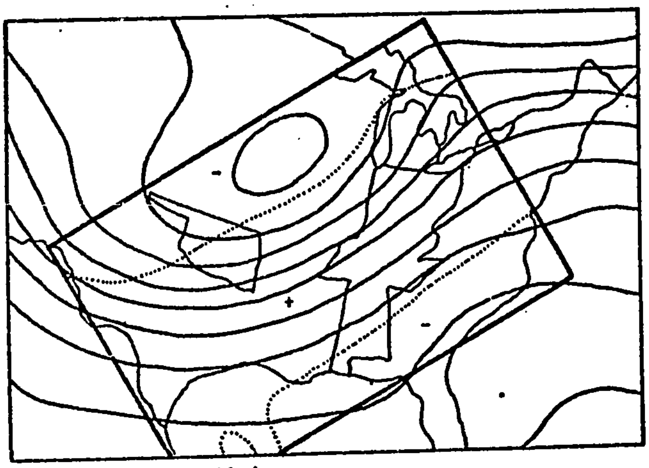

500 MB 0000Z April 4

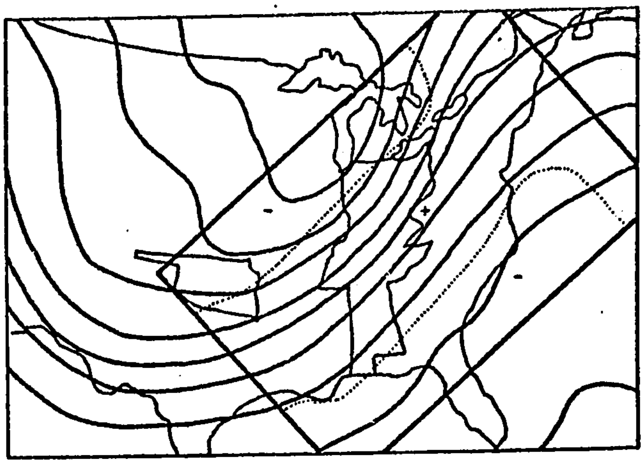

500 MB 1200Z April 4

Figure 48. Weather map at 500 MB for four time steps and the domains considered in this study.

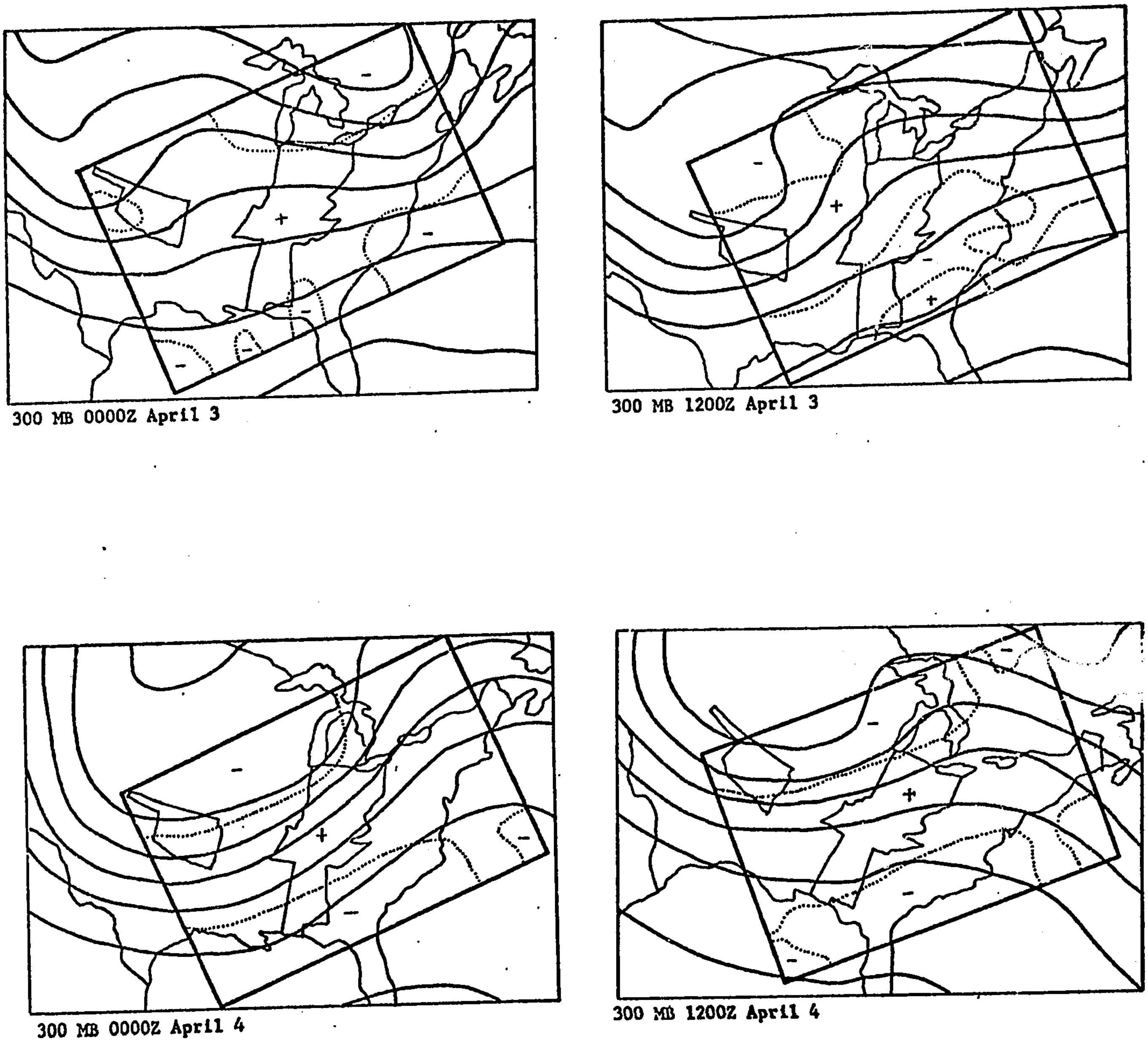

Figure 49. Weather map at 300 MB for four time steps and the domains considered in this study.